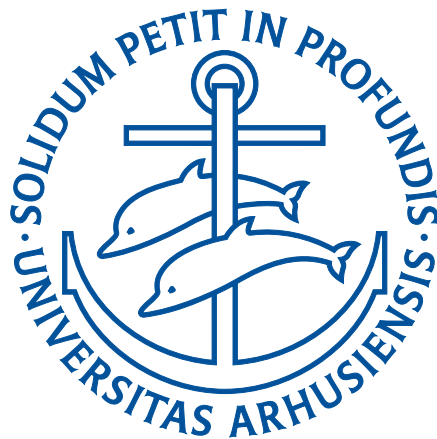


TOWARDS COLLECTIVE
OPTOMECHANICS WITH
NANOMEMBRANES



PHD THESIS

BHAGYA NAIR

JANUARY 11 2017

DEPARTMENT OF PHYSICS AND ASTRONOMY
AARHUS UNIVERSITY

This thesis is submitted to the Graduate school of science and technology (GSST), Aarhus University, Denmark, as per the requirements for successful completion of PhD degree. The thesis studies have been carried out under the supervision of Associate Prof. Aurelien Dantan in the Optomechanics group at Department of Physics and Astronomy, Aarhus University from September 2013 to November 2016.

Preface

The present thesis summarizes our work towards establishing a “Optomechanics ” (OM) lab at the university. And this thesis describes the first steps towards the experimental realization of collective optomechanics. In the last 3 years, we have been working in two different directions till now, an experimental direction where our primary aim is to build the optomechanics lab from scratch and as well as to investigate theoretical aspect of cavity optomechanics in as yet unexplored scenarios such as cavity optomechanics with thick nanomembranes and hybrid optomechanics with doped systems.

For the guidance, support and supervision, i’m grateful to my supervisor Aurelien Dantan who has not only provided me with the opportunity to work in the project but also helped me in the better understanding of optics and optomechanics at each step. I’m also extremely indebted to Aurelien for the proof-reading and corrections of the present thesis.

Over the course of 3 years, in setting up our OM lab, we have had help and advice from various sources. For the custom fabrication of our double membranes and notched membranes, Norcada Inc., Edmonton, Canada has helped us with useful discussions and valuable inputs.

For the assembly of experimental setup and vacuum testing, all members of mechanical workshop and vacuum lab at the Physics department have been immensely helpful. Anders Damgaard, Henrik Bechtold, John Andersen, Torben Thomsen, René Warthoe, Simon Lajer and Anders Petersen have all helped in the design, manufacture of parts and construction of our experimental chambers and gluing tool.

And our colleagues from the chemistry and inano department have guided us in various efforts, from aiding in the development of membrane gluing process to providing training in the cleanroom for nano-fabrication and characterization processes. Special thanks to Bjarke Jeppesen and Pia Jensen for providing training in the cleanroom and always being helpful with valuable suggestions and in debugging any machine problems. It’s been a pleasure to work with Bjarke who not only trained me in most of the cleanroom machines but was always available for discussions and problem solving. Jacques Chevallier, Folmer Lyckegaard, Ramon Liebrechts, John Hansen and Jesper Vinther have helped us with useful suggestions and in tackling cleanroom machine failures.

The Ion trap group has been generous to allow us to access their workshop and tools which has served to be immensely helpful. Also, it’s been a pleasure to work along side Ion trappers who have helped us with useful inputs from time to time. Julian Glässel has

helped us to set-up a Labview interface system and Hans Andersen has helped me with the Latex template.

Also, i'm thankful to my family and friends for their care, support and understanding.

Finally, my welcome and thanks to our new lab members Anders Næsby and Sepideh Naserbakht who have taken over the project and am sure are going to succeed in the future experiments.

Bhagya Nair, January 2017

Abstract (English)

High quality nanomechanical resonators exploiting the effects of electromagnetic radiation pressure have a broad range of applications ranging from metrology and sensing to information processing. The work presented in this thesis takes place in the context of optomechanics with integrated arrays of mechanical resonators consisting of high tensile stress silicon nitride membranes.

In the first part of the thesis we report on the first steps in assembling and characterizing periodic arrays of such membranes. We also report on the design and construction of a cavity optomechanics setup and discuss the prospects for future experiments with these arrays.

In the second part we present the design, fabrication and first characterization of subwavelength grating structures on commercial, high tensile stress membranes in order to improve their reflectivity. The last part of the thesis deals with a theoretical investigation of hybrid cavity optomechanics with doped membranes.

Abstract (Danish)

Der er mange praktiske anvendelser for højkvalitets nanomekaniske resonatorer, der udnytter effekterne af elektromagnetisk strålingspres. Disse findes inden for en bred vifte der spænder fra metrologi, præcisionsmålinger og over til informationsprocessering. Arbejdet, der præsenteres i denne PhD afhandling, omhandler optomekanik med integrerede rækker af mekaniske resonatorer lavet af silicium nitrid membraner der har høj intern trækstyrke. I den første del af denne tese beskrives de første skridt med at samle og karakterisere periodiske rækker af disse membraner. Der rapporteres også på design og konstruktion af en kavitet optomekanisk forsøgsopstilling og der diskuteres fremtidige mulige eksperimenter med disse mekaniske rækker. I den anden del præsenteres designet, fabrikationen og den første undersøgelse af en optisk ristestruktur med strukturer mindre end en bølgelængde. Disse er lavet på kommercielt tilgængelige membraner med høj intern trækstyrke for at forbedre deres reflektivitet. Til sidst omtales den teoretiske undersøgelse af hybrid kavitets optomekanik med membraner der er blevet tilsat optisk tilgængelige urenstilstande.

List of publications

- Bhagya Nair, Andreas Næsby, Aurélien Dantan, “Optomechanical characterization of silicon nitride membrane arrays”, Manuscript in preparation
- Bhagya Nair, André Xuereb, Aurélien Dantan, “Cavity optomechanics with arrays of thick dielectric membranes”, *Phys. Rev. A*, 94(2016), page 053812.
- Aurélien Dantan, Bhagya Nair, Guido Pupillo, Claudiu Genes, “Hybrid cavity mechanics with doped systems”, *Phys. Rev. A*, 90(2014), page 033820

Contents

Preface	i
Abstract (English)	iii
Abstract (Danish)	iv
List of publications	v
Contents	vi
1 Introduction	1
2 Cavity optomechanics with movable reflectors	5
2.1 Planar Fabry Perot cavity	5
2.2 Fabry Perot cavity with movable end mirror	15
2.3 Fabry Perot cavity with Membrane-in-the-middle approach	21
2.4 Fabry Perot with periodic arrays of reflectors	23
3 Silicon nitride membrane arrays	28
3.1 Single Si_3N_4 membrane	28
3.2 Single Si_3N_4 membrane characterization	31
3.3 Fabrication of Si_3N_4 membrane arrays	48
3.4 Optical characterization of double membrane arrays	53
3.5 Transmission of wedged Fabry Perot cavity	62
4 Towards cavity optomechanics with membrane arrays	68
4.1 Experimental setup	68
4.2 Optomechanics in the thick membrane regime	74
5 High reflectivity Si_3N_4 membranes	84
5.1 RCWA theory for rectangular grating	84
5.2 Grating simulation studies	88
5.3 Fabrication and characterization of SWG	99
5.4 Characterization of Si_3N_4 membranes	109
5.5 Optical characterization of grating on Si_3N_4 membrane	112

6 Hybrid cavity mechanics with doped systems	117
6.1 Model	119
6.2 Results	125
6.3 Conclusion	130
7 Conclusion	133
Bibliography	135

Chapter 1

Introduction

Cavity optomechanics is a growing field within physics which studies the interaction of electromagnetic and mechanical fields. When light impinges on an object it exerts a radiation pressure force through momentum transfer and, if the object is a mechanical resonator, can affect its vibrational properties. The first experimental effects of radiation pressure force predicted by Maxwell were observed by Nichols and Hull, and Lebedev in 1901 [1].

The interest in optomechanical systems increased with the pioneering work of Braginsky, Caves et al [2] [3] and the development of gravitational wave interferometers (such as LIGO or VIRGO) in the 1970's and 80's. Their investigation into achieving ultra-precise displacement detection systems led to the analysis of the effect of radiation pressure backaction on mirrors and hence set the foundation of the modern field of cavity optomechanics. This led to the speculation that if the radiation pressure backaction force could produce significant noise in a kg-mass mirror then it should be quite a significant force for micro or nano resonators. Since then many different physical systems spanning a wide range of masses and frequencies have been investigated and optomechanics has gained a momentum of its own in establishing itself as an independent research field [1, 4, 5].

Many theoretical predictions resulting from optomechanical coupling by radiation pressure have already been observed in different optomechanical setups e.g. static effects such as radiation pressure bistability [6] and optical spring effect [7] and dynamical effects such as optomechanical back action cooling used to cool cantilevers [8], microtoroids [9], and membranes[10].

With recent progress in micro and nano fabrication techniques it has become possible to design micro and nano mechanical resonators with very well defined properties. These engineered mechanical resonators can be of such high quality that it has become possible to operate some of these devices in the quantum regime using optomechanical interactions[11–13].

To name just a few, some of the interesting experiments proposed and currently being investigated within quantum cavity optomechanics are generation of squeezed states of light [14], optomechanical entanglement [15], fundamental test of quantum mechanics with massive objects [16]. In terms of practical applications, optomechanical setups can be used

as metrology and sensing tools such as optical-electrical transducer [17][18], tunable optical filters and switches [19], optical memory elements [20].

Quantum optomechanics requires systems which ideally can provide control over both the quantum state of the light and of the mechanical resonator. This requires high quality mechanical resonators with excellent optical properties, so they can be part of or integrated into high finesse optical resonators. High quality mechanical resonators are desired in optomechanical setups since they reduce the loss of oscillator energy to the environment and high finesse optical cavities are required to increase the optomechanical coupling. These requirements can be naturally fulfilled in the Membrane-in-the-middle (MIM) cavity optomechanical setup, as first demonstrated by Jack Harris's group at Yale [10].

In this setup, a dielectric membrane acting as the mechanical resonator is placed in the middle of a high finesse Fabry Perot cavity. The promising aspect of the MIM setup is to allow the integration of a low mass and high mechanical quality factor resonator with a high finesse optical resonator, thereby optimizing the single photon optomechanical coupling factor, which measures the strength of the optomechanical interaction.

Si_3N_4 membranes have shown to be excellent candidates for this kind of setup, due to their low mass ($\approx ng$), high mechanical quality factors ($Q_m \approx 10^7$) for megahertz frequencies [21] and very low optical absorption. MIM system employing Si_3N_4 membrane resonators was first successfully implemented by the Harris group at Yale, and in Kimble's group at Caltech. Since then this particular MIM setup is being studied extensively and used by several groups around the world [10, 17, 18, 22–30]. For example, some of the state-of-art experiments performed by the Regal group in University of Colorado involve using the Si_3N_4 membrane to cool down the motion of the resonator close to the quantum ground state [31], to generate squeezed states of light using optomechanical interaction [27], and to study fundamental aspects such as observing radiation pressure shot noise effects on the membrane [27]. One of the promising application for the MIM setup is to realize transducers between microwave and optical domain [18][17]. Another interesting direction is to make hybrid systems involving membranes and ions or ultracold atoms. Steps in this direction have already been taken in coupling cold atoms to membrane [23] and other proposals exist to realize hybrid optomechanical interface, for example, trapped ions [32] or doped systems [33].

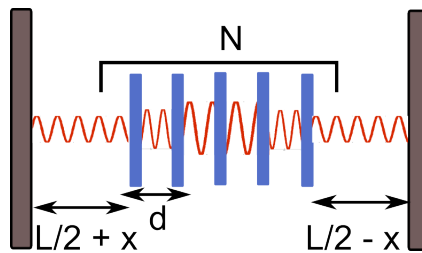
In parallel to improving the control of the motion of individual mechanical resonators, such as flexible membranes, collective optomechanical effects in multimode optomechanical systems are starting to attract a lot attention. Membrane-arrays for instance have been investigated theoretically for applications in sensing and multimode quantum optomechanics [34] and to study many body physics phenomena such as heat transport [35] and synchronization effects [36].

This work presents the first steps towards the investigation of collective optomechanics with membrane arrays and is presented in the following way :

- Chapter 2 : Introduces cavity and collective optomechanics through Transfer matrix method (TMM). TMM is a classical approach based on solving Maxwell's equations in one dimension that is used to analyze the propagation of electromagnetic waves

through layered media. We start by describing plane wave propagation in a lossless medium using Maxwell's equations and introduce the concept of forward and backward propagating electric fields. This discussion then introduces the concept of "transfer matrix" which is 2×2 matrix relating the forward-backward electric fields on one side of a dielectric interface to the other side.

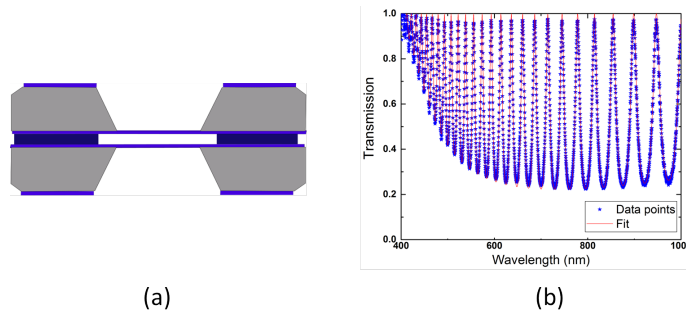
The TMM is then used to discuss the static optical properties of parallel dielectric slabs. Next, we introduce the canonical examples of a movable end-mirror and of a membrane-in-the-middle optomechanical setup, first classically and then quantum mechanically. Last, the theory needed to describe collective optomechanics of a periodic array of membranes is discussed, based on the work of [34][37].



Scheme showing N -membrane array at the middle of a planar cavity which form the basis for all our collective optomechanics discussion.

- Chapter 3 : Details the first steps towards the realization of few Si_3N_4 membrane-arrays. The chapter starts with single Si_3N_4 membrane characterization. In order to determine the single membrane parameters such as the thickness and refractive index of the Si_3N_4 membrane and spacer thicknesses, we use different characterization tools, such as ellipsometry, profilometer and Atomic force microscopy (AFM).

Next, we detail the fabrication of double membrane array systems with different membrane separations and perform optical transmission measurements using a broad band white light source and a monochromatic light source.



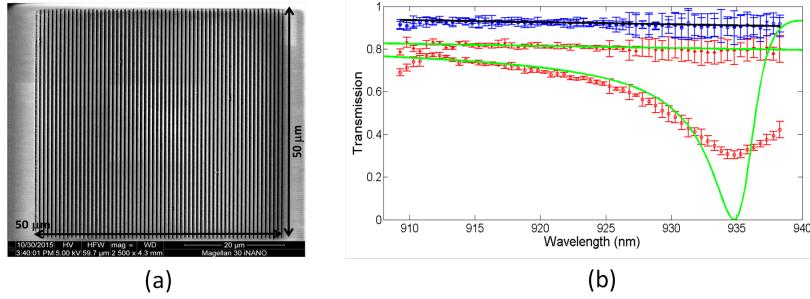
(a) shows a double-membrane array with a spacer distance of $8.5 \mu\text{m}$ and (b) the transmission spectrum for such an array obtained using white light source.

- Chapter 4 : Reports on the design and construction of setup for characterizing the mechanical properties of the membrane-arrays, as well as the design considerations for building the cavity optomechanics setup to be used in future experiments.

Furthermore, in this chapter we clarify an as yet untreated issue of thick dielectric membranes. We look into what happens when the effective thickness of the dielectric membrane is comparable to the wavelength of the incident light ($nl \approx \lambda$) and compare the optical and optomechanical properties of a thick membrane array with the thin membrane case [38].

- Chapter5 : Discusses the design, fabrication and optical characterization of sub-wavelength gratings (SWG) on Si_3N_4 membranes in order to increase their reflectivity and thereby the achievable optomechanical coupling strengths.

We begin the chapter by providing a brief outline of the Rigorous Coupled Wave Analysis (RCWA) which provides the theoretical framework necessary to understand SWG's. Next, we detail the simulation results obtained with Model Integrated Scattering Tool (MIST) for our specific grating structure on Si_3N_4 membranes. Following up, we describe the fabrication process for SWG on Si_3N_4 membranes using EBL and etching process. The Si_3N_4 grating-on-membrane is then characterized using SEM and other techniques to extract grating profile and grating parameters. Lastly, the gratings are characterized optically by measuring their transmission using a monochromatic light source.



(a) shows a SEM image of grating on Si_3N_4 membrane and (b) the transmission spectrum for the grating in (a) obtained using a monochromatic light source.

- Chapter 6 : Provides a theoretical investigation of hybrid optomechanics of a doped membrane in a cavity setup. The chapter is based on our published work [33].

Chapter 2

Cavity optomechanics with movable reflectors

Cavity optomechanics studies the interaction between electromagnetic radiation in a optical resonator and mechanical motion. In an optomechanical setup, the optical field within a cavity can influence the motion of micro-or-nano sized resonators through radiation pressure forces.

In section 2.1 we introduce the first basic constituent of an optomechanical setup, the planar Fabry Perot cavity and investigate its optical properties using the Transfer Matrix Method (TMM). In section 2.2 we introduce, the mechanical resonator which forms the movable part of the optomechanical setup. The two parts are combined and studied as a Membrane-in-the-Middle (MIM) setup in section 2.3. Such a setup is a versatile optomechanical platform which has been employed in various experiments and proposed to have many applications[10, 17, 18, 22, 24–30, 35]. In section 2.4, we introduce the concept of collective optomechanics where, instead of a single membrane, we investigate the optical and optomechanical properties of a periodic array of such membranes, which motivates most of the work of this thesis. In this chapter we use exclusively a 1D treatment, which is convenient for illustration purposes and allowing for tractable calculations. Aspects departing from the considered 1D geometry, due to e.g. the Gaussian nature of the beams, will be discussed in chapters 2 and 3.

2.1 Planar Fabry Perot cavity

2.1.1 Propagation of plane electromagnetic waves in lossless medium

Consider the propagation of uniform plane waves in the z -direction in a lossless medium characterized by its electric permittivity ϵ and magnetic permeability μ . Uniformity means that the electric and magnetic fields are not dependent on the transverse (x, y) coordinates, but the fields are a function of only (z, t) : $\mathbf{E}(x, y, z, t) = \mathbf{E}(z, t)$ and $\mathbf{H}(x, y, z, t) = \mathbf{H}(z, t)$.

Since there is no dependence of the electric and magnetic fields on x, y the vector

differential operations reduce to

$$\nabla = \hat{\mathbf{z}} \frac{\partial}{\partial z}, \nabla \cdot \mathbf{E} = \frac{\partial E_z}{\partial z}, \nabla \times \mathbf{E} = \hat{\mathbf{z}} \times \frac{\partial \mathbf{E}}{\partial z} = -\hat{\mathbf{x}} \frac{\partial E_y}{\partial z} + \hat{\mathbf{y}} \frac{\partial E_x}{\partial z} \quad (2.1)$$

Assuming an electric displacement vector $\mathbf{D} = \epsilon \mathbf{E}$ and a magnetic field $\mathbf{B} = \mu \mathbf{H}$, Maxwell's equations can be written as

$$\begin{aligned} \nabla \times \mathbf{E} &= -\mu \frac{\partial \mathbf{H}}{\partial t} \\ \nabla \times \mathbf{H} &= \epsilon \frac{\partial \mathbf{E}}{\partial t} \\ \nabla \cdot \mathbf{E} &= 0 \\ \nabla \cdot \mathbf{H} &= 0 \end{aligned} \quad (2.2)$$

Using equation 2.1 in 2.2 we get

$$\begin{aligned} \hat{\mathbf{z}} \times \frac{\partial \mathbf{E}}{\partial z} &= -\mu \frac{\partial \mathbf{H}}{\partial t} \\ \hat{\mathbf{z}} \times \frac{\partial \mathbf{H}}{\partial z} &= \epsilon \frac{\partial \mathbf{E}}{\partial t} \\ \frac{\partial E_z}{\partial z} &= 0 \\ \frac{\partial H_z}{\partial z} &= 0 \end{aligned} \quad (2.3)$$

As a consequence of uniformity \mathbf{E} and \mathbf{H} do not have components along z -direction ($E_z = H_z = 0$). Using $\hat{\mathbf{z}} \cdot (\hat{\mathbf{z}} \times \mathbf{a})$ we get,

$$\hat{\mathbf{z}} \cdot \left(\hat{\mathbf{z}} \times \frac{\partial \mathbf{H}}{\partial z} \right) = \epsilon \hat{\mathbf{z}} \cdot \frac{\partial \mathbf{E}}{\partial t} = 0 \Rightarrow \frac{\partial E_z}{\partial t} = 0 \quad (2.4)$$

As $\frac{\partial E_z}{\partial z} = 0$ and $\frac{\partial E_z}{\partial t} = 0$, E_z is a constant independent of z, t and, excluding static solutions, we take $E_z = 0$. Similarly, $H_z = 0$ and the fields have components only in the x, y direction given by:

$$\begin{aligned} \mathbf{E}(z, t) &= \hat{\mathbf{x}} E_x(z, t) + \hat{\mathbf{y}} E_y(z, t) \\ \mathbf{H}(z, t) &= \hat{\mathbf{x}} H_x(z, t) + \hat{\mathbf{y}} H_y(z, t) \end{aligned} \quad (2.5)$$

The transverse fields in 2.5 must satisfy Faraday's and Ampere's laws in 2.3. For propagation of the electromagnetic waves in a medium with impedance η , ϵ and μ are related to the speed of light in vacuum c by

$$\epsilon = \frac{1}{\eta c}, \mu = \frac{\eta}{c} \text{ where } c = \frac{1}{\sqrt{\mu \eta}}, \eta = \sqrt{\frac{\mu}{\epsilon}} \quad (2.6)$$

Now, using equation 2.6 in 2.5, we get

$$\begin{aligned}\hat{\mathbf{z}} \times \frac{\partial \mathbf{E}}{\partial z} &= -\frac{1}{c} \eta \frac{\partial \mathbf{H}}{\partial t} \\ \eta \hat{\mathbf{z}} \times \frac{\partial \mathbf{H}}{\partial z} &= \frac{1}{c} \frac{\partial \mathbf{E}}{\partial t}\end{aligned}\quad (2.7)$$

Using the BAC-CAB rule and the fact $\hat{\mathbf{z}} \cdot \frac{\partial \mathbf{E}}{\partial z} = 0$ and $\hat{\mathbf{z}} \cdot \hat{\mathbf{z}} = 1$,

$$\left(\hat{\mathbf{z}} \times \frac{\partial \mathbf{E}}{\partial z} \right) \times \hat{\mathbf{z}} = \frac{\partial \mathbf{E}}{\partial z} (\hat{\mathbf{z}} \cdot \hat{\mathbf{z}}) - \hat{\mathbf{z}} \left(\hat{\mathbf{z}} \cdot \frac{\partial \mathbf{E}}{\partial z} \right) = \frac{\partial \mathbf{E}}{\partial z} \quad (2.8)$$

Hence, equation 2.7 can be reduced to an equivalent system given by the coupled equations

$$\begin{aligned}\frac{\partial \mathbf{E}}{\partial z} &= -\frac{1}{c} \frac{\partial}{\partial t} (\eta \mathbf{H} \times \hat{\mathbf{z}}) \\ \frac{\partial}{\partial z} (\eta \mathbf{H} \times \hat{\mathbf{z}}) &= -\frac{1}{c} \frac{\partial \mathbf{E}}{\partial t}\end{aligned}\quad (2.9)$$

This system of coupled equations can be decoupled by introducing the forward and backward propagating electric fields defined as:

$$\begin{aligned}\mathbf{E}_+ &= \frac{1}{2} (\mathbf{E} + \eta \mathbf{H} \times \hat{\mathbf{z}}) \\ \mathbf{E}_- &= \frac{1}{2} (\mathbf{E} - \eta \mathbf{H} \times \hat{\mathbf{z}})\end{aligned}\quad (2.10)$$

Inverting equation 2.10, we deduce

$$\begin{aligned}\mathbf{E}(z, t) &= \mathbf{E}_+(z, t) + \mathbf{E}_-(z, t) \\ \mathbf{H}(z, t) &= \frac{1}{\eta} \hat{\mathbf{z}} \times [\mathbf{E}_+(z, t) - \mathbf{E}_-(z, t)]\end{aligned}\quad (2.11)$$

where $\mathbf{E}_+(z, t)$ is the forward propagating wave (in the positive z -direction) and $\mathbf{E}_-(z, t)$ is the backward propagating wave (in the negative z -direction).

Using the forward and backward propagating fields, the system of coupled equations 2.9 decouples into

$$\begin{aligned}\frac{\partial \mathbf{E}_+}{\partial z} &= -\frac{1}{c} \frac{\partial \mathbf{E}_+}{\partial t} \\ \frac{\partial \mathbf{E}_-}{\partial z} &= +\frac{1}{c} \frac{\partial \mathbf{E}_-}{\partial t}\end{aligned}\quad (2.12)$$

For uniform monochromatic plane waves propagating in a lossless medium with harmonic time dependence we get:

$$\begin{aligned}\mathbf{E}(z, t) &= \mathbf{E}(z) e^{-i\omega t} \\ \mathbf{H}(z, t) &= \mathbf{H}(z) e^{-i\omega t}\end{aligned}\quad (2.13)$$

Using 2.12 in equation 2.11 and by replacing $\frac{\partial}{\partial t} \rightarrow -i\omega$ then equations 2.11 becomes first-order differential equations:

$$\frac{\partial \mathbf{E}_\pm(z)}{\partial z} = \pm ik \mathbf{E}_\pm(z) \quad (2.14)$$

where $k = \frac{\omega}{c}$, with solutions given by

$$\begin{aligned}\mathbf{E}_+(z) &= \mathbf{E}_{0+} e^{ikz} \\ \mathbf{E}_-(z) &= \mathbf{E}_{0-} e^{-ikz}\end{aligned}\quad (2.15)$$

where $\mathbf{E}_{0\pm}$ are arbitrary complex valued constant vectors such that $\hat{\mathbf{z}} \cdot \mathbf{E}_{0\pm} = 0$. The corresponding magnetic field components are

$$\begin{aligned}\mathbf{H}_+(z) &= \frac{1}{\eta} \hat{\mathbf{z}} \times \mathbf{E}_+(z) = \frac{1}{\eta} (\hat{\mathbf{z}} \times \mathbf{E}_{0+}) e^{ikz} \\ \mathbf{H}_-(z) &= -\frac{1}{\eta} \hat{\mathbf{z}} \times \mathbf{E}_-(z) = -\frac{1}{\eta} (\hat{\mathbf{z}} \times \mathbf{E}_{0-}) e^{-ikz}\end{aligned}\quad (2.16)$$

Using 2.15 in 2.11 one obtains the general solution for single frequency plane waves, as a superposition of forward and backward propagating components:

$$\begin{aligned}\mathbf{E}(z) &= \mathbf{E}_{0+} e^{ikz} + \mathbf{E}_{0-} e^{-ikz} \\ \mathbf{H}(z) &= \frac{1}{\eta} \hat{\mathbf{z}} \times [\mathbf{E}_{0+} e^{ikz} - \mathbf{E}_{0-} e^{-ikz}]\end{aligned}\quad (2.17)$$

Equation 2.17 can also be rewritten as

$$\begin{aligned}E_+(z) &= \frac{1}{2} [E(z) + \eta H(z)] \\ E_-(z) &= \frac{1}{2} [E(z) - \eta H(z)]\end{aligned}\quad (2.18)$$

In the next section, we discuss what happens when a monochromatic plane wave impinges on a dielectric medium interface at normal incidence.

2.1.2 Plane waves at a dielectric interface

Consider a planar dielectric interface in the x, y plane fixed at some z location separating two dielectric media with complex valued characteristic impedances η, η' , as shown in figure 2.1

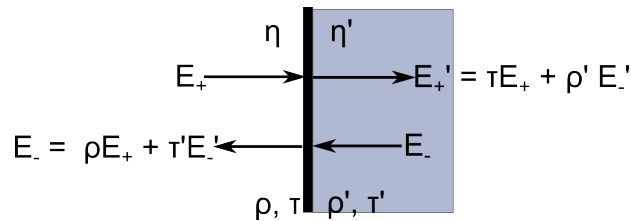


Figure 2.1: Scheme showing a dielectric interface between two media with characteristic impedances η, η' and amplitude reflection and transmission coefficients ρ, ρ' and τ, τ' , respectively

For a field propagation as shown in figure 2.1, the boundary condition implies that the total electric and magnetic fields must be continuous at the interface

$$\begin{aligned} E &= E' \\ H &= H' \end{aligned} \quad (2.19)$$

Expressing 2.19 in terms of forward and backward electric fields, one gets

$$\begin{aligned} E_+ + E_- &= E'_+ + E'_- \\ \frac{1}{\eta}(E_+ + E_-) &= \frac{1}{\eta}(E'_+ - E'_-) \end{aligned} \quad (2.20)$$

Rewriting equation 2.20 in matrix form, we get :

$$\begin{bmatrix} E_+ \\ E_- \end{bmatrix} = \frac{1}{\tau} \begin{bmatrix} 1 & \rho \\ \rho & 1 \end{bmatrix} \begin{bmatrix} E'_+ \\ E'_- \end{bmatrix} \quad (2.21)$$

or, inversely,

$$\begin{bmatrix} E'_+ \\ E'_- \end{bmatrix} = \frac{1}{\tau'} \begin{bmatrix} 1 & \rho' \\ \rho' & 1 \end{bmatrix} \begin{bmatrix} E_+ \\ E_- \end{bmatrix} \quad (2.22)$$

where ρ, τ and ρ', τ' are the reflection and transmission coefficients from the left and right of interface defined with η, η' respectively

$$\begin{aligned} \rho &= \frac{\eta' - \eta}{\eta' + \eta}, & \tau &= \frac{2\eta'}{\eta' + \eta} \\ \rho' &= \frac{\eta - \eta'}{\eta + \eta'}, & \tau' &= \frac{2\eta}{\eta + \eta'} \end{aligned} \quad (2.23)$$

For $\eta = \eta_0/n$ and $\eta' = \eta_0/n'$, where n, n' are the refractive indices, we get the Fresnel coefficients at normal incidence

$$\begin{aligned} \rho &= \frac{n - n'}{n + n'}, & \tau &= \frac{2n}{n + n'} \\ \rho' &= \frac{n' - n}{n' + n}, & \tau' &= \frac{2n'}{n' + n} \end{aligned} \quad (2.24)$$

In the next section we are going to apply the above concepts to investigate reflection and transmission through a dielectric slab.

2.1.3 Single dielectric slab

Consider a dielectric slab as shown in figure 2.2 of length l and refractive index n . There are two interfaces in this situation, the left medium and the right medium that is vacuum with $n = 1, \eta_0$ separated by the dielectric slab η . Within the slab, the propagation number $k = \omega/c$ and wavelength $\lambda = 2\pi/k$. Also, $\lambda = \lambda_0/n$ where λ_0 is the free space wavelength.

The incident, reflected and transmitted wave directions are as shown in figure 2.2. The forward and backward propagating waves are related by the transfer matrix

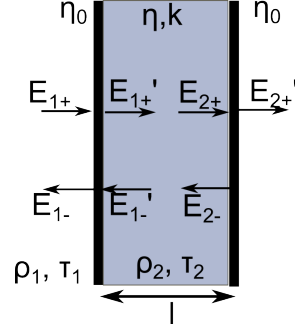


Figure 2.2: Scheme showing a dielectric slab with characteristic impedance η and thickness l between two medium with characteristic impedances η_0

$$\begin{bmatrix} E_{1+} \\ E_{1-} \end{bmatrix} = \underbrace{\frac{1}{\tau_1} \begin{bmatrix} 1 & \rho_1 \\ \rho_1 & 1 \end{bmatrix}}_{M_{\text{vacuum/dielectric}}} \underbrace{\begin{bmatrix} e^{-ikl} & 0 \\ 0 & e^{ikl} \end{bmatrix}}_{M_{\text{dielectric slab}}} \underbrace{\frac{1}{\tau_2} \begin{bmatrix} 1 & \rho_2 \\ \rho_2 & 1 \end{bmatrix}}_{M_{\text{dielectric/vacuum}}} \begin{bmatrix} E_{2+}' \\ 0 \end{bmatrix} \quad (2.25)$$

The transfer function for the dielectric slab can be given by:

$$M_{\text{slab}} = M_{\text{vacuum/dielectric}} M_{\text{dielectric slab}} M_{\text{dielectric/vacuum}} \quad (2.26)$$

For a general transfer matrix system given by :

$$M = \begin{bmatrix} m_{11} & m_{12} \\ m_{21} & m_{22} \end{bmatrix} \quad (2.27)$$

we define the complex amplitude transmissivity of the system as $t_m = \frac{1}{m_{22}}$ and amplitude reflectivity $r_m = \frac{m_{12}}{m_{22}}$.

The reflection and transmission coefficients of the membrane are then given by [34, 39]

$$r_m = \frac{\rho(1 - e^{2iknl})}{1 - \rho^2 e^{2iknl}}, \quad \text{and} \quad t_m = \frac{\tau_1 \tau_2 e^{iknl}}{1 - \rho^2 e^{2iknl}}. \quad (2.28)$$

The equivalent membrane polarizability $\zeta \equiv -ir_m/t_m$ is then

$$\zeta = \frac{n^2 - 1}{2n} \sin(knl). \quad (2.29)$$

Eqs. (2.26)–(2.29) hold for any membrane thickness.

Here, we model the dielectric slab as a scatterer that interacts linearly with the electromagnetic field and is defined by the polarizability ζ which is real for lossless medium and complex for lossy medium. Polarizability is related to amplitude reflectivity as :

$$r = \frac{i\zeta}{1 - i\zeta} \quad (2.30)$$

and for a lossless scatterer we get

$$|r|^2 = \frac{\zeta^2}{1 + \zeta^2} \quad (2.31)$$

For a dielectric slab whose thickness l is much less than the wavelength of incident light λ , then the slab is treated as a single element defined by polarizability ζ and a transfer matrix given by

$$M_m(\zeta) = \begin{bmatrix} 1 + i\zeta & i\zeta \\ -i\zeta & 1 - i\zeta \end{bmatrix} \quad (2.32)$$

where ζ is given by Eq. (4.12), which gives reflection and transmission coefficients having the same amplitude as that of the equivalent membrane having arbitrary thickness.

In the above discussion, we have considered a dielectric slab and introduced transfer matrix method to define the optical properties of the slab. In a limit where the thickness of the slab is much less than the wavelength of the light ($l \ll \lambda$), we can assume the dielectric slab to be a thin membrane, defined by the transfer matrix 2.32 and conveniently characterized by a single parameters, ζ .

In the next section, we are going to use transfer matrix method to determine optical properties of a planar Fabry Perot cavity.

2.1.4 Multiple reflector systems : Planar Fabry Perot cavity

In this section we consider the optical properties of systems consisting of more than one reflector (dielectric element) in a 1D scenario. For multiple reflector systems we use the fact that the optical properties of the whole system can be given by an overall transfer matrix which is the product of the transfer matrices representing individual elements of the multiple reflector system.

As an example, consider a planar Fabry Perot cavity consisting of two mirrors with amplitude transmittivity t_1, t_2 and amplitude reflectivity r_1, r_2 separated by a distance L as shown in figure 2.3 in vacuum. For simplicity we consider incident light to be at normal incidence.

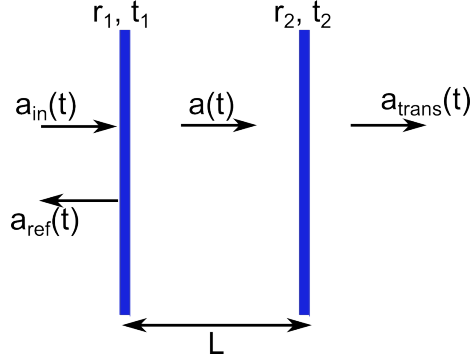


Figure 2.3: Scheme showing a planar Fabry Perot cavity of length L with input and output mirror reflectivity and transmissivity given by r_1, t_1 and r_2, t_2 respectively

The overall transfer matrix for this optical system is given by:

$$\mathbf{M}_{FP} = \underbrace{\frac{1}{t_1} \begin{bmatrix} 1 & r_1 \\ r_1 & 1 \end{bmatrix}}_{M_{mirror1}} \underbrace{\begin{bmatrix} e^{-ik_0L} & 0 \\ 0 & e^{ik_0L} \end{bmatrix}}_{M_{free\ space}} \underbrace{\frac{1}{t_2} \begin{bmatrix} 1 & r_2 \\ r_2 & 1 \end{bmatrix}}_{M_{mirror2}} \quad (2.33)$$

From above equation 2.33 and previously defined transmittance, $t = \frac{1}{M_{22}}$, we get the transmission for the Fabry Perot

$$T_{FP} = |t_{FP}|^2 = \frac{|t_1 t_2|^2}{|1 - r_1 r_2 e^{2k_0 L}|^2} \quad (2.34)$$

For identical mirrors reflectivities $R = |r_1|^2 = |r_2|^2$ we get

$$T_{FP} = \frac{(1 - R)^2}{1 + R^2 - 2R \cos(\phi)} \quad (2.35)$$

where $\phi = 2k_0 L$ and $k_0 = 2\pi/\lambda_0$.

Simplifying equation 2.35 we get the well-known Airy function transmission function

$$T_{FP} = \frac{1}{1 + F \sin^2(\frac{\phi}{2})} \quad (2.36)$$

where $F = \frac{4R}{(1-R^2)^2}$ is the coefficient of finesse.

Plotting this function with wavelength gives the transmission cavity spectrum shown in figure 2.4.

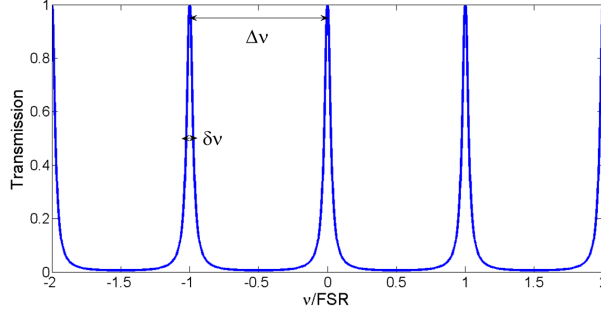


Figure 2.4: Symmetric Fabry Perot cavity transmission spectrum for a cavity of Finesse $\mathcal{F} = 20$

Due to the interference between the forward and backward propagating waves, the intracavity electric field builds up when the laser wavelength is close to a cavity resonance wavelength, which corresponds to $m\lambda = 2L$, where m is an integer.

The distance between two consecutive peaks in frequency is the Free Spectral Range FSR .

$$FSR \equiv \Delta\nu = \frac{c}{2L} \quad (2.37)$$

Using 2.37 we define another quantity called the Finesse \mathcal{F} defined as

$$\mathcal{F} = \frac{\Delta\nu}{\delta\nu} \quad (2.38)$$

where $\Delta\nu \equiv FSR$ and $\delta\nu$ is the Full Width at Half Maximum (FWHM) of a transmission peak.

For mirrors with $R > 0.5$ the Finesse is given by

$$\mathcal{F} \approx \frac{\pi R^{1/2}}{1 - R} \quad (2.39)$$

and for unequal mirror reflectivities R_1, R_2 the finesse is

$$\mathcal{F} \approx \frac{\pi(R_1 R_2)^{1/4}}{1 - (R_1 R_2)^{1/2}} \quad (2.40)$$

Qualitatively, the finesse of such a cavity gives a measure of how many round trips a photon makes on average inside the cavity before leaving and hence determines the resonant build up power inside the cavity.

2.1.4.1 Dynamics of the field in a high-finesse Fabry Perot resonator

We now consider a high finesse cavity for which $R_1, R_2 \rightarrow 1$ and use an input-output theory to describe the cavity field dynamics. While classical here, this formalism can then be easily extended to the quantum mechanical description. We consider an empty cavity with

an incoming field amplitude $a_{in}(t)$, an intra-cavity field amplitude $a(t)$, a transmitted field amplitude $a_{trans}(t)$ and reflected field amplitude $a_{ref}(t)$.

The incoming field and the outgoing field amplitudes are then related at the first mirror by

$$a(t) = t_1 a_{in}(t) + r_1 r_2 a'(t - \tau) e^{i\phi} \quad (2.41)$$

where $\tau = \frac{2L}{c}$ is the round trip time for a photon and $\phi = (\omega_L - \omega_c)\tau = -\Delta_c \tau$ is the phase change after one round trip when the driving laser frequency is ω_L and the nearest cavity resonance frequency is ω_c .

At first order in $\phi, 1 - r_1, 1 - r_2$ equation 2.41 gives the dynamical equation for the field amplitude inside the cavity

$$\dot{a}(t) = -(\kappa + i\Delta_c)a(t) + \sqrt{\frac{2\kappa_1}{\tau}} a_{in}(t) \quad (2.42)$$

where $\kappa = \kappa_1 + \kappa_2$, $\kappa_i = \frac{|t_i|^2}{2\tau}$ and a_{in} is the field coupled into the cavity from the input mirror and $a(t)$ is the intracavity field.

Solving equation 2.42 in the steady state we get:

$$\bar{a} = \frac{\sqrt{2\kappa_1} \bar{a}_{in}}{(\kappa + i\Delta_c)} \quad (2.43)$$

and the transmission through the output mirror is then a lorentzian function of the detuning

$$T = \left| \frac{a_{trans}}{a_{in}} \right|^2 = \frac{4\kappa_1\kappa_2}{\kappa^2 + \Delta_c^2} \quad (2.44)$$

where $a_{trans} = \sqrt{2\kappa_2} \bar{a}$ is the transmitted field through the output mirror.

The advantage of using input-output theory for describing dynamics of field amplitudes in a Fabry Perot cavity is that it can be easily extended to the quantum regime by using annihilation and creation field operators instead of the classical field amplitudes.

$$a \rightarrow \hat{a}, \quad a_{in} \rightarrow \hat{a}_{in}, \text{ etc.} \quad (2.45)$$

with commutator relations given by

$$[\hat{a}, \hat{a}^\dagger] = 1, \quad [\hat{a}_{in}(t), \hat{a}_{in}(t')^\dagger] = \delta(t - t') \quad (2.46)$$

So far we have treated the optical properties of *stationary* planar Fabry Perot resonators first using the Transfer matrix method (TMM) and then using input-output relations in the high finesse cavity limit. In the next section 2.2 we discuss what happens when one of the end mirrors of the cavity is movable.

2.2 Fabry Perot cavity with movable end mirror

In this section we discuss the dynamics of a mechanical resonator constituting the end mirror of a Fabry Perot cavity, first in the case of empty cavity, that is without the presence of optical fields and, second, in the presence of a coherent monochromatic laser drive. The movable end mirror Fabry Perot cavity is as shown in figure 2.5, which is considered to be a suspended membrane with vibrational drum modes. In the very underdamped and well separated mode regime, we consider a single mechanical vibrational mode of frequency ω_m .

2.2.1 Mechanical resonator

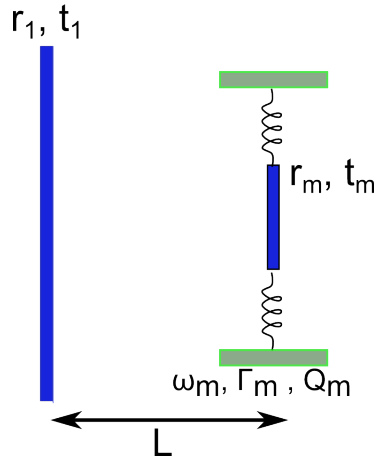


Figure 2.5: Fabry Perot cavity with a movable end mirror which is a suspended dielectric membrane.

The equation of motion describing the displacement amplitude of this mode is given by

$$m\ddot{x} + m\Gamma_m\dot{x} + m\omega_m^2x(t) = F_T \quad (2.47)$$

where m is the effective mass of the mode considered [40], Γ_m is the mechanical damping rate which gives the loss of the mechanical energy to the environment, $x(t)$ is the displacement and F_T is the thermal fluctuation force.

The mechanical quality factor of the membrane is an important parameter defined as

$$Q_m = \frac{\omega_m}{\Gamma_m} \quad (2.48)$$

Taking the Fourier transform of 2.47 ($x(\omega) = \int_{-\infty}^{\infty} x(t)e^{-i\omega t} dt$), the mechanical susceptibility can be defined as

$$\chi_m(\omega) \equiv \frac{x(\omega)}{F_T(\omega)} = \frac{m^{-1}}{\omega_m^2 - \omega^2 + \pi i\omega\Gamma_m} \quad (2.49)$$

For a stationary process the noise spectrum of the position fluctuation is given by

$$S_x(\omega) = \langle |x(\omega)|^2 \rangle = |\chi_m(\omega)|^2 S_{\text{FT}} \quad (2.50)$$

where S_{FT} is the noise spectra of the thermal force.

In the case of weak damping ($\Gamma_m \ll \omega_m$), equation 2.50 gives Lorentzian peaks with Half width at half maximum (HWHM) to be Γ_m located at $\omega = \pm\omega_m$. The area under the peaks gives a measure of the oscillator energy or temperature T in the mode since, according to equipartition theorem, $\frac{1}{2}\omega_m^2 \langle x^2 \rangle = \frac{1}{2}k_B T$.

2.2.2 Mechanical resonator in the presence of radiation pressure force

Consider the setup shown in figure 2.6 with perfectly reflecting mirrors ($r_1, r_m \rightarrow 1$), where one of the end mirrors forming the cavity is the mechanical resonator. In this scheme the cavity is driven with monochromatic light at ω_L .

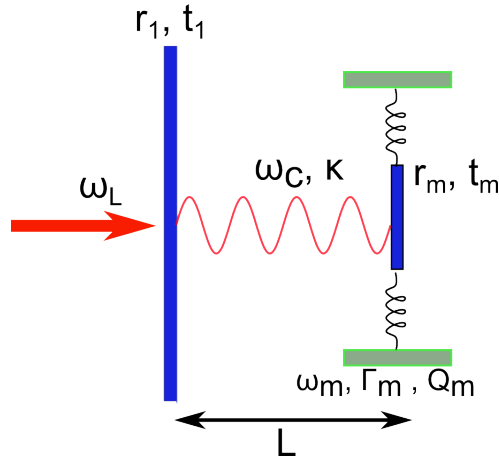


Figure 2.6: Fabry Perot cavity with a movable end mirror which is a suspended dielectric membrane. The cavity is driven with monochromatic laser beam at a frequency of ω_L

The coupling between the mechanical motion of the membrane and the optical cavity field is due to the radiation pressure force. Neglecting absorption in the movable mirror, the radiation pressure results from the momentum transfer of reflected photons in the cavity and has the form

$$F_{rp} = N \frac{\Delta P}{\tau_c} = N \hbar \frac{\omega_c(x)}{L} \quad (2.51)$$

where ΔP is the change in momentum and $\tau_c = \frac{2L}{c}$ is the roundtrip time for a photon inside the cavity of length L and N is number of photons circulating in the cavity.

In this model, when the input optical power is resonant with a cavity mode, the circulating optical power is optimum which exerts a force on the movable mirror. And

the mirror displacement causes a new optical round trip condition, which modifies the detuning of the cavity resonance with respect to the incident field. This interaction is a non-linear process and for high mechanical and optical quality factor systems, it can result in dynamical actions such as mechanical resonator cooling and amplification [4].

At the lowest order in the displacement, the cavity frequency is linearly shifted and $F_{\text{rp}} = \hbar G |a|^2$ where $G = \frac{\omega_c}{L}$ is known as the frequency pull parameter.

One then gets the coupled equations of motion for the system,

$$m\ddot{x}(t) + m\Gamma_m \dot{x}(t) + m\omega_m^2 x(t) = F_T(t) + F_{\text{rp}}(t) \quad (2.52)$$

$$\dot{a}(t) = (i(-\Delta_c + Gx(t)) - \kappa)a(t) + \sqrt{2\kappa_1} \quad (2.53)$$

where the radiation pressure force is given by $F_{\text{rp}}(t) = \hbar G |a|^2$, $x(t)$ is the amplitude of vibration and is always real, and $a(t)$ is the amplitude of the intracavity field which is complex.

The dynamics of the system can be studied by looking at the fluctuations around its steady state values, assuming there is one. Linearizing the system of equations 2.52 and 2.53 where each variable is decomposed as the sum of its steady state mean value and a small time dependent fluctuating term,

$$x(t) = \bar{x} + \delta x(t) \quad (2.54)$$

$$a(t) = \bar{a} + \delta a(t) \quad (2.55)$$

gives,

$$m\delta\ddot{x}(t) + m\Gamma_m \delta\dot{x}(t) + m\omega_m^2 \delta x(t) = \delta F_T(t) + \delta F_{\text{rp}}(t) \quad (2.56)$$

$$\delta\dot{a}(t) = iG(\bar{x}\delta a + \delta x\bar{a}) - i\Delta_c \delta a - \kappa \delta a \quad (2.57)$$

Taking the fourier transform of equation 2.57, one gets

$$\frac{\delta a(\omega)}{\delta x(\omega)} = \frac{\bar{a}}{\frac{-\Delta_c - \omega + i\kappa}{G} + \bar{x}} \quad (2.58)$$

where $\bar{a} = \frac{\sqrt{2\kappa_1 \bar{a}_{in}}}{(\kappa + i\Delta_c)}$ and $\bar{x} = \frac{\langle F_{\text{rp}} \rangle}{m\omega_m^2}$.

Fourier transforming equation 2.56 gives,

$$-m\omega^2 \delta x(\omega) + im\omega\Gamma_m \delta x(\omega) + m\omega_m^2 \delta x(\omega) = \delta F_T(\omega) + \delta F_{\text{Rp}}(\omega) \quad (2.59)$$

where $\delta F_{\text{rp}}(\omega) = G(\bar{a}^*(\omega)\delta a(\omega) + \bar{a}(\omega)\delta a^*(\omega))$. One can define the effective mechanical susceptibility χ_{eff} as

$$\chi_{\text{eff}}^{-1}(\omega) = \frac{\delta F(\omega)}{\delta x(\omega)} = \omega_m^2 - \omega^2 + im\omega\Gamma_m - \frac{G}{m}(\bar{a}^* \delta a + \bar{a} \delta a^*) \quad (2.60)$$

Using equation 2.58 in equation 2.59, the optomechanical damping rate at the mechanical resonance frequency, ($\omega = \omega_m$), is defined by

$$\Gamma_{\text{opt}} = \frac{G}{m} \text{Im} \frac{[\bar{a}^*(\omega_m)\delta a(\omega_m) + \bar{a}(\omega_m)\delta a^*(\omega_m)]}{\omega_m} \quad (2.61)$$

$$= \frac{-G^2|a|^2\kappa}{m\omega_m} \left\{ \frac{1}{(-\Delta_c + \omega_m - G\bar{x})^2 + \kappa^2} - \frac{1}{(-\Delta_c - \omega_m - G\bar{x})^2 + \kappa^2} \right\} \quad (2.62)$$

Therefore the total effective mechanical damping rate is expressed as,

$$\Gamma_{\text{eff}} = \Gamma_m + \Gamma_{\text{opt}} \quad (2.63)$$

where Γ_{opt} can be either positive or negative and hence can either increase or decrease the total mechanical damping rate of the resonator leading to either cooling or heating of the mechanical resonator.

Taking the real part of the effective susceptibility at $\omega = \omega_m$ gives the optical spring term,

$$\delta\omega_m = \frac{G}{m\omega_c} \text{Re} \frac{[\bar{a}^*(\omega_m)\delta a(\omega_m) + \bar{a}(\omega_m)\delta a^*(\omega_m)]}{\omega_m} \quad (2.64)$$

which gives the shift in the mechanical resonance frequency of the oscillator induced by the light field and is known as the ‘‘Optical Spring effect’’.

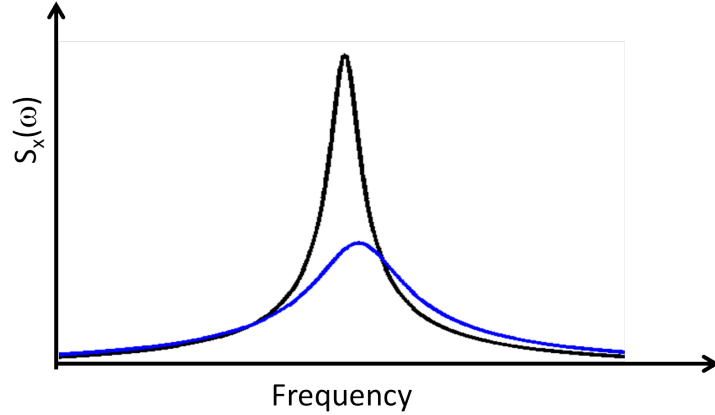


Figure 2.7: Schematic presentation to see the optomechanical cooling and optical spring effect as a function of frequency. The relative temperature of the system decreases from black to blue, where black represents mechanical spectra without radiation pressure force and blue is with radiation pressure force. We can clearly see the linewidth of the blue spectra increasing and the area under the curve decreasing showing the optomechanical cooling effect. The mechanical frequency shifts showing the optical spring effect.

In the next section, we extend the above description to the quantum regime where we use a Hamiltonian formulation to describe the interaction between optical cavity and movable mirrors using field operators.

2.2.2.1 Quantum regime : Hamiltonian formulation

We start by considering the uncoupled optical and mechanical modes to be approximated as quantum harmonic oscillators, where the Hamiltonian for the system is given as [1]

$$\hat{H}_0 = \hbar\omega_c\hat{a}^\dagger\hat{a} + \hbar\omega_m\hat{b}^\dagger\hat{b} \quad (2.65)$$

where \hat{b} and \hat{b}^\dagger are the annihilation and creation operators for the quantized motional mode considered, satisfying $[\hat{b}, \hat{b}^\dagger] = 1$.

Since the coupling of optical and mechanical modes is parametric, we get that the cavity resonance frequency is shifted to the lowest order by the mechanical amplitude as

$$\omega_c(x) \approx \omega_c + x \frac{\partial\omega_c}{\partial x} + \dots \quad (2.66)$$

where we define $G = -\frac{\partial\omega_c}{\partial x}$ as the optical frequency shift per displacement. For a linear Fabry Perot cavity of length L with a perfectly reflecting movable end-mirror, $G = \omega_c/L$

Within the linear approximation, substituting equation 2.66 in 2.65, we get

$$\hbar\omega_c(x)\hat{a}^\dagger\hat{a} \approx \hbar(\omega_c - Gx)\hat{a}^\dagger\hat{a} \quad (2.67)$$

The mechanical mode operator is quantized in terms of phonon creation and annihilation operators

$$\hat{x} = x_{ZPF}(\hat{b} + \hat{b}^\dagger) \quad (2.68)$$

where x_{ZPF} is the zero point fluctuation of the mechanical oscillator defined as $x_{ZPF} = \sqrt{\frac{\hbar}{m_{eff}\omega_m}}$.

The interaction hamiltonian is then given by

$$\hat{H}_{int} = -\hbar g_0 \hat{a}^\dagger \hat{a} (\hat{b} + \hat{b}^\dagger) \quad (2.69)$$

where $g_0 = Gx_{ZPF}$ is the vacuum optomechanical coupling strength which gives the interaction strength in terms of frequency shift between a single photon and a single phonon.

The radiation pressure force is given by the derivative of the interaction Hamiltonian: [1]

$$\hat{F} = -\frac{d\hat{H}_{int}}{d\hat{x}} = \hbar G \hat{a}^\dagger \hat{a} = \hbar \frac{g_0}{x_{ZPF}} \hat{a}^\dagger \hat{a} \quad (2.70)$$

The full Hamiltonian for this system involves dissipation terms such as optical losses and mechanical damping, fluctuation terms that take into account the fluctuation of thermal phonons and photons fluctuations in the optical field.

We consider the optical mode in the rotating frame at a laser frequency ω_L , where the unitary transformation $\hat{U} = e^{i\omega_L \hat{a}^\dagger \hat{a} t}$ makes the driving terms time-independent and gives the Hamiltonian

$$\hat{H} = \hat{U}(\hat{H}_0 + \hat{H}_{int})\hat{U}^\dagger + i\hbar\partial\hat{U}/\partial t \quad (2.71)$$

simplifying to

$$\hat{H} = \hbar\Delta_c\hat{a}^\dagger\hat{a} + \hbar\omega_m\hat{b}^\dagger\hat{b} - \hbar g_0\hat{a}^\dagger\hat{a}(\hat{b} + \hat{b}^\dagger) + \dots \quad (2.72)$$

where Δ_c is the laser detuning.

Using the same linearized approach as previously

$$\hat{a} = \bar{a} + \delta\hat{a} \quad (2.73)$$

we get interaction Hamiltonian as

$$\hat{H}_{int} = -\hbar g_0(\bar{a} + \delta\hat{a})^\dagger(\bar{a} + \delta\hat{a})(\hat{b} + \hat{b}^\dagger) \quad (2.74)$$

Simplifying equation 2.74, where the first term $-\hbar g_0|\bar{a}|^2(\hat{b} + \hat{b}^\dagger)$ is the average radiation pressure force equivalent to $\bar{F} = \hbar G|\hbar a|^2$ which can be omitted as a shift in the resonator displacement $\delta\bar{x} = \bar{F}/m_{eff}\omega_m^2$.

The second term from equation 2.74 gives the interaction Hamiltonian:

$$-\hbar g_0(\bar{a}^*\delta\hat{a} + \bar{a}\delta\hat{a}^\dagger)(\hat{b} + \hat{b}^\dagger) \quad (2.75)$$

and the third term from equation 2.74 $-\hbar g_0\delta\hat{a}^\dagger\delta\hat{a}$ is omitted as being typically too small in comparison to $|\bar{a}|$.

Using $\bar{a} = \sqrt{\bar{n}_c}$ where \bar{n}_c is the average number of the circulating photons in the cavity, the Hamiltonian in equation 2.74 simplifies to:

$$\hat{H} \approx \hbar\Delta_c\delta\hat{a}^\dagger\delta\hat{a} + \hbar\omega_m\hat{b}^\dagger\hat{b} + \hat{H}_{lin} + \dots \quad (2.76)$$

where the linearized interaction part is given as

$$\hat{H}_{lin} = -\hbar g_0\sqrt{\bar{n}_c}(\delta\hat{a}^\dagger + \delta\hat{a})(\hat{b} + \hat{b}^\dagger) \quad (2.77)$$

It can be seen that the effective optomechanical coupling strength

$$g_{lin} = g_0\sqrt{\bar{n}_c} \quad (2.78)$$

is enhanced by a factor of $\sqrt{\bar{n}_c}$.

In the resolved side band regime ($\kappa \ll \omega_m$) and depending on the cavity detuning there can be different interesting regimes for the optomechanical interaction.

For $\Delta_c = \omega_m$, the mechanical and optical resonators are approximated as harmonic oscillators that can resonantly exchange energy. And within the rotating wave approximation (RWA), the interaction Hamiltonian reduces to

$$-\hbar g(\delta\hat{a}^\dagger\hat{b} + \delta\hat{a}\hat{b}^\dagger) \quad (2.79)$$

Also known as the beam-splitter Hamiltonian in quantum optics: this is the regime of optimal cooling of the mechanical resonator.

When $\Delta_c \approx -\omega_m$, the interaction Hamiltonian within RWA becomes

$$-\hbar g(\delta\hat{a}^\dagger\hat{b}^\dagger + \delta\hat{a}\hat{b}) \quad (2.80)$$

which is known as the two mode squeezing interaction and is the regime of parametric amplification or heating where there is exponential growth in the energies of the mechanical and optical mode's. For the mechanical mode the growth of energy results in anti-damping or heating.

In conclusion in this section, we have dicussed the optomechanical effects of a Fabry Perot cavity with a movable end mirror using classical equations and quantum approach. In the next section we are going to discuss the optomechanics of membrane-in-the-middle setup.

2.3 Fabry Perot cavity with Membrane-in-the-middle approach

A Fabry Perot cavity with membrane in the middle is shown in figure 2.8. The end mirrors of the cavity are assumed to be highly reflective ($|r| \rightarrow 1$) and separated by L . The membrane is modelled as an infinitely thin 1D scatterer with polarizability ζ . We introduce the overall transfer matrix for the MIM setup using the TMM and use it to determine the optomechanical coupling strength g_0 .

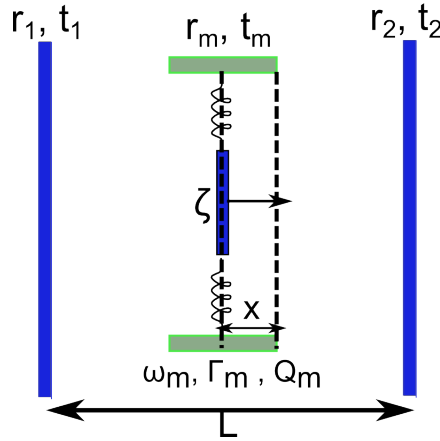


Figure 2.8: Scheme showing Fabry Perot cavity with a dielectric membrane in the middle (Membrane-in-the-middle setup)

For highly reflecting mirrors, the field should reproduce itself at the left and right cavity mirrors and this gives us the condition :

$$\begin{bmatrix} 1 \\ -1 \end{bmatrix} = \underbrace{\begin{bmatrix} e^{i\phi} & 0 \\ 0 & e^{-i\phi} \end{bmatrix}}_{M_{free\ space\ 1st\ half\ of\ cavity}} \underbrace{\begin{bmatrix} e^{1+i\zeta} & i\zeta \\ -i\zeta & 1-i\zeta \end{bmatrix}}_{M_{dielectric\ membrane}} \underbrace{\begin{bmatrix} e^{i\theta} & 0 \\ 0 & e^{-i\theta} \end{bmatrix}}_{M_{free\ space\ 2nd\ half\ of\ cavity}} \begin{bmatrix} 1 \\ -1 \end{bmatrix} \quad (2.81)$$

Solving and simplifying equation 2.81 gives us :

$$e^{ikL} = \frac{1}{1+i\zeta} [i\zeta \cos(2kx) \pm \sqrt{1 + \zeta^2 \sin^2(2kx)}] \quad (2.82)$$

by definition

$$g_0(x) = \frac{\partial \omega}{\partial x} x_{ZPM} = \frac{\partial k}{\partial x} (cx_{ZPM}) \quad (2.83)$$

Differentiating equation 2.82 as $(x \rightarrow x + \delta x, k \rightarrow k + \delta k)$

$$(1+i\zeta)e^{ikx}(1+i\delta kL) = i\zeta \cos[2(k+\delta k)(x+\delta x)] \pm \sqrt{1 + \zeta^2 \sin^2(x+\delta x)(k+\delta k)} \quad (2.84)$$

Simplifying equation 2.84 we get

$$\frac{\delta k}{\delta x} = \mp \frac{\frac{2k}{L}\zeta \sin(2kx)}{\sqrt{1 + \zeta^2 \sin^2(2kx) \pm \frac{2x}{L}\zeta \sin(2kx)}} \quad (2.85)$$

where equation 2.85 gives the single optomechanical coupling strength as

$$g_0(x) = \mp \frac{2\omega x_{ZPM}}{L} \frac{\zeta \sin(2kx)}{\sqrt{1 + \zeta^2 \sin^2(2kx) \pm \frac{2x}{L}\zeta \sin(2kx)}} \quad (2.86)$$

and in the case of symmetric placing $(2kx = \pi/2)$ equation 2.86 reduces to

$$g_0(x) \approx \frac{2\omega x_{ZPM}}{L} \frac{\zeta}{\sqrt{1 + \zeta^2 \pm \frac{2x\zeta}{L}}} \quad (2.87)$$

for a long cavity and a membrane approximately in the middle $(x \ll L)$

$$g_0(x) \approx g_0 \frac{\zeta \sin(2kx)}{\sqrt{1 + \zeta^2 \sin^2(2kx)}} \approx g_0 \frac{\zeta}{\sqrt{1 + \zeta^2}} \approx g_0 |r_m| \quad (2.88)$$

where $g_0 = \frac{2\omega x_{ZPM}}{L}$ is the optomechanical coupling strength for a perfectly reflecting membrane. We see that the effective optomechanical coupling strength is directly proportional to the reflectivity of the membrane $|r_m|$.

This shows that there is an interest in increasing the membrane reflectivity, i.e., to move from a membrane-in-the-middle to a mirror-in-the-middle system, which is the driving motivation for the discussion in chapter 4 [41].

Another approach to enhance the optomechanical interaction is to move from the single MIM to multiple MIM, as will be discussed in the next section.

2.4 Fabry Perot with periodic arrays of reflectors

In this section, we study the effects of having multiple mechanical elements forming a periodic array inside a large Fabry Perot cavity. It has been suggested that the collective motion of a periodic array of flexible elements modelled as scatterers can couple strongly to optical cavity fields under certain conditions. [34]

Consider an array of N identical reflectors (or dielectric membranes) shown in figure 2.9, assumed to be thin with respect to the wavelength of the incident light. Each reflector is treated as a lossless scatterer that is assumed to interact linearly with the electromagnetic field and is parametrized by its polarizability ζ . The spacing between the reflectors in the array is assumed to be d .

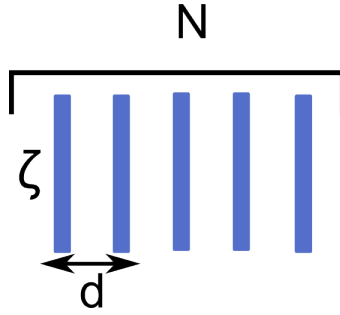


Figure 2.9: Scheme showing an array of N identical reflectors with inter-element separation d and individual element polarizability ζ

The optical properties of the array is determined by the number of elements N , the polarizability of each element ζ and the spacing between the elements d . For simplicity we consider lossless scatterers with real ζ . The transfer matrix for each element is given by:

$$M_m(\zeta) \equiv \begin{bmatrix} 1 + i\zeta & i\zeta \\ -i\zeta & 1 - i\zeta \end{bmatrix} \quad (2.89)$$

The free space propagation matrix between array elements for an incident monochromatic beam of wavelength $\lambda = \frac{2\pi}{k}$ over a separation distance d is given by

$$M_p(d) \equiv \begin{bmatrix} e^{ikd} & 0 \\ 0 & e^{-ikd} \end{bmatrix} \quad (2.90)$$

Then the transfer matrix of the array can be written as

$$M_{tot} = M_m(\zeta)M_p(d)M_m(\zeta)\dots M_m(\zeta) \quad (2.91)$$

where $M_m(\zeta)$ is repeated N times for N -elements.

Define a matrix M as

$$M_p(d/2)M_m(\zeta)M_p(d)\dots M_m(\zeta)M_p(d/2) = [M_p(d/2)M_m(\zeta)M_p(d/2)]^N \equiv M^N \quad (2.92)$$

which gives

$$M \equiv \begin{bmatrix} (1 + i\zeta)e^{ikd} & i\zeta \\ -i\zeta & (1 - i\zeta)e^{-ikd} \end{bmatrix} \quad (2.93)$$

M has unit determinant and, for real ζ , can be put under the form

$$M^N = \begin{bmatrix} (1 + i\chi)e^{ikd} + \mu & i\chi \\ -i\chi & (1 - i\chi)e^{-ikd} + \mu \end{bmatrix} \quad (2.94)$$

where $\chi \equiv \zeta U_{N-1}(a)$ and $U_n(x)$ is the n th Chebyshev polynomial of the second kind, $a = \cos(kd) - \zeta \sin(kd)$ and

$$e^{i\mu} = \frac{1 - i\zeta U_{N-1}(a)}{(1 - i\zeta)U_{N-1}(a) - e^{ikd}U_{N-2}(a)} \quad (2.95)$$

The matrix M^N has a padding corresponding to free space propagation over $d/2$ on either side which we remove to get the transfer matrix of the N -element array :

$$M_N \equiv M_p[\mu/(2k)]M_m\chi M_p[\mu/(2k)] \quad (2.96)$$

M_N is a single matrix representing the N -element array matrix as one single collective superelement with effective polarizability χ and a padding equivalent to a phase shift of $\mu/2$ on either side of the array.

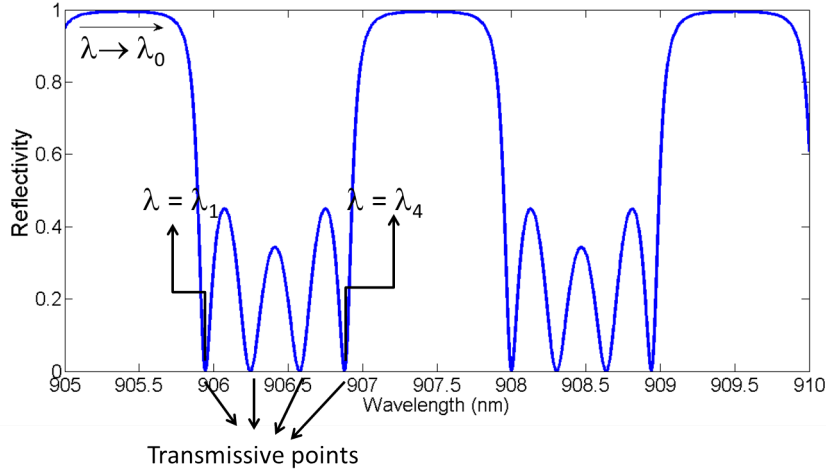


Figure 2.10: Modelled reflectivity spectrum for an array of 5 Si_3N_4 membranes with a separation distance $d = 200 \mu\text{m}$ and refractive index of $n = 1.98$, showing the reflective regime and $(N-1 = 4)$ transmissive points.

Since we know the transfer matrix of the N -array element 2.96 we obtain the reflectivity of the N -array of elements $\left(R = \left| \frac{M_N(1,2)}{M_N(2,2)} \right|^2 \right)$.

Figure 2.10 shows as an example the reflectivity as a function of wavelength of an array of 5 Si_3N_4 membranes with a separation distance of $200 \mu\text{m}$, membrane thickness of 100 nm and a refractive index of $n = 1.98$.

From figure 2.11, we observe two distinct operating regimes : A reflective regime when the reflectivity of the ensemble of 5-element array has a high reflectivity ($\approx 99\%$), and a transmissive regime, around the $(N-1)$ transmissive points where the reflectivity goes to zero ($\lambda_{1,2,3,4}$).

The N -element array is then placed in a Fabry Perot cavity to imitate the MIM setup as shown in figure 2.11.

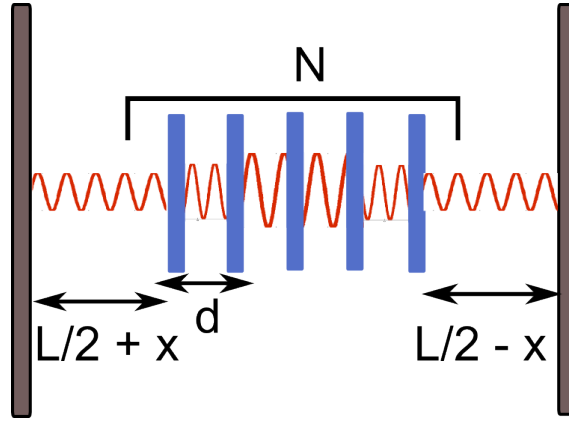


Figure 2.11: Scheme showing an array of N identical reflectors with inter-element separation d and individual element polarizability ζ placed in the middle of a Fabry Perot cavity.

The Fabry Perot cavity has a length L which is assumed much longer than the array ($L \gg Nd$). The transfer matrix for the system is then given by :

$$M_c = M_m(Z)M_p(L/2 + x)M_N M_p(L/2 - x)M_m(Z) \quad (2.97)$$

where x is the displacement of the ensemble with respect to the center of the cavity and Z is the polarizability of the cavity mirrors which is assumed equal for both.

The transmission of the system is given by

$$T_c = \left| \frac{1}{(M_c)_{22}} \right|^2 \quad (2.98)$$

The interaction of the array with the cavity field will shift the resonances of the main cavity. The maxima of T_c will give the new resonances which can be computed numerically using TMM. Analytically, we can find the resonances for perfectly reflecting cavity mirrors ($Z \rightarrow \infty$) by solving

$$\begin{bmatrix} 1 \\ -1 \end{bmatrix} = \underbrace{\begin{bmatrix} e^{i\phi} & 0 \\ 0 & e^{-i\phi} \end{bmatrix}}_{M_{\text{free space 1st half of cavity}}} \underbrace{\begin{bmatrix} e^{1+i\chi} & i\chi \\ -i\chi & 1 - i\chi \end{bmatrix}}_{M_{\text{dielectric membrane}}} \underbrace{\begin{bmatrix} e^{i\theta} & 0 \\ 0 & e^{-i\theta} \end{bmatrix}}_{M_{\text{free space 2nd half of cavity}}} \begin{bmatrix} 1 \\ -1 \end{bmatrix} \quad (2.99)$$

where $\phi \equiv k(L/2 + x) + \mu/2$ and $\theta \equiv k(L/2 - x) + \mu/2$ and we get

$$e^{ikL} = \frac{e^{-i\mu}}{1 + i\chi} [i\chi \cos(2kx) \pm \sqrt{1 + \chi^2 \sin^2(2kx)}] \quad (2.100)$$

We consider the optomechanics of the ensemble of N -elements with center of mass (COM) coupling. To know the shift in the cavity resonance frequency as the COM of the ensemble changes or the separation distance between the elements shifts, we expand equation 2.100 in small increments ($k \rightarrow k + \delta k$, $x \rightarrow x + \delta x$, $\chi \rightarrow \chi + \delta \chi$, $\mu \rightarrow \mu + \delta \mu$). For the case of uniform displacement, $\partial \mu = \partial \chi = 0$ and $|L/x|$ is very large

$$L\delta k = \mp [2\chi \sin(2kx) / \sqrt{1 + \chi^2 \sin^2(2kx)}] k \delta x \quad (2.101)$$

Equation 2.101 is maximum when $\sin(2kx) = \mp 1$ which gives

$$L\delta k = 2k(-\chi / \sqrt{1 + \chi^2}) \delta x \quad (2.102)$$

The optomechanical coupling derived from equation 2.102 increases monotonically with $|\chi|$ and is maximum when χ is maximum $\chi_0 \equiv \zeta U_{N-1}(\sqrt{1 + \zeta^2}) = -i \sin[N \cos^{-1}(\sqrt{1 + \zeta^2})]$. This happens when $kd = kd_0 \equiv -\tan^{-1}(\zeta)$. The optomechanical coupling strength is then given by

$$g_{COM} = g \sqrt{\mathcal{R}/N} \quad (2.103)$$

where $\mathcal{R} = \chi_0^2 / (1 + \chi_0^2)$ and $g = \frac{2\omega_c x_{zpt}}{L}$.

From equation 2.103 we see that g_{COM} can be increased by increasing the effective reflectivity, but will ultimately decrease due to the increase in the effective mass of the mode, which is multiplied by N .

In any case, g_{COM} is bounded by g .

For a transmissive point λ_l shown in figure 2.10 the reflectivity of the ensemble goes to 0 at certain transmissive points given by

$$\lambda_l \equiv \frac{2\pi d}{\cos^{-1}[\cos(l\pi/N) / \sqrt{1 + \zeta^2}] - \tan^{-1}(\zeta)} \quad (2.104)$$

To obtain the optomechanical coupling strength we use one transmissive point, let's say λ_1 and apply the same procedure as defined above and in section 2.8 which is further detailed thoroughly in ???. With this analysis, the aim is determine the shift in the cavity resonance frequency when one of the elements, let's say the j th gets displaced by a certain amount δx_j . The transfer matrix for the ensemble then becomes the matrix associated with elements to the left of the j th element, the j th element, and the elements to the right of the j th element. The result being that the individual linear optomechanical coupling for a given l th transmissive point has a sinusoidal dependence with respect to the position in the array

$$g_j^{(l)} \propto \sin\left(2l\pi \frac{j - 1/2}{N}\right) \quad (2.105)$$

and the coupling of the collective motion of all the elements to the cavity field close to the l th transmission is given by

$$g_{sin}^{(l)} \equiv \sqrt{\sum_{j=1}^N (g_j^{(l)})^2} \quad (2.106)$$

As detailed in reference [37] the coupling of the collective motion of dielectric membranes to the cavity field close to the l th transmission point is governed by the constant $g_{sin}^{(l)}$. For $l = 1$ and $\zeta < 0$, we get

$$g_j^{(1)} = -2\omega_c x_0 \frac{\zeta \csc(\pi/N) [\sqrt{\sin^2(\pi/N) + \zeta^2} - \zeta]}{L - 2Nd\zeta \csc^2(\pi/N) \sqrt{\sin^2(\pi/N) + \zeta^2}} \sin(2\pi \frac{j-1/2}{N}) \quad (2.107)$$

for $N = 2$ equation 2.107 becomes

$$g_{sin}^{(1)} = -g \frac{\sqrt{2}\zeta(\sqrt{1+\zeta^2} - \zeta)}{1 - 4\frac{d}{L}\sqrt{1+\zeta^2}} \quad (2.108)$$

and for $N > 2$ equation 2.107 gives

$$g_{sin}^{(1)} = -g \sqrt{\frac{N}{2}} \frac{\zeta \csc(\pi/N) [\sqrt{\sin^2(\pi/N) + \zeta^2} - \zeta]}{1 - 2N\frac{d}{L}\zeta \csc^2(\pi/N) \sqrt{\sin^2(\pi/N) + \zeta^2}} \quad (2.109)$$

The collective optomechanical coupling strength $g_{sin}^{(l)}$ is no longer bounded by g . For large N and $|\zeta|$ and small d/L , equation 2.109 gives

$$g_{sin}^{(1)} \approx \frac{\sqrt{2}}{\pi} g \zeta^2 N^{3/2} \quad (2.110)$$

Equation 2.110 shows that the collective optomechanical coupling strength scales with ζ^2 and $N^{3/2}$. This is because as N increases the fraction of energy density per photon inside the array increases strongly and this effect increases the optomechanical coupling strength. And for $|\zeta| > 1$, the cavity field mode is strongly concentrated between the highly reflective elements and this concentration grows with element reflectivity and gives the quadratic scaling of $g_{sin}^{(1)}$ with ζ .

Operating in the transmissive regime thus offers various interesting possibilities: (i) for enhancing the optomechanical coupling strength beyond that achievable with a single element, and potentially for reaching the single photon strong coupling regime of optomechanics [34], (ii) for engineering long-range interactions between the membranes which are determined by the structural properties of the array and thus tunable by the choice of the optical fields[35].

In the next chapter we detail the first steps towards the experimental realization of membrane array systems to be used in the experiments of transmissive optomechanics.

Chapter 3

Silicon nitride membrane arrays

This chapter reports on the first steps towards the realization of silicon nitride membrane arrays. As previously discussed in chapter 2, the membrane arrays will be used to study collective optomechanical effects in future experiments [34][37]. Section 3.1 gives a general introduction to Si_3N_4 membranes and details the different membranes we have used in our studies. In section 3.2 we discuss single Si_3N_4 membrane and chip characterization. This section details how Profilometer and Atomic Force Microscopy (AFM) measurements are used to determine the inter-membrane spacing and how we use ellipsometric measurements to get an estimate of the individual membrane's thickness and refractive index. In section 3.3, we discuss the assembly of double membrane arrays and in section 3.4 we present results on the characterization of the optical properties of various membrane arrays using white light and monochromatic light transmission measurements. The results of these measurements are compared with the theoretical expectations and further discussed. The chapter ends with section 3.5, where the effect of non-parallelism on the transmission of plane mirror Fabry Perot resonators is theoretically discussed.

3.1 Single Si_3N_4 membrane

High stress Si_3N_4 membranes due to their low mass ($m \approx ng$) and high mechanical quality factor ($Q_m = 10^6 - 10^7$) for megahertz frequencies [42] have attracted attention as efficient mechanical resonators. Also, Si_3N_4 membranes have very low absorption coefficients, which means that they can be incorporated into high finesse optical cavities without increasing the absorption losses significantly. The combination of these two factors makes Si_3N_4 membranes ideal candidates for cavity optomechanical experiments. The Si_3N_4 membranes were first introduced in the middle of a Fabry- Perot cavity for optomechanical experiments by Harris group at Yale [39]. Since then many research groups around the world are now using these membranes for variety of optomechanical experiments [10, 17, 18, 22-30] .

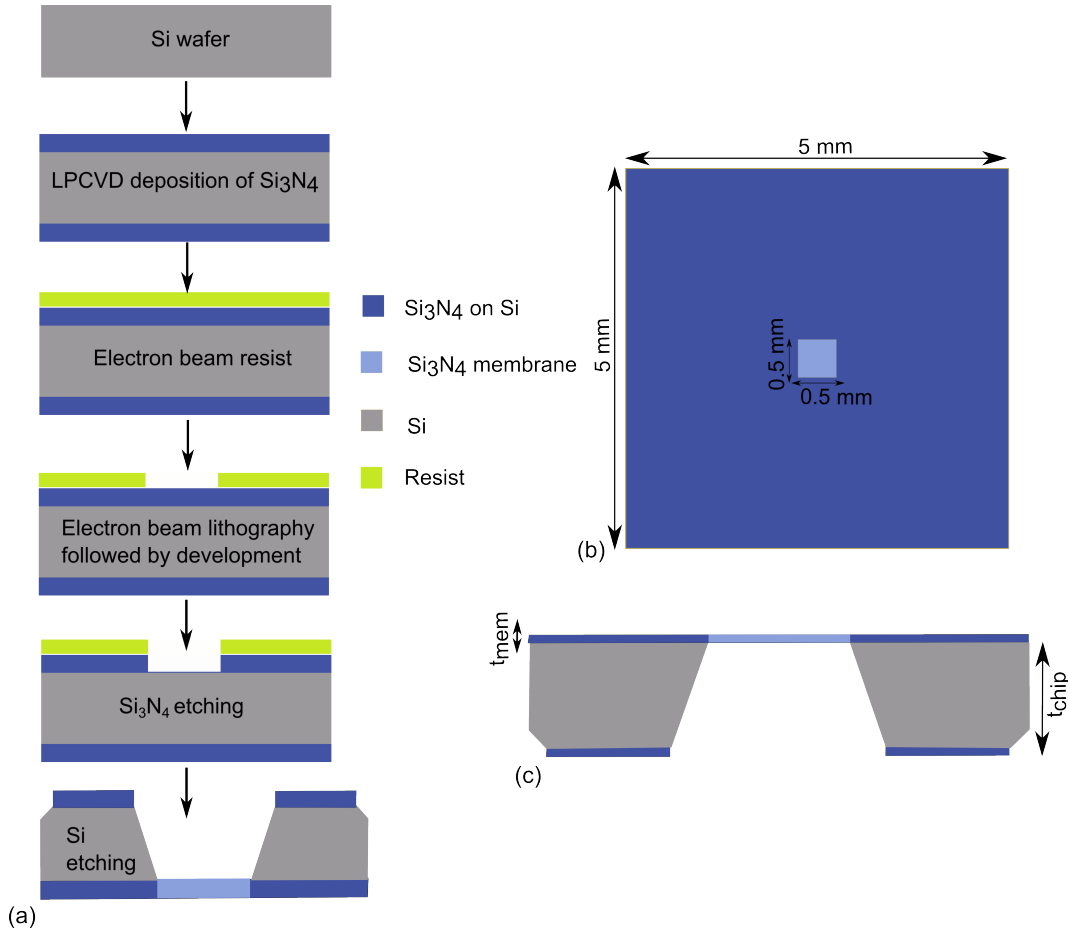


Figure 3.1: Fabrication process for single Si₃N₄ membranes is shown in (a). The membrane dimensions are shown in (b) top view and (c) shows a cross sectional view

The Si₃N₄ membranes used in this thesis are bought from a MEMS company, NORCADA, Edmonton (Canada). NORCADA delivers membranes in a range of different chip sizes, membrane sizes and thicknesses (<http://www.norcada.com/>). The Si₃N₄ membranes bought from NORCADA are fabricated using a Low Pressure Chemical Vapour Deposition Technique (LPCVD). As shown in figure 3.1(a), the fabrication starts with LPCVD deposition of Si₃N₄ layer on a Si wafer, followed by deposition of electron beam resist and electron beam lithography (EBL) to define the membrane window, and further development and etching to create the suspended Si₃N₄ membrane [43]. The Si₃N₄ membrane acquires tensile stress due to thermal expansion mismatch between Si and Si₃N₄ layer. Depending on the fabrication parameters such as composition of Silicon and Nitride, temperature of deposition etc, Si₃N₄ membranes can possess either low stress in the range of few 100's MPa or high stress (stoichiometric membranes) which can be as high as 1 GPa.

A typical picture of single Si₃N₄ membrane is shown in figure 3.2a. The Si₃N₄ membrane

acts as a mechanical resonator with square drum modes of vibration, shown in figure 3.2b. The vibration frequencies for the drum modes of a square membrane under tension are,

$$\nu_{ij} = \frac{1}{2L} \sqrt{\frac{\sigma}{\rho}} \sqrt{i^2 + j^2} \quad (3.1)$$

for the (i, j) th mode where σ is the tensile stress, ρ is the mass density and L is the lateral dimension of the membrane. For a high stress stoichiometric Si_3N_4 square membrane with $L = 500 \mu\text{m}$, $\sigma = 0.9 \text{ GPa}$ and $\rho = 2.7 \times 10^3 \text{ kg/m}^3$ the frequency of the fundamental eigenmode $(1, 1)$ is $\nu_{11} \approx 800 \text{ kHz}$.

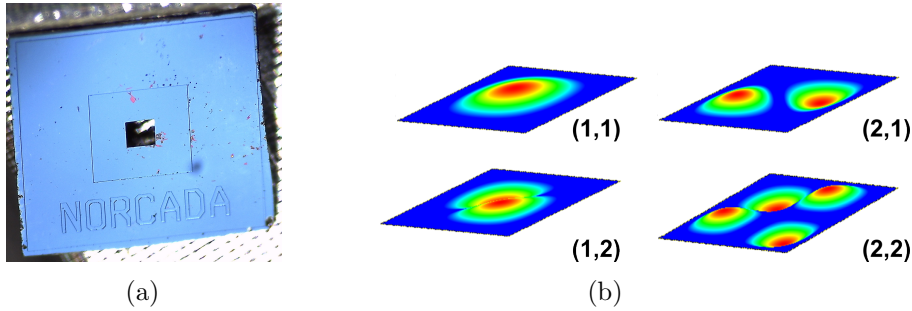


Figure 3.2: Norcada single membrane with $5 \times 5 \text{ mm}^2$ Si frame, $500 \times 500 \mu\text{m}^2$ membrane window and 100 nm membrane thickness is shown in (a) and a color coded plot of the amplitude of mechanical modes of vibration $(1,1)$, $(1,2)$, $(2,1)$ and $(2,2)$ is shown in (b).

Figure 3.1(b) shows a schematic of the topview of a single membrane and 3.1(c) gives the cross sectional view. For all the membranes used in this chapter, the lateral dimension of the chip size is $5 \times 5 \text{ mm}^2$ of the Si_3N_4 chip, the membrane window size is $500 \times 500 \mu\text{m}^2$ and the thickness is 100 nm .

Identification	Properties	t_{chip}	t	d
A Chip	No spacer	$500 \mu\text{m}$	100 nm	
B Chip	Spacer	$500 \mu\text{m}$	100 nm	$9 \mu\text{m}$
$100 \mu\text{m}$ notched chip	Si substrate as spacer	$100 \mu\text{m}$	100 nm	$100 \mu\text{m}$
$200 \mu\text{m}$ notched chip	Si substrate as spacer	$200 \mu\text{m}$	100 nm	$200 \mu\text{m}$

Table 1: Summary of Si_3N_4 membrane's

Table 1 gives a summary of the various single membranes used in this chapter to make membrane arrays where t_{chip} is thickness of the Si chip, t is the Si_3N_4 membrane thickness and d is the thickness of the spacer which defines the distance between two membranes.

Chip A and chip B form a series of specially designed membranes to be used together to create a double array with membrane separation to be $\approx 9 \mu\text{m}$. As an illustration, we show in figure 3.3 how we stack the chip A and chip B, which has a $\approx 9 \mu\text{m}$ thick custom spacer

deposited on the Si_3N_4 film on the Si frame region to form the $9\ \mu\text{m}$ double membrane array.

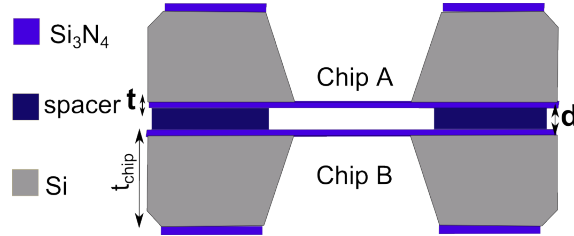


Figure 3.3: Chip A and custom designed chip B forming $9\ \mu\text{m}$ spaced double membrane array.

Using the Si chip frame as a spacer allows for realizing arrays with more than two membranes, at the expense of an increased inter-membrane separation. While NORCADA can achieve Si chip thicknesses down to $\approx 50\ \mu\text{m}$, we use chip thicknesses of either $100\ \mu\text{m}$ or $200\ \mu\text{m}$ in these first experiments.

3.2 Single Si_3N_4 membrane characterization

Bearing in mind the previous array geometries and to assess the homogeneity of the samples we now characterize the membranes from the different batches in terms of optical properties (thickness, refractive index) and in terms of the chip geometry (spacer thickness, planarity).

Single Si_3N_4 membranes are thus characterized using Profilometer, AFM and Ellipsometry techniques. Profilometer and AFM measurements are used to characterize the spacer thickness and roughness of B chip's and the Si frame of the notched membranes. Using ellipsometric measurements on the Si_3N_4 film on Si surrounding the membranes, we give an estimate of the membrane thickness and refractive index. These measurements were performed in the cleanroom of the iNano center at Aarhus University.

3.2.1 Profilometer spacer measurement

A profilometer is an instrument used to measure surface variations. The contact profilometer used in this work is shown in figure 3.4. It consists of a translation stage where the sample is placed and a stylus tip which moves across the sample surface. To perform a sample scan, the sample is positioned below the stylus tip, then the range of scan defined and the tip engaged to start the measurement process. The diamond tip which was set at a certain vertical point now moves along the surface and measures the force exerted by the surface on the tip. The set vertical point defines a fixed torque for the system and, as the force on the tip changes, this is recorded as a change in the set torque. The scanning process is controlled via active force feedback loop and the surface profile generated gives a direct measure of the sample surface. Profilometer gives robust, sensitive and high resolution measurements and are ideally

suited for hard solid surfaces. The resolution of a profilometer measurement depends on the scan length, the duration of scan and the sampling rate which depends on the specific profilometer used. To measure a step height of $\approx 9 \mu\text{m}$ we have a resolution of $\approx 0.2 \mu\text{m}$ and for $100 \mu\text{m}$ and $200 \mu\text{m}$ notched membranes the resolution is $\approx 1.2 \mu\text{m}$.



Figure 3.4: Bruker DektakXT profilometer with the inset showing the diamond tip mounted on a translation stage.

Profilometer measurements are first performed on the B chip with the custom made spacer and the results are compared with AFM studies in section 3.2.2.

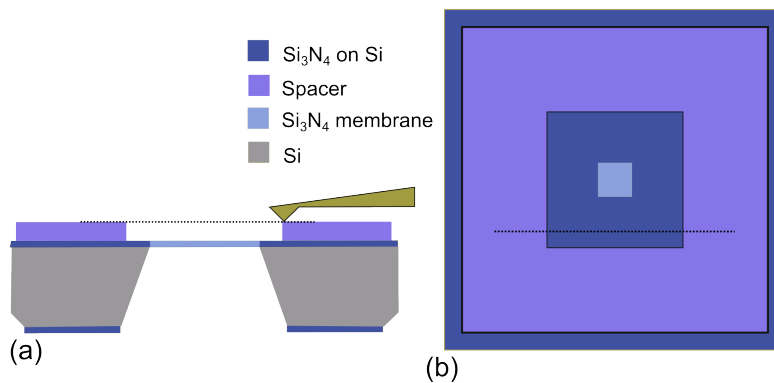


Figure 3.5: (a) shows a cross sectional view of the scanning tip on chip B and (b) shows a top view of a typical scan.

Figure 3.5 shows a scheme where the tip is scanned along a line parallel to the chip side on the spacer surface. The same line scanning process is repeated over several edges to estimate spacer thickness variations and to estimate possible wedge at one or the other edges. Figure 3.6 shows the various line scans made on a B chip, the evaluation of which will be further discussed.

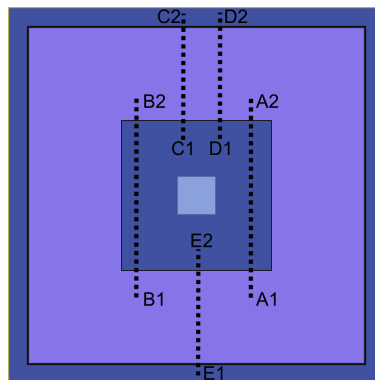


Figure 3.6: Various line scans used for spacer thickness determination on chip B. For example, A1A2 is a scan line with two step edges one at A1 and the other at A2.

Figure 3.7 shows the result of a typical line scan measurement as given in Figure 3.6. The vertical axis shows the step profile of the spacer in units of μm and the horizontal axis shows the lateral distance moved by the stylus tip in units of μm . The bottom level is the membrane surface on Si substrate and the top level is the spacer surface for line scans.

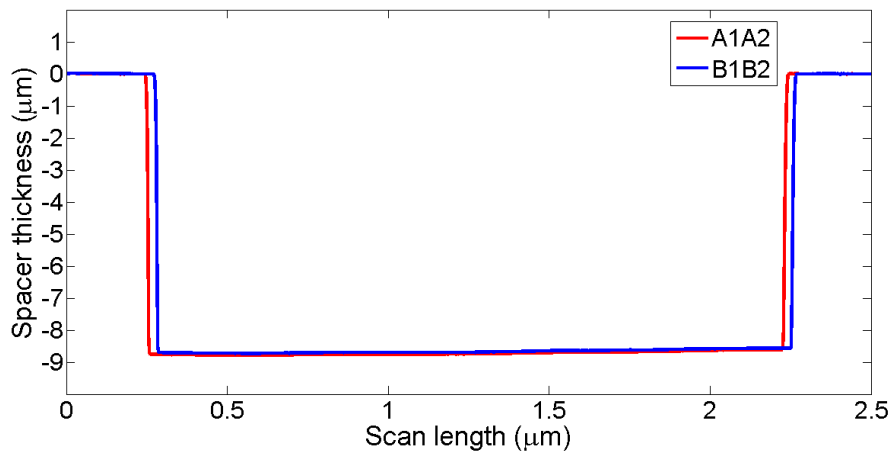


Figure 3.7: Result of an typical profilometer scan on chip B.

From figure 3.7 it can be seen that the spacer thickness does not deviate much on a μm scale ($\approx 50 \text{ nm}$) indicating flat, smooth, non-wedged structure. This is a critical observation since the optical properties of the double membrane array are crucially dependent on the parallelism of the membranes as will be discussed in section 5.8.

For finding the average spacer thickness at each step point, we take the average of data points for the top level and subtract it by the average of data points for the bottom level. For example, for the scan shown in 3.7, there are two step points. For the first step point marked as A1 in figure 3.6, we take the average of all spacer thickness data points in the scan length range of $\approx 0 - 0.25 \mu\text{m}$ and subtract this with the average of spacer

thickness data points in the range of $\approx 0.30 - 2.20 \mu\text{m}$. This gives us an estimate of the average spacer thickness at one step point, then we repeat the procedure for all other step positions.

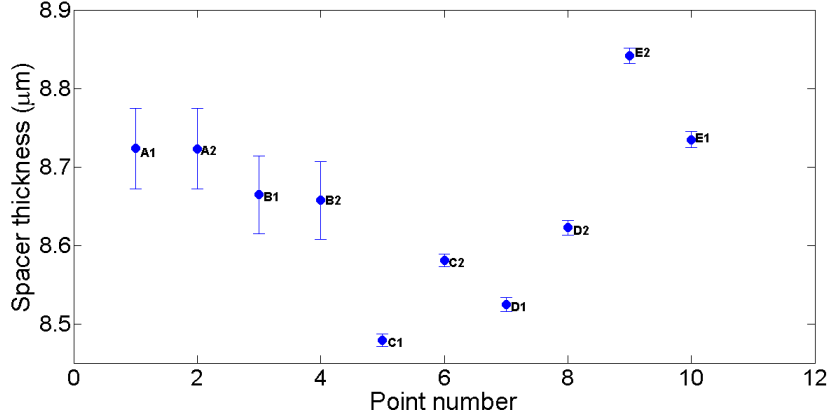


Figure 3.8: Point-by-point height variation graph for line scans shown in figure 3.6.

Figure 3.8 shows the height measured at each step point on a line scan of the same membrane chip with reference to figure 3.7. The results are summarized in table 2. From figure 3.8 we can clearly see that there is a some variation, of the order of $\approx 0.4 \mu\text{m}$, between the highest and lowest point in height, but there is no clear trend to be observed in the spacer thickness variation. This seems to indicate that there is no gradual or systematic variation of the spacer thickness for this chip.

Scanning Line	Point Number	Height (μm)
A1	1	8.72 ± 0.05
A2	2	8.72 ± 0.05
B1	3	8.66 ± 0.05
B2	4	8.66 ± 0.05
C1	5	8.48 ± 0.01
C2	6	8.58 ± 0.01
D1	7	8.52 ± 0.01
D2	8	8.62 ± 0.01
E1	9	8.84 ± 0.01
E2	10	8.73 ± 0.01

Table 2: Summary of profilometer measurement results for a B chip.

An upper bound on the tilt of the spacer is calculated to be of the order of 0.1 mrad and the average spacer height is estimated to be $8.65 \pm 0.11 \mu\text{m}$.

The same measurement scheme is used to estimate the thickness of the Si substrate for the 100 and $200 \mu\text{m}$ notched chips, where the chip thickness now acts as the spacer distance. In conducting these measurements, one practical difficulty was to make scans over the chip surface without making the chip move with the tip. A simple yet effective

solution was found when the chip was taped onto a clean Si carrier wafer, with the Si wafer surface acting as the base level and the chip surface as the top level. As shown in figure 3.33(b), the reference level is the surface of a clean carrier Si wafer and the top level is the membrane upside surface. To check for any unevenness of the surface these measurements were repeated on the reverse side, i.e with the membrane side down, as well.

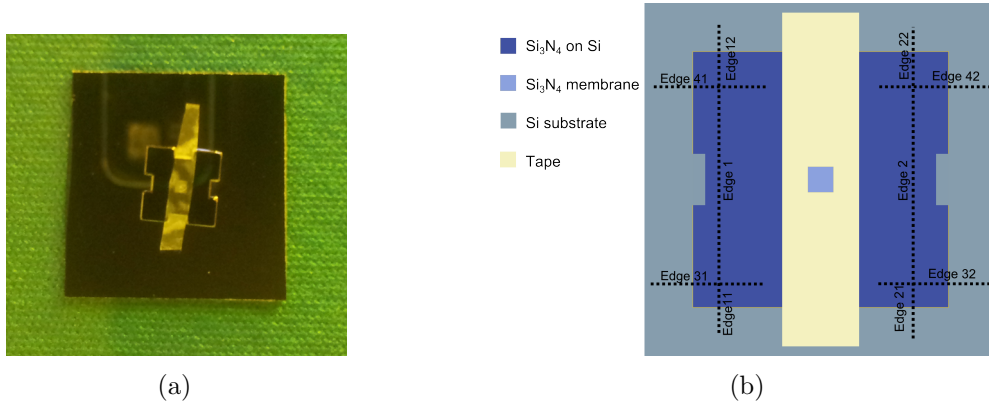


Figure 3.9: (a) shows a picture of the notched chip taped onto a Si carrier and (b) shows the scheme of various line scans made on this chip.

Figure 3.10 shows a couple of typical measurement scans for a 100 μm notched chip. The reference level is the surface of the Si carrier wafer and the top level is the surface of the Si_3N_4 membrane on the chip. A slight wedge at one of the edges, of the order of $\approx 2.9 \mu\text{m}$ can be observed.

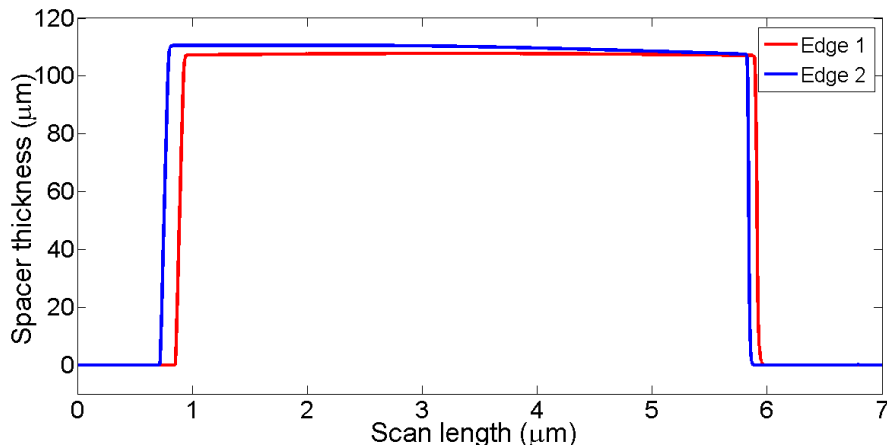


Figure 3.10: Result of a typical scan for 100 μm notched chip.

To map the thickness at various locations, the same measurement is performed on different edges of the same chip and the results are summarized in table 2. Figure 3.11 shows the thickness variation at each step point. The average height of the 100 μm spacer

is estimated to be $109.9 \mu\text{m} \pm 2.5 \mu\text{m}$ and an upper bound on the tilt is estimated to be 0.9 mrad.

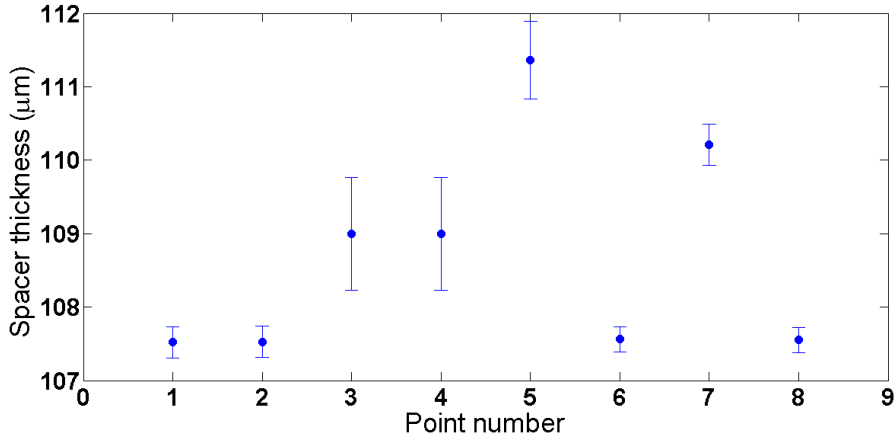


Figure 3.11: Spacer thickness at various positions for a $100 \mu\text{m}$ notched chip.

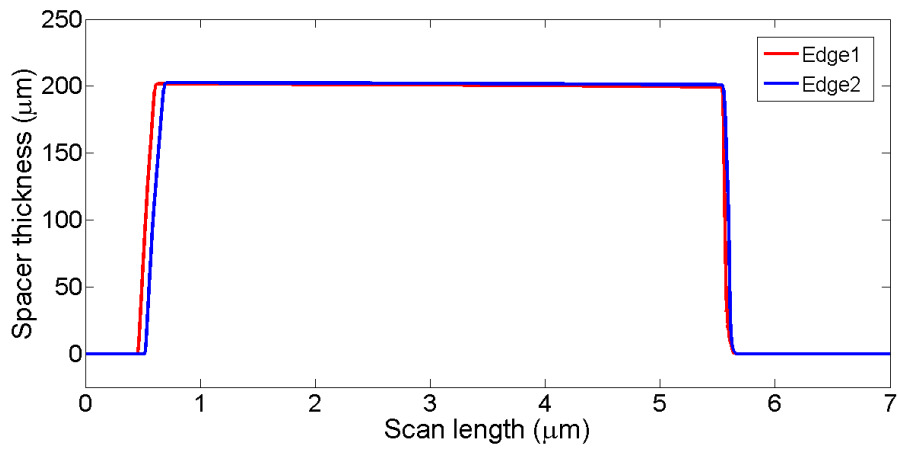
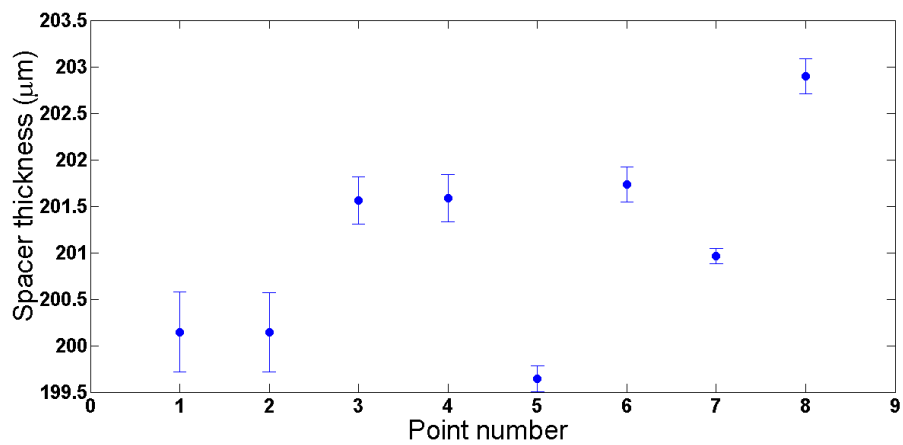
Scanning line	Point number	Height membrane side up (μm)	Height membrane side down (μm)
Edge 11	1	107.5 ± 0.2	111.6 ± 0.9
Edge 12	2	107.5 ± 0.2	111.6 ± 0.9
Edge 21	3	108.9 ± 0.8	108.5 ± 0.5
Edge 22	4	108.9 ± 0.8	108.5 ± 0.5
Edge 31	5	111.4 ± 0.5	109.6 ± 0.4
Edge 32	6	107.6 ± 0.2	115.6 ± 0.4
Edge 41	7	110.2 ± 0.3	108.1 ± 0.3
Edge 42	8	107.5 ± 0.2	114.3 ± 0.4

Table 2 : Summary of measured chip thickness of a $100 \mu\text{m}$ notched chip at various edge positions.

Similar measurements on a different $100 \mu\text{m}$ notched chip gave a chip thickness of $111.5 \mu\text{m} \pm 3.0 \mu\text{m}$. This result suggests that within the same batch we expect the thickness to be closer to the measured value of $\approx 110 \mu\text{m}$ than the expected chip thickness of $100 \mu\text{m}$. Profilometer measurements on more chips from a given batch could allow for sampling the Si chip thickness distribution in a batch.

Profilometer measurements for a notched $200 \mu\text{m}$ chip are performed and analyzed in the same way as discussed before. The results for the $200 \mu\text{m}$ notched chip are summarized below. Figure 3.12 shows typical scan results, 3.13 shows the variation in spacer thickness and table 3 tabulates the result.

The average thickness for this chip is found to be $201.1 \pm 0.8 \mu\text{m}$ with an estimated upper bound on the tilt of 0.5 mrad.

Figure 3.12: Result of typical scan for a 200 μm notched chip.Figure 3.13: Spacer thickness variation for 200 μm thick chip.

Scanning Line	Point Number	Height Membrane side up (μm)	Height Membrane side down (μm)
Edge 11	1	200.1 ± 0.4	201.5 ± 0.1
Edge 12	2	200.1 ± 0.4	201.5 ± 0.1
Edge 21	3	201.6 ± 0.3	200.5 ± 0.1
Edge 22	4	201.6 ± 0.2	200.5 ± 0.1
Edge 31	5	199.6 ± 0.1	201.6 ± 0.1
Edge 32	6	201.7 ± 0.2	200.5 ± 0.2
Edge 41	7	200.9 ± 0.1	202.1 ± 0.1
Edge 42	8	202.9 ± 0.2	200.9 ± 0.2

Table 3 : Summarizing measurement results for notched 200 μm Si chip thickness.

In conclusion, the profilometer measurements provide us with a rough estimate of the

spacer thickness of the various chips to be used to make membrane arrays. We obtained spacer thicknesses of $8.65 \pm 0.11 \mu\text{m}$, $109.9 \pm 2.5 \mu\text{m}$, $201.1 \pm 0.9 \mu\text{m}$ for $9 \mu\text{m}$ B chip, $100 \mu\text{m}$ notched chip and $200 \mu\text{m}$ notched chip, respectively.

These measurements somehow deviate with respect to the specifications provided by NORCADA which were $9.3 \pm 0.5 \mu\text{m}$ for B chip, $100 \pm 5 \mu\text{m}$ for $100 \mu\text{m}$ notched chip and $200 \pm 10 \mu\text{m}$ for $200 \mu\text{m}$ notched chip. This prompted us in using another method, Atomic Force Microscopy (AFM), for characterizing the spacer thickness, which will be discussed in the next section.

The profilometer measurements of spacer thickness at various positions also provide an upper bound on a possible wedge of the spacer (typically around 0.5 mrad), which is a relevant parameter when characterizing the optical properties of membrane arrays.

3.2.2 AFM spacer measurement

Atomic Force Microscopy (AFM), as its name suggests, is a microscopic imaging technique that maps atomic force interaction between a tip and a sample and produces surface scans. The AFM instrument used for analysis in this work is shown in figure 3.14. The main parts of this AFM are: a remote controlled XYZ translation stage, a Si cantilever mounted on an adjustable holder and a laser beam deflection system. The AFM is operated in a non-contact tapping mode, which means that the tip is not in contact with the sample surface but at a very close range, where it can sense the attractive force between the tip and the sample. These short range atomic forces cause a deflection of the tip which is then detected using a laser beam. As shown in figure 3.15, a laser beam is directed towards the back of the cantilever tip which is then reflected to quadrant photodetectors. As the tip is scanning across a sample surface, any change in height is then recorded as the change in the reflected light intensity by the photodetectors. The movement of the tip is controlled via an active feedback loop.

For us AFM acts as a high resolution measurement technique to measure spacer height and correlate the results obtained with profilometer on the same chip. We use standard RTE SP cantilever tip with a tip radius of 8 nm . Sharper tips allow for high resolution imaging since the tip can resolve adjacent features more accurately. The lower bound on the dimension of measurable features is limited by the tip of the cantilever. For us the applicability of AFM measurement was limited to the B chip, due to an upper bound on the measurable height by the AFM instrument, which is about $10 \mu\text{m}$.

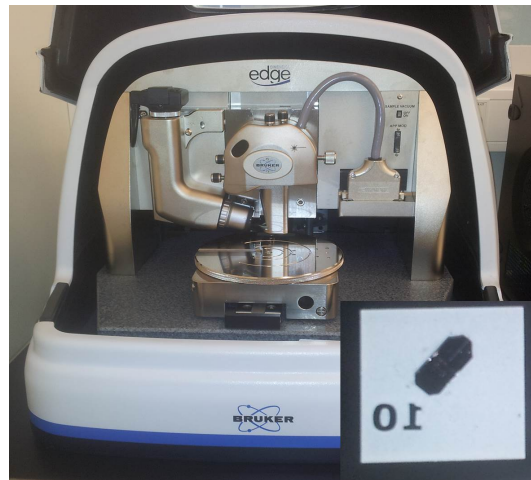


Figure 3.14: Picture of Bruker AFM (edgeDimension) used in this work with the inset showing the used cantilever tip.

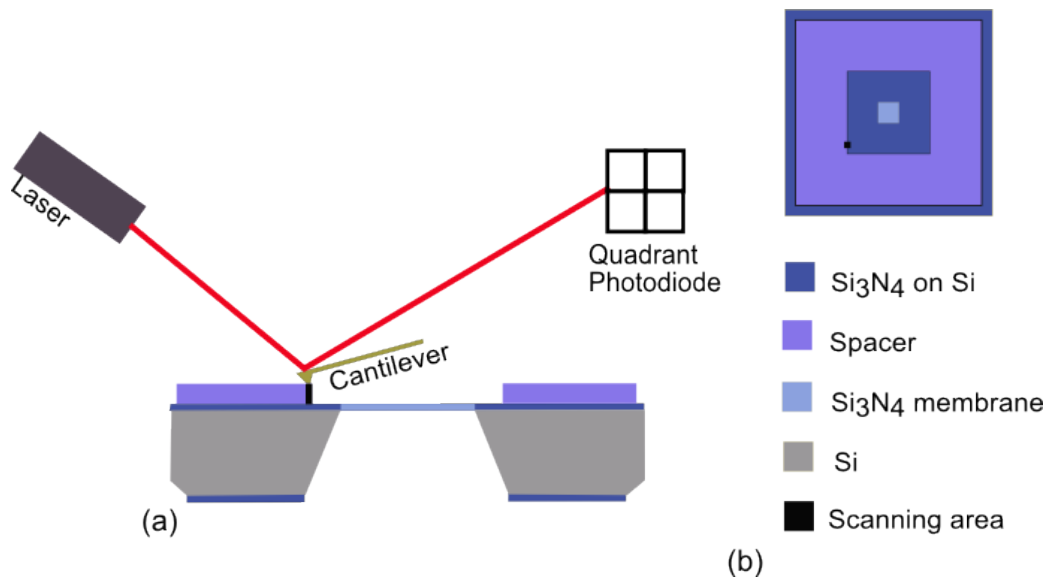


Figure 3.15: Principle of AFM scanning on a chip B (a) cross sectional view (b) top view.

Figure 3.16(a) shows a picture of the AFM tip scanning over the spacer of the B chip used previously in profilometer measurement. The scan is performed over an area of $50\ \mu\text{m} \times 50\ \mu\text{m}$ and the result of the measurement is shown in 3.16(b). The dark region represents the membrane surface reference level and the bright region is the spacer top level.

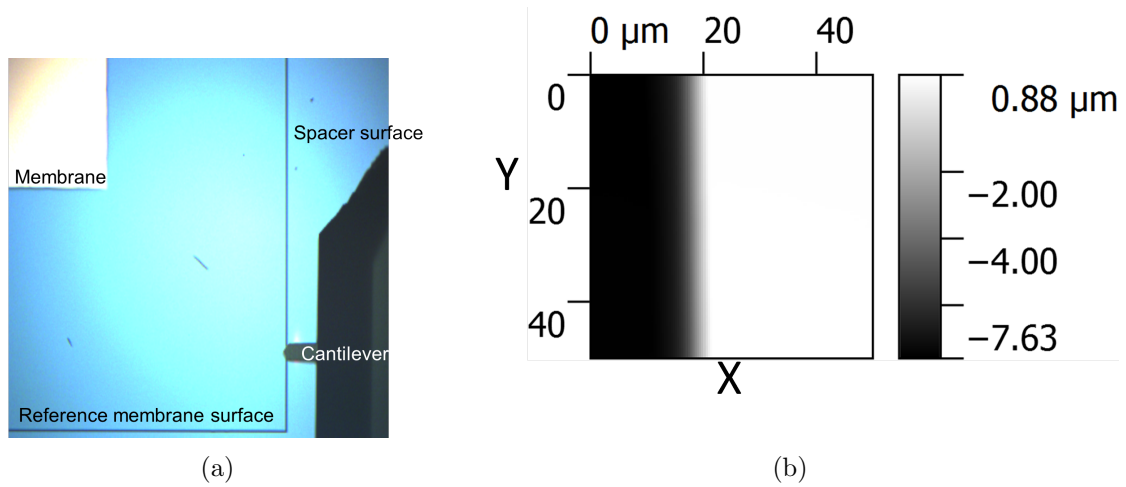


Figure 3.16: (a) shows a picture of the AFM tip scanning over the spacer of a B chip and (b) shows the result of the AFM scan measurement over the area of $50 \mu\text{m} \times 50 \mu\text{m}$ shown in (a).

Averaging the measured height along Y and plotting it versus X for the image shown in figure 3.16(b), we get height profile of the spacer shown in figure 3.17. The vertical axis shows the step profile in units of nm and the horizontal axis shows scan length in μm . The spacer height at this location is found to be $8.447 \mu\text{m} \pm 0.003 \mu\text{m}$.

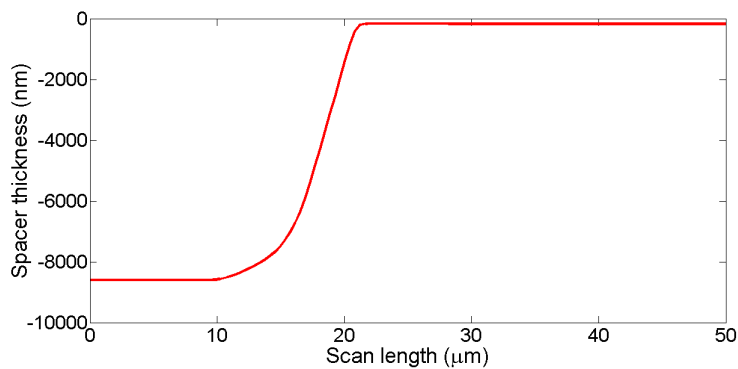


Figure 3.17: AFM measured spacer thickness at a given edge position for a B chip. This is obtained by averaging the measured height along Y axis shown in figure 3.16(b) and plotting it along X.

The scanning process shown in figure 3.16 is repeated at several spacer edge locations on the same chip, as shown in fig 3.18. The average spacer heights obtained at each of these locations is shown in figure 3.19 and summarized in the table 4.

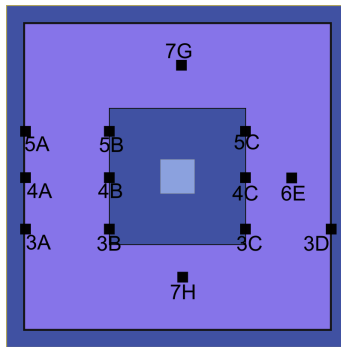


Figure 3.18: AFM scanned areas on a B chip.

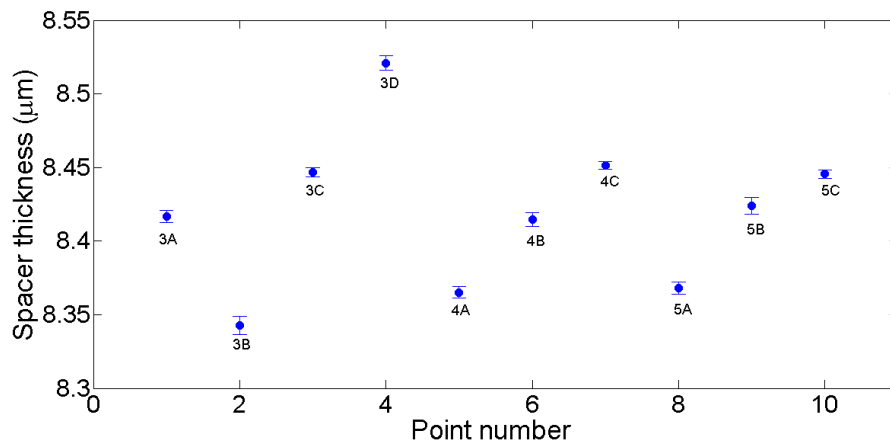


Figure 3.19: Measured heights at different edge locations on a B chip.

From figure 3.19 we can see that the measured spacer heights are distributed in a region between $8.34\ \mu\text{m}$ to $8.52\ \mu\text{m}$, with an increase in height observed as one moves along the A-B-C line. This suggests a “left-to-right” tilt of the edges on the order of $0.1\ \text{mrad}$. The average spacer height of this B chip is estimated to be $8.42 \pm 0.05\ \mu\text{m}$.

Scan location	Average spacer height (μm)
3A	8.417 ± 0.004
3B	8.343 ± 0.006
3C	8.447 ± 0.003
3D	8.521 ± 0.005
4A	8.365 ± 0.004
4B	8.415 ± 0.005
4C	8.451 ± 0.003
5A	8.368 ± 0.004
5B	8.424 ± 0.005
5C	8.445 ± 0.003

Table 4: Summarizing average height measured at specified locations in 3.18.

The AFM measurements for the B chip spacer thickness differ noticeably from that specified by NORCADA. The slight discrepancy between the results obtained by both methods ($8.42 \pm 0.05 \mu\text{m}$ for AFM and $8.65 \pm 0.11 \mu\text{m}$ for profilometer on the same chip) suggests the presence of unaccounted for systematic errors, possibly in the calibration of the AFM.

More measurements performed on different B chips would allow for sampling the distribution, which could be used to compare the results obtained from the optical characterization of the arrays, as will be discussed later.

To evaluate the roughness of the spacer surface, we also scan the surface at various positions on the spacer, namely the areas marked as 6F, 7G and 7H shown in 3.18. We obtain an average surface roughness of $5.5 \text{ nm} \pm 0.3 \text{ nm}$ which suggests a flat and smooth spacer surface for this B chip.

3.2.3 Ellipsometric characterization

Ellipsometry is an optical technique which can provide information on the composition of a layer of thin films, their thicknesses and dielectric properties. We use ellipsometry in this thesis to determine the refractive index and thickness of Si_3N_4 membranes.

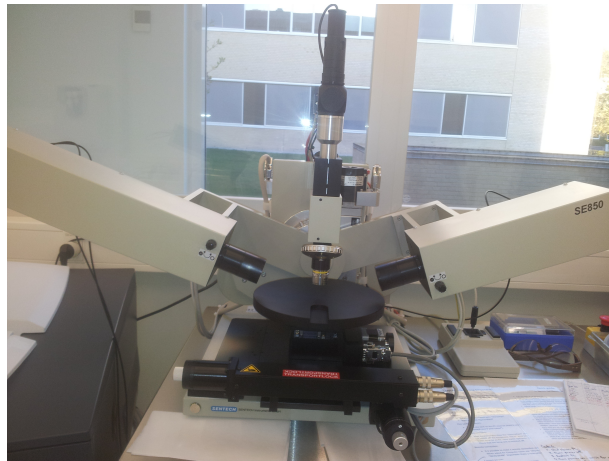


Figure 3.20: Ellipsometer used in this work (Sentech Instruments SE 850).

Figure 3.20 shows the ellipsometer used in this work. It consists of a white light source, movable sample stage, detector and other optical components. The principle of ellipsometer is based on detecting a change in the polarization of light that is reflected

off the sample surface. As shown in scheme 3.21, a white light source sends elliptically or linearly polarized light onto the sample surface. Following which, the reflected light from the surface of the layered model carries information about the material properties. This information is embedded in the Ψ and Δ component of the reflected light, where $\tan(\Psi)$ is the ratio amplitude change upon reflection and Δ is the change in phase, defined as,

$$\frac{r_p}{r_s} = \tan(\Psi) \exp i\Delta \quad (3.2)$$

where r_p and r_s are the normalized p-polarized and s-polarized components of the reflected light, respectively. This ratio can be measured for a wide range of wavelengths.

Ellipsometric measurement is an indirect method which requires a model to relate the variation of Ψ and Δ with wavelength to determine the thin film properties. The model is built by choosing the correct material layer sequence and defining the material properties using predefined data from the ellipsometer.

In this thesis, we use ellipsometry to determine the refractive index and thickness of the Si_3N_4 membrane. Ideally, we are interested in measuring these quantities on the suspended Si_3N_4 films. However, ellipsometry is only suited for thin films on a substrate. We thus perform the measurement on the Si_3N_4 films on the Si substrate and assume that the measured quantities obtained over the substrate are the same as for the suspended film, which is a reasonable assumption as composition and thickness are determined by the deposition parameters during fabrication process. We perform measurements in the UV-visible range (300-820 nm) where a Cauchy model is used for a thin Si_3N_4 film on a thick Si layer.

From fitting the variations of the measured Ψ and Δ with the wavelength to this model, the thickness and refractive index of the Si_3N_4 membranes are extracted over the wavelength range of interest.

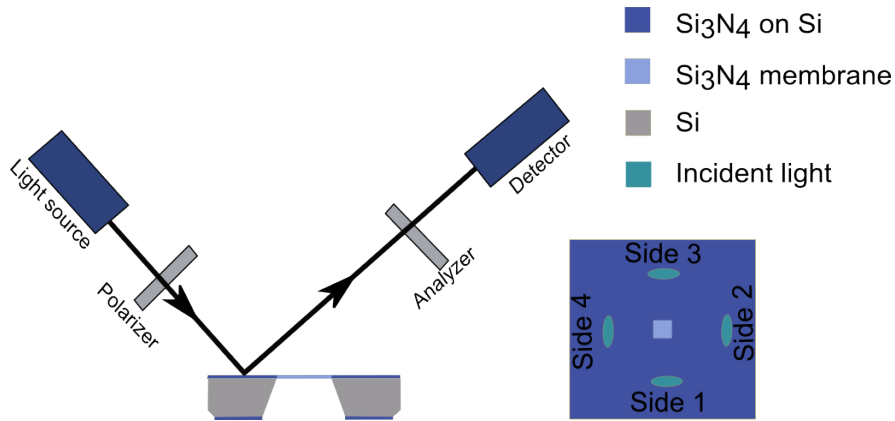


Figure 3.21: Ellipsometer measurement scheme for A chip and 100 μm and 200 μm notched chips. The dark area indicate the spots for the incident light on the chip.

The refractive index extracted from the Cauchy model has a functional dependence on

the wavelength λ given by

$$n(\lambda) = n_0 + \frac{n_1 \times 100}{\lambda^2} \quad (3.3)$$

where λ is in units of nm and n_0 and n_1 are Cauchy coefficients extracted from fitting the data to the model.

The results of the measurements on the 4 sides show that the uncertainties on Cauchy coefficients extracted from the fit are less than the spread of the mean refractive indices. The index is then determined by averaging the Cauchy coefficients obtained from the measurements on the 4 sides of the same chip and the uncertainties estimated by the spread in the measured value.

These measurements are then repeated for different chips from the same batch, the results of which are shown in figure 3.23 and summarized in table 5.

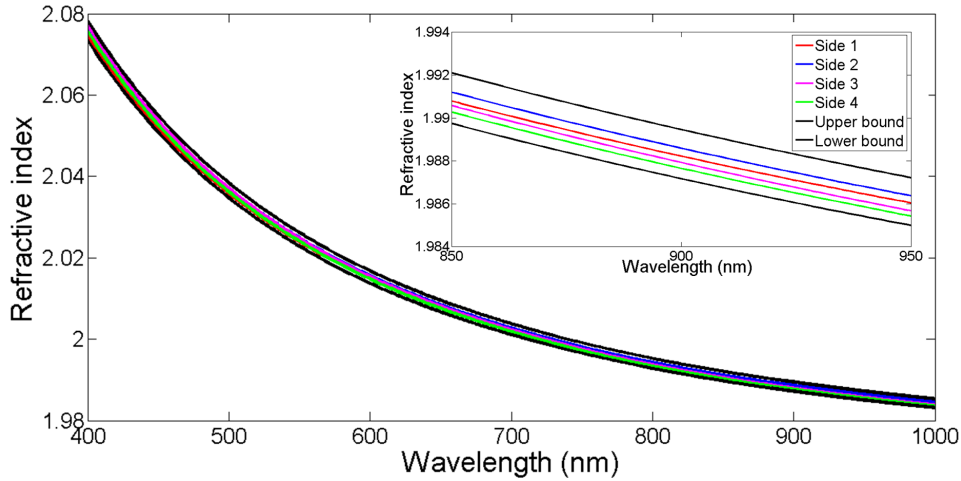


Figure 3.22: Result of ellipsometer measurement on a given A chip. Inset shows a zoom over the region of interest for the monochromatic light transmission measurement.

We make measurements by having the incident light reflect off 4 different spots (one on each side) of a given given chip, as shown in figure 3.21 and 3.22, to evaluate possible deviations in the refractive index and thickness over the chip surface. Figure 3.22 shows one such graph where the extracted refractive index of Si_3N_4 film is shown as a function of wavelength for a given A chip.

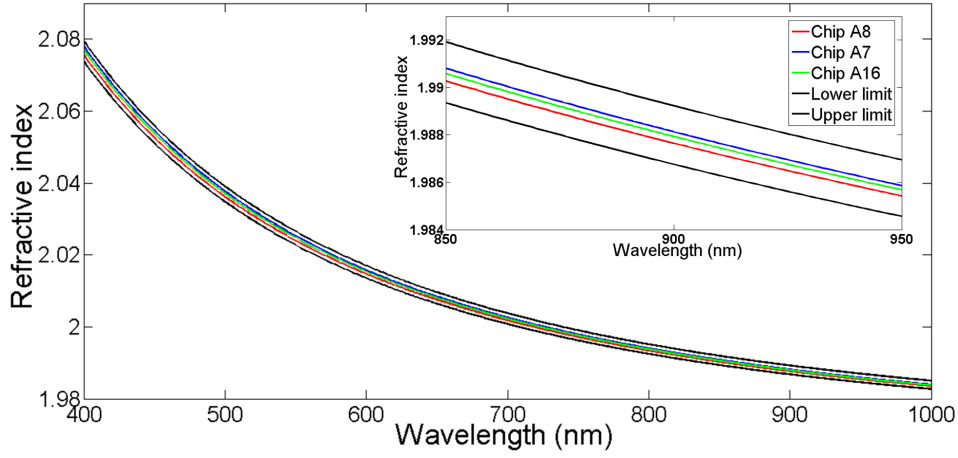


Figure 3.23: Results of ellipsometer measurements on three different A chip's from the same batch. Inset shows a zoom over the region of interest for the monochromatic light transmission measurement.

Chip A	Membrane thickness (nm)	Cauchy coefficient, n_0	Cauchy coefficient, n_1
A7	95.86 ± 0.03	1.966 ± 0.001	180.1 ± 1.2
A8	95.62 ± 0.01	1.966 ± 0.000	176.3 ± 2.2
A16	96.23 ± 0.12	1.967 ± 0.001	174.3 ± 2.5

Table 5 : Summary of extracted thicknesses and Cauchy coefficients for 3 different chip A's from the same batch.

In figure 3.23, we show the measurement results on 3 different A chips from the same batch and in table 5 we summarize the thicknesses and Cauchy coefficients obtained from these measurements. From table 5, the average parameters for the 3 A chip's are found to be $t = 95.9 \pm 0.3\text{nm}$, $n_0 = 1.966 \pm 0.001$ and $n_1 = 176.7 \pm 3.2$. The refractive index n obtained with the n_0, n_1 values in the Cauchy formula are close to theoretically expected value for stoichiometric films [42]. From table 5 we see that, for the model extracted thickness and Cauchy coefficients, there is a very small chip-to-chip variation indicating a rather good homogeneity for chips from the same batch.

Similar measurements were performed on 100 μm notched and 200 μm notched chips. Figure 3.24 shows the result of ellipsometric measurement done on two 100 μm notched chips and table 6 summarizes the result obtained with these measurements. From table 6, the average parameters are found to be $t = 98.8 \pm 0.1\text{nm}$, $n_0 = 1.971 \pm 0.004$ and $n_1 = 158.9 \pm 3.3$ for 100 μm notched chip.

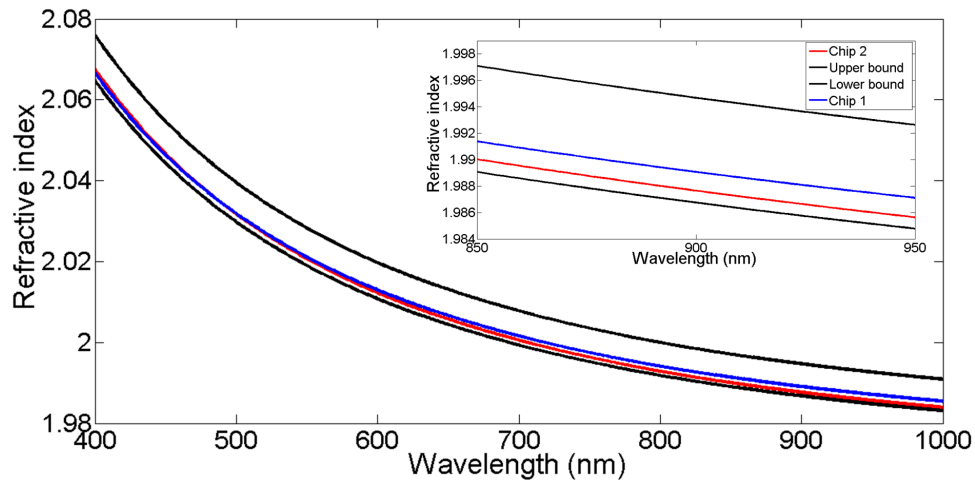


Figure 3.24: Results of ellipsometer measurements on 100 μm notched chips. Inset shows a zoom over the region of interest for the monochromatic light transmission measurement.

Notched 100 μm thick Si chip	Membrane thickness (nm)	Cauchy coefficient, n_0	Cauchy coefficient, n_1
Chip 1	98.9 ± 0.5	1.971 ± 0.004	157.3 ± 3.3
Chip 2	98.7 ± 0.3	1.970 ± 0.003	161.0 ± 1.7

Table 6 : Summary of extracted thicknesses and Cauchy coefficients for 2 different 100 μm notched chips from the same batch.

Figure 3.25 and table 7 show the results of the measurement performed on 3 200 μm notched chips. The average parameters are found to be $t = 93.5 \pm 0.3 \text{ nm}$, $n_0 = 1.964 \pm 0.014$ and $n_1 = 197.2 \pm 8.9$.

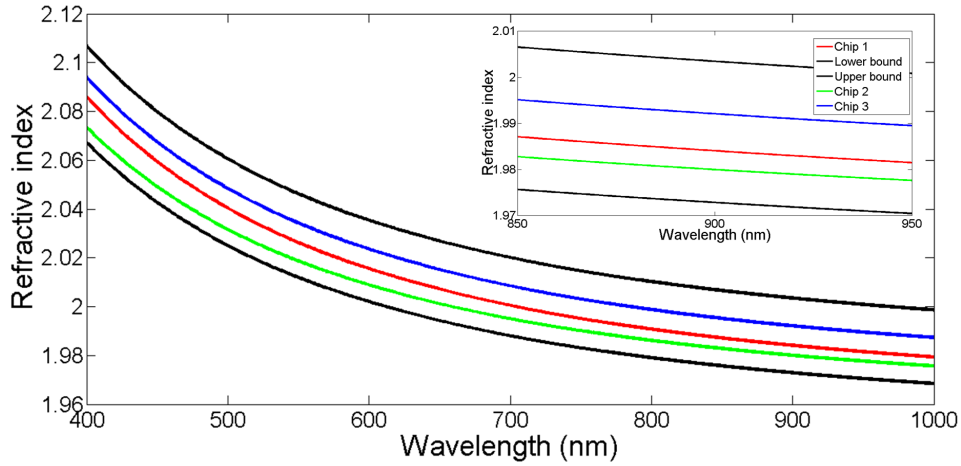


Figure 3.25: Result of ellipsometer measurements on 3 different 200 μm notched chips. Inset shows a zoom over the region of interest for the monochromatic light transmission measurement.

Notched 200 μm thick Si chip	Membrane thickness (nm)	Cauchy coefficient, n_0	Cauchy coefficient, n_1
Chip 1	93.4 ± 1.2	1.97 ± 0.02	204.3 ± 2.7
Chip 2	93.8 ± 0.1	1.955 ± 0.002	187.2 ± 1.8
Chip 3	93.3 ± 1.0	1.97 ± 0.02	204.3 ± 1.5

Table 7 : Summary of extracted thicknesses and Cauchy coefficients for 3 different 200 μm notched chips from the same batch.

In conclusion, we have performed ellipsometric measurement on multiple chips from the batches of A chips, 100 μm notched chips and 200 μm notched chips to estimate the membrane thickness and refractive index variation with wavelength. The measurements show little variation of thickness and refractive index within the same batch but larger variation between different batches, as can be expected from the strong dependence of these quantities on the fabrication condition.

3.3 Fabrication of Si_3N_4 membrane arrays

We now turn to the fabrication of Si_3N_4 membrane arrays using the chips previously discussed.

Our initial attempt to fabricate double membrane arrays uses custom made chip A and chip B. To hold, stack and glue the two membranes, we designed and build a mechanical setup shown in figure 3.27. Before gluing the membranes we have to first preselect a pair of matching membranes with similar lateral chip dimension. This was one of the main challenges with this method, to find chips with matching lateral dimensions, in order to have the two membrane windows overlap well.

In figure 3.26, the image shows overlap of two membranes, an A chip and a B chip, where the colors indicate the lateral mismatch. In figure 3.26(a), the image shows the two membranes in a given orientation to overlap with maximum overlap of the two membrane area. However, in a different orientation as shown in figure 3.26(b) the two membranes are imperfectly overlapping with the result that the membrane area covered by the two membranes being reduced. This suggests that we need to preselect the membranes and fix the orientation before making an array to make membrane arrays with proper overlap of the membrane region.



Figure 3.26: Image showing the lateral overlap of two membranes where the colors show the relative mismatch in dimensions. Figure (a) shows the orientation where the two membranes are closely matched in comparison to a different orientation shown in (b).

To hold, align and glue the membranes we use a home made mechanical setup shown in figure 3.27. In this setup, the two membranes (in blue) are placed on a membrane holder and then mechanically aligned using steel bars (in yellow) with the aim to have the two membrane windows overlap. Once the lateral alignment of membranes is achieved, we bring the top spring and hold the two membranes in place. Then the steel bars are removed from two opposite edges. On the 4 open corners, a small drop of “5 minutter epoxy” glue is deposited and left to be cured for 1 day.

However, due to difficult alignment and lack of reproducible results from the samples glued with this setup, it has since been modified.

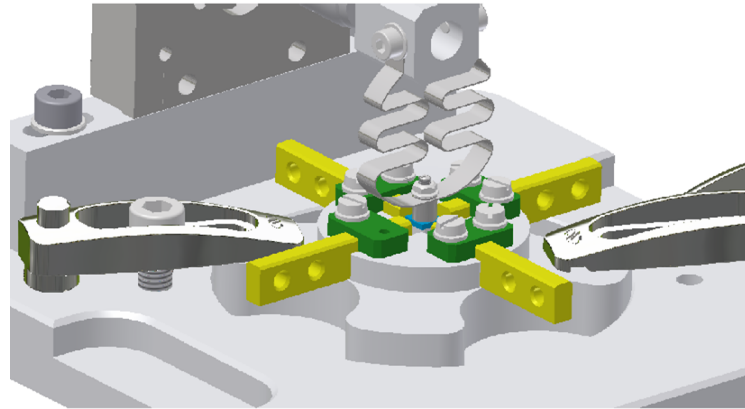


Figure 3.27: Inventor schematic drawing of the first gluing setup showing the membranes in blue, alignment bars in yellow and top spring in gray. The spring is attached to a translation stage which gives the freedom to move the spring in the vertical direction and hold membranes in place through compression force.

3.3.1 $9\ \mu\text{m}$ double arrays

The first double membrane arrays are made with chip A and chip B. As shown in figure 3.28, chip A is a standard single membrane with dimensions defined in table 1. Chip B has a specified $9\ \mu\text{m}$ spacer structure which consists of a layer of Si_3N_4 , SiO_2 and Si as shown in figure 3.28.

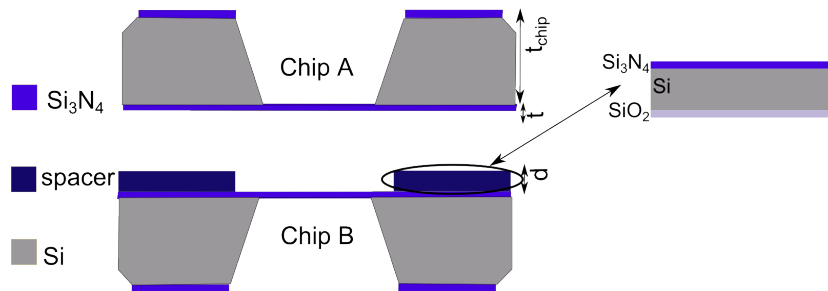


Figure 3.28: Scheme for $9.3\ \mu\text{m}$ double array.

Figure 3.29 shows a picture of the first double array, A4B5, made with the first gluing setup 3.27 and using epoxy glue. This double membrane array gives $> 99\%$ transmission as discussed in the optical characterization section 3.4.

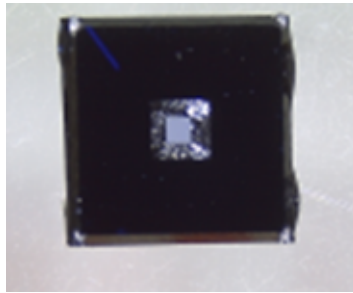


Figure 3.29: Picture of the double membrane array, glued using 3.27 setup.

A new and improved gluing set up has been built and we have also changed glue from epoxy glue to UV cured glue (OrmoComp, Micro Resist Technology) with better results. Since then the new setup has been employed to produce double membrane arrays of both $100\ \mu\text{m}$ and $200\ \mu\text{m}$ notched chips with better reproducibility and improved parallelism between the membranes.

The new membrane holder is shown in figure 3.30, it consists of a small holder with a $300\ \mu\text{m}$ hole at the centre and 4 grooves with movable bars to align the two membranes. The top holder with springs is to hold the membranes in place once they have been correctly aligned. As shown in figure 3.31, the new gluing setup involves a white light source which is a flash light with tungsten bulb, the membrane holder and an optical fiber connected to a spectrometer (Ocean optics HR4000CG-UV-NIR). By monitoring the transmission of the membrane array while positioning the membranes, we have gained better control on the parallelism of the membranes.

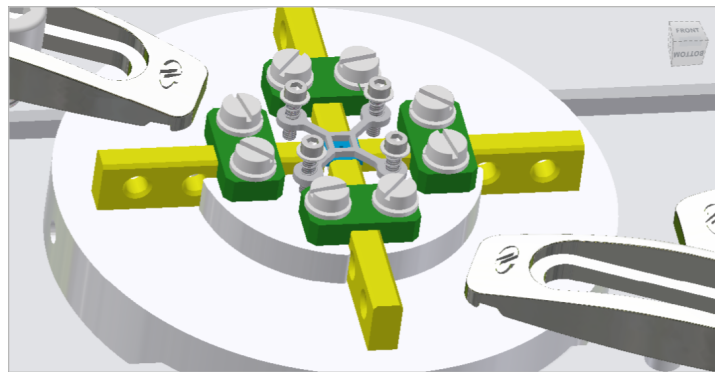


Figure 3.30: Inventor design of the new gluing setup where the top spring has been replaced with a four-point top holder.

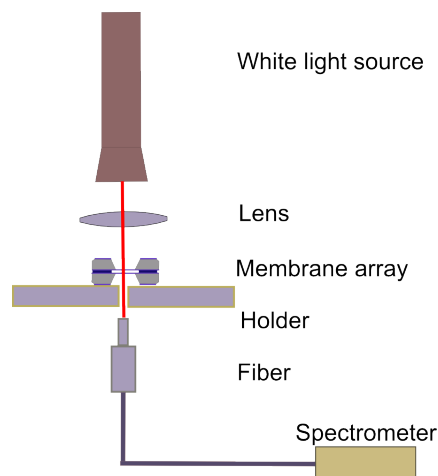


Figure 3.31: New gluing setup showing the flashlight, membrane array, fiber and spectrometer.

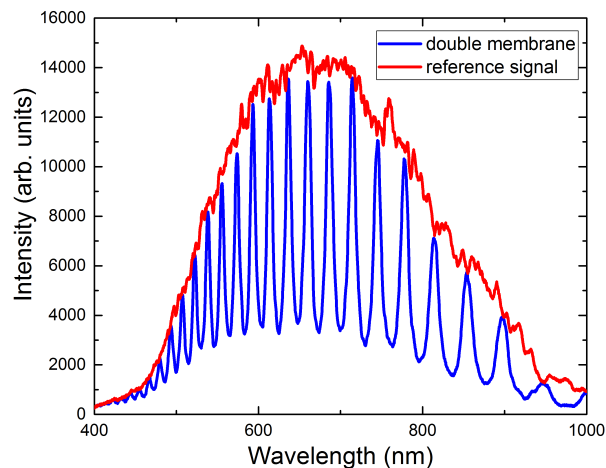


Figure 3.32: Transmission measured by the fiber spectrometer for a $9\ \mu\text{m}$ double array before gluing where the reference (no array) signal is shown in red and the membrane-array transmission signal in blue.

Before placing the membrane chips, we first align the membrane holder with white light source, hole and fiber to get a relatively clean and high intensity signal on the spectrometer as shown by the red line in figure 3.32. Next, both membranes are placed on the holder and aligned with the bars and the top holder to get the transmission signal shown in blue in figure 3.32. One obtains a transmission spectrum displaying two mirror interference fringes. As the mirrors have equal reflectivities, unit transmission is ideally expected when both

membranes are parallel. Once the transmission signal is optimized, the bars are removed and membranes glued by depositing with a needle tip small amount of UV-curable glue at the 4 corners followed by immediate shining of 405 nm laser pointer at the glue for a few seconds.

3.3.2 100 μm and 200 μm double membrane arrays

The new gluing setup is also used to make double membrane arrays with 100 μm and 200 μm notched chips. These chips are notched as shown in figure 3.33, the four notches are cut with precise edges (NORCADA specified notch precision of $\pm 10 \mu\text{m}$) to aid in lateral alignment of the membranes. Figure 3.33, shows a scheme where the membranes are arranged as a stack with the Si chip acting as a spacer to form the arrays.

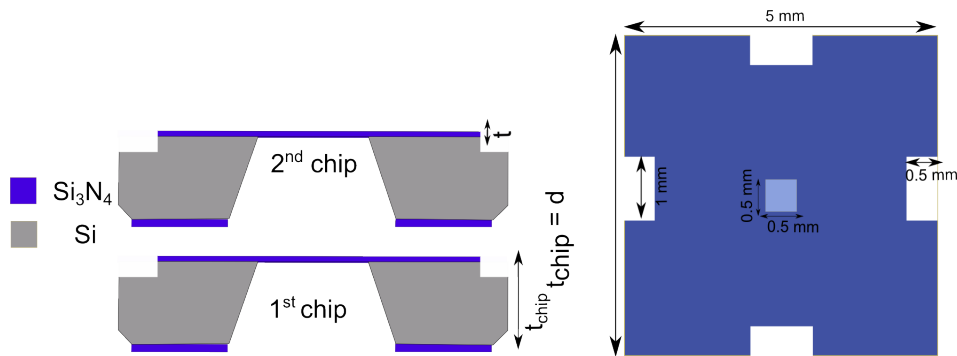


Figure 3.33: Scheme of double membrane array for notched 100 μm and 200 μm thick Si chips.

The procedure for gluing the double arrays is the same as described in section 3.3.1 with the exception that now we use a high resolution spectrometer with a resolution of $\approx 0.1 \text{ nm}$ to see the closely spaced fringes.

We see in figure 3.34, that the transmission signal from the 100 μm notched double membrane array is substantially lower in intensity as compared to the reference signal. This is partly due to imperfect parallelism, but mostly due to the limitation imposed by the resolution of the spectrometer, as will be discussed later.

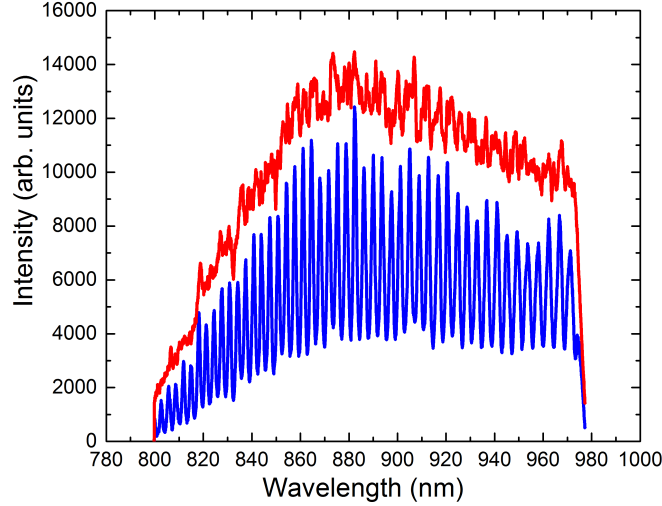


Figure 3.34: Transmission measured by the high resolution fiber spectrometer for the 100 μm double array before gluing where the reference signal is shown in red and double membrane transmission signal in blue.

3.4 Optical characterization of double membrane arrays

In this section we discuss complementary methods for characterizing the optical properties of membrane arrays and apply them to the double membrane arrays assembled previously. Both methods aim at measuring the optical transmission of these array, the first one using a broadband white light source and the other one using a tunable monochromatic laser source. To analyze the experimentally measured spectra we make use of the transfer matrix model introduced in chapter 2 in which the array is modelled as a parallel arrangement of two identical thick dielectric slabs with thickness t , refractive index n and separation distance d between the membranes. The transmission spectrum is then that calculated in section 2.4 of chapter 2 and is in principle a function of n , t and d .

As shown by the ellipsometry measurements, the relative variation of the refractive index in the range of 400 - 1000 nm are rather small ($< 4\%$). In fitting the transmission data to the transfer matrix model we take these variations into account by modelling the refractive index variation using the Cauchy formula

$$n(\lambda) = n_0 + \frac{n_1 \times 100}{\lambda(\text{nm})^2} \quad (3.4)$$

where $n(\lambda)$ is refractive index, λ is wavelength in units of nm, n_0 and n_1 are Cauchy coefficients determined by the ellipsometry measurements.

3.4.1 Transmission measurement of arrays using broadband light illumination

For white light characterization, we use the same setup as for assembling the array 3.31. It consists of a white light source, membrane holder with 300 μm hole in the middle and an optical fiber connected to a spectrometer interfaced with a computer. In these measurements, a reference spectrum is first measured without any membrane. The transmission spectrum of the double membrane array is recorded with the signal optimized to get maximum transmission. The background subtracted ratio of the signals with and without the double membrane array, then gives the normalized transmission spectrum.

In the case of the 9 μm double membrane array, whose spectrum is shown in figure 3.35, we use $n_0 = 1.966 \pm 0.001$ and $n_1 = 176.7 \pm 3.2$ to fit and leave t and d as free fitting parameters. Since the thickness and refractive index are not independently determined in the ellipsometry, we choose to fix only the value of the refractive index.

For the spectrum shown in figure 3.35, using the mean n_0 and n_1 values, we extract from the fit a membrane thickness $t = 93.69 \pm 0.05$ nm and spacer distance between the membranes to be 8567.3 ± 0.1 nm. For the best fitting results, the fitting is performed from $\lambda_{start} = 405$ nm to $\lambda_{end} = 1000$ nm.

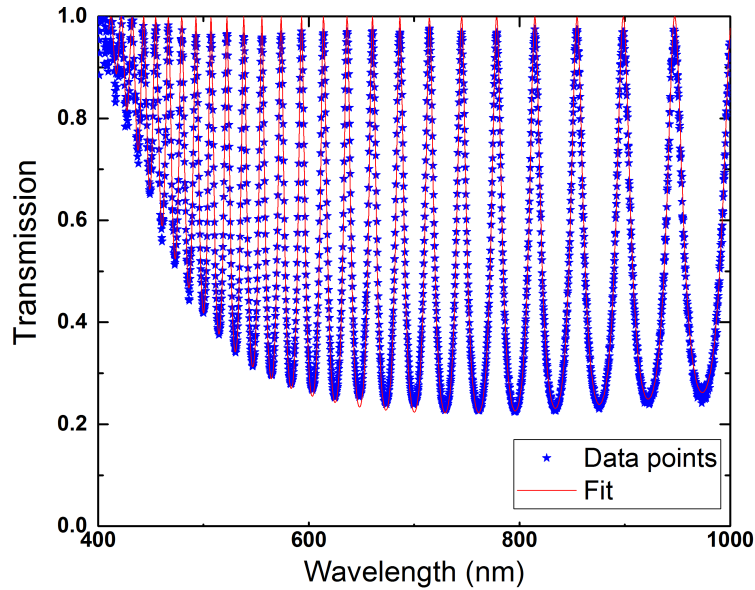


Figure 3.35: White light transmission spectrum for 9 μm double membrane array where the measured data points are shown in blue and the result of the fit to the data in red color, respectively.

To find the error in the determination of the membrane thickness t and spacer thickness

d , we use three sets of Cauchy coefficients $(n0_{\text{mean}}, n1_{\text{mean}})$, $(n0_+, n1_+)$ and $(n0_-, n1_-)$. As shown in table 8, the value of spacer distance that we extract from the fit is consistent for all three sets where d is 8567.3 nm with an error of 0.1 nm. The average membrane thickness is determined to be $t = 93.69$ nm with an error of 0.07 nm, which is almost the same as fitting error obtained using the mean $(n0, n1)$ set. This suggests that the fitting errors obtained on t and d are of the same order as the ones calculated using the limits in the Cauchy coefficient variables. Hence, for further study we are satisfied using only the mean values of $(n0, n1)$ for a given batch of chip and extracting membrane thickness t and spacer distance d with the errors given by the fit errors.

	$n0_{\text{mean}} = 1.966, n1_{\text{mean}} = 176.7$	$n0_+ = 1.967, n1_+ = 179.9$	$n0_- = 1.965, n1_- = 173.5$
t	93.69 ± 0.05	93.62 ± 0.05	93.76 ± 0.05
d	8567.3 ± 0.1	8567.3 ± 0.1	8567.3 ± 0.1

Table 8 : Fitted membrane thickness t and spacer distance d using different values of $n0$ and $n1$.

The membrane thickness reasonably agrees with that determined from the ellipsometry measurements, although the inter membrane separation distance is in contrast quite precisely determined (measurement uncertainty of $\approx 10^{-5}$). This is a consequence of the fact that the two mirror interference spectrum critically depends on this parameter and that the broad band interferometry method allows for measuring many interference fringes simultaneously. The spacing determined with this method is also in agreement with the measured spacer distance using profilometer and AFM techniques.

One downside, though, of this method is to determine precisely the peak transmission of arrays, which is a critical parameter for e.g., the insertion of such arrays within a high finesse optical cavity and the implementation of transmissive optomechanics regime as discussed in section 2.4 of chapter 2. Indeed, the resolution of the spectrometer (0.3 nm) and the inherent noise associated with spatial interferences on the fiber spectrometer detectors resulting from coupling into a fiber prevents an accurate (5% level) determination of the array transmission at a specific wavelength.

3.4.2 Transmission measurement of membrane arrays using monochromatic light illumination

In order to solve this problem and to cross-check the results obtained with the white light transmission measurements we use another method to measure the transmission of a membrane array using well collimated monochromatic light source. The measurement setup is depicted in figure 3.36. The light from an external cavity diode laser (Sacher LION diode laser (TEC 520) in a Littman-Metcalf configuration, shown in the inset of figure 3.36) tunable in the range of 890 - 940 nm, is coupled to a single mode fiber. The output laser beam from the fiber is then split into two on a 50/50 beamsplitter. One part of the split beam is sent to a reference detector (detector 1, Thorlabs DET 36A/M) and

the other part is focussed onto the membrane array with a waist of $50\ \mu\text{m}$ lying on a (Θ, Φ) adjustable mount with a $500\ \mu\text{m}$ hole and detected with another detector (detector 2, Thorlabs DET 36A/M). The outputs of detector 1 and 2 are connected to an oscilloscope (Agilent Technologies DSO-X 2024A).

The laser wavelength is scanned over a certain range by rotating the external mirror in the laser cavity with a step motor as shown in the inset of figure 3.36. For each wavelength λ_i , the power measured by each detector is recorded for 0.1 ms, over the desired wavelength range. Without a sample in place the ratio of the intensities gives the normalization factor $N(\lambda_i)$ defined by

$$N(\lambda_i) = \frac{I2_{\text{without}}(\lambda_i)}{I1_{\text{without}}(\lambda_i)} \quad (3.5)$$

where λ_i is the wavelength at each step i , $I2_{\text{without}}(\lambda_i)$ is the mean intensity measured by detector 2 and $I1_{\text{without}}(\lambda_i)$ is the mean intensity measured by detector 1, without membrane array.

The measurement can then be repeated with a sample in place and the sample transmission is obtained by

$$T(\lambda_i) = N(\lambda_i) \frac{I2_{\text{with}}(\lambda_i)}{I1_{\text{with}}(\lambda_i)} \quad (3.6)$$

where λ_i is discrete wavenegth for each step i , $I2_{\text{with}}(\lambda_i)$ is the mean intensity measured by detector 2 and $I1_{\text{with}}(\lambda_i)$ is mean intensity measured by detector 1, with sample.

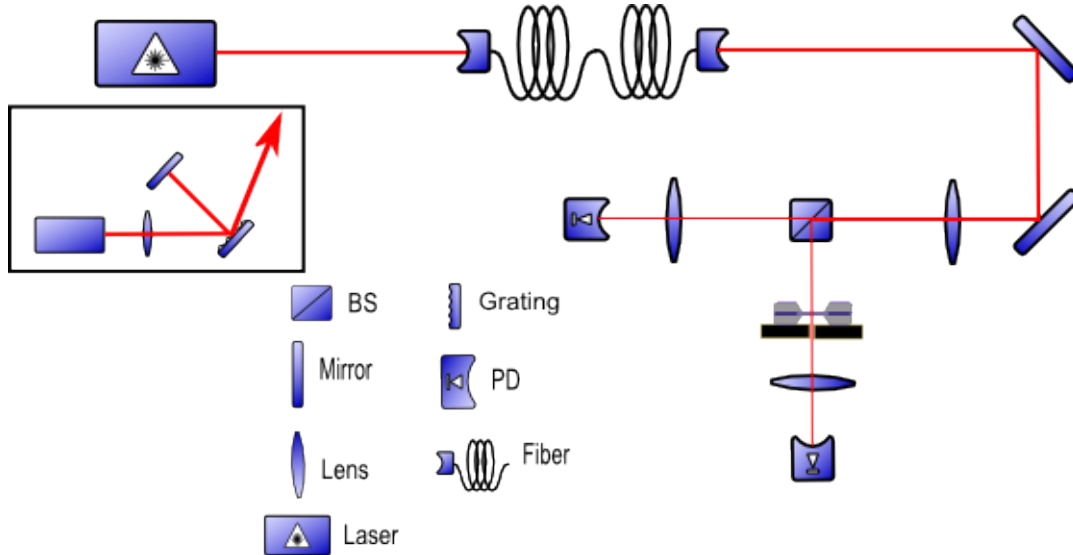


Figure 3.36: Experimental scheme for accurate measurement of the transmission of membrane arrays using monochromatic light. Inset shows a scheme of the diode laser used in the Littman Metcalf configuration.

This method allows for taking care of power fluctuations in the output of the laser when it is scanned and as well as wavelength dependent variations on the transmission of the optical elements. To improve the precision and avoid suspicious “bad” working points of the scanned laser, each scan is repeated 10 times and the ratios without and with the sample averaged.

Figure 3.37 shows the transmission spectrum of the 9 μm double membrane array measured using this method where each data point is an average of transmission obtained in 10 scans and the error bars represent the standard error of mean for this distribution.

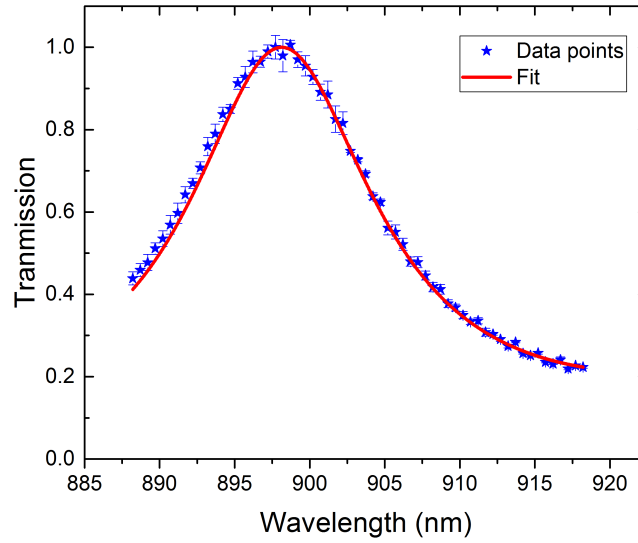


Figure 3.37: Monochromatic light transmission spectrum for 9 μm spacer membrane array fitted with Airy’s function.

To fit single transmission peak we use the standard Airy’s function which works successfully to describe the transmission through a Fabry Perot cavity defined as

$$T = \frac{A}{1 + \frac{4R}{(1-R)^2} \sin^2\left(\frac{2\pi d}{\lambda}\right)} \quad (3.7)$$

From the fit, as shown in figure 3.37, we extract A to be $\equiv 100\%$ with an uncertainty of $\pm 0.8\%$, which gives the lower bound for the peak transmission to be $\approx 99.2\%$.

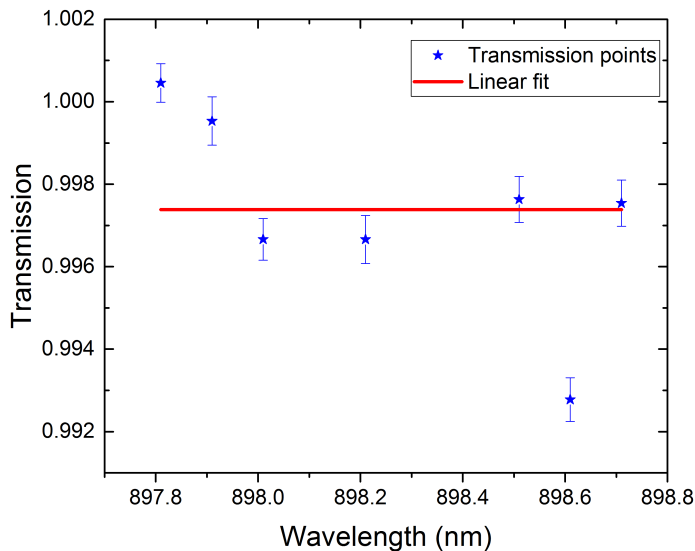


Figure 3.38: Point wise transmission spectrum for 9 μm spacer double array.

To measure the peak transmission even more accurately and avoid the noise resulting from scanning the laser wavelengths, measurements of the intensity ratios with and without membranes are performed for a few points around the peak transmission wavelength (i.e. the wavelength of the laser is not changed between the measurements of with and without membranes for each point).

From the data shown in figure 3.38 we measure a peak transmission of $T_{\text{peak}} = 99.7 \pm 0.1\%$. Similar results have been obtained, albeit with a slightly lower peak transmission (99.2%) with another 9 μm double membrane array assembled in the new gluing setup.

We have also fabricated and characterized 100 μm and 200 μm double membrane arrays using the previous methods. For the white light interferometry measurements a similar fiber spectrometer with higher resolution (≈ 0.1 nm), but narrow range (800 - 1000 nm) was used. The transmission spectrum of such an array is showed in figure 3.39 and 3.40.

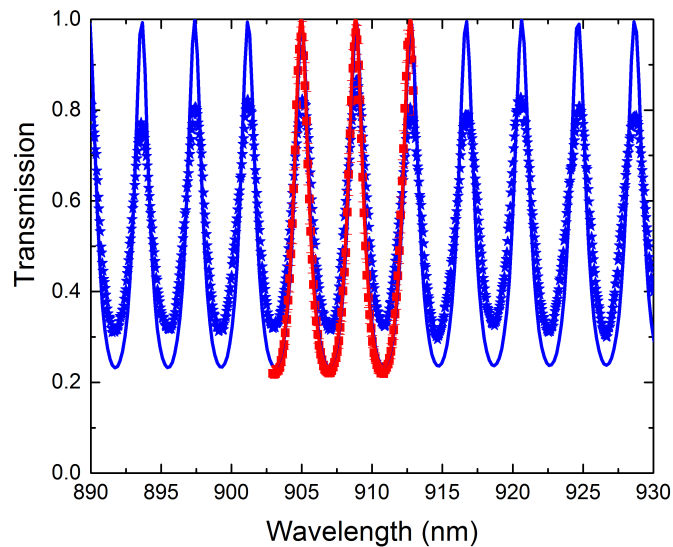


Figure 3.39: Transmission spectrum for 100 μm spacer double membrane array where the red data points represent measured transmission using monochromatic light source and red line represents the fit to this data. Similarly, blue data points present transmission measured using broad band white light illumination and the blue line is the fit to the data.

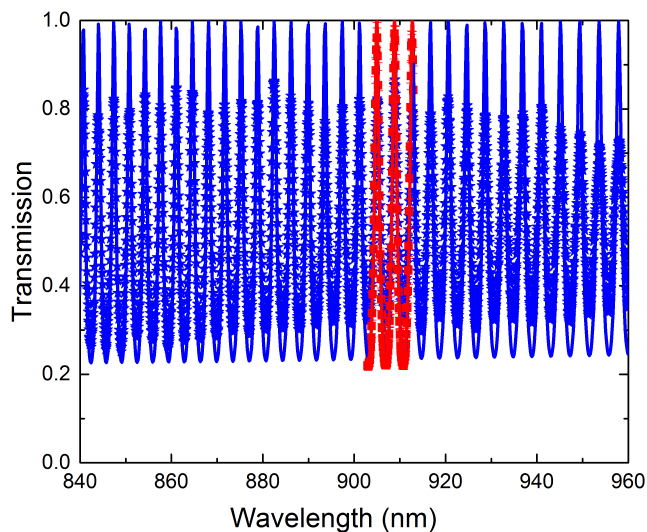


Figure 3.40: Same result as 3.39 with increased wavelength range.

For 100 μm spacer double membrane array, we get a peak transmission of $\approx 97\%$ around 900 nm. The motivation here is to achieve 100% transmission for the membrane array however the reduction in efficiency could be either due to misalignment of the two chips while construction or due to intrinsic tilt in the cavity as a result of a wedged edge. We discuss how a wedge of the chip forming a membrane array affects the transmission of the array in section 3.5.

As shown in figure 3.39 and 3.40, we see that the transmission of the 100 μm spacer double membrane array is measured using both broad band white light source and monochromatic light source and fitted with the full transfer matrix model, as shown in blue and red colors respectively. For 100 μm double membrane array, we use $n_0 = 1.971 \pm 0.004$ and $n_1 = 158.9 \pm 3.3$ to plot and leave t and d as free fitting parameters.

For the spectrum shown in figure 3.39, we extract from the fit a membrane thickness $t = 100.0 \pm 0.3$ nm and spacer distance between the membranes to be $d = 106.359 \pm 0.004$ μm for the white light transmission spectrum and $t = 100.0 \pm 0.4$ nm and $d = 106.355 \pm 0.005$ μm for the monochromatic light transmission spectrum.

In the same way, we measure the transmission of the 200 μm spacer double membrane array using white light source and monochromatic laser source.

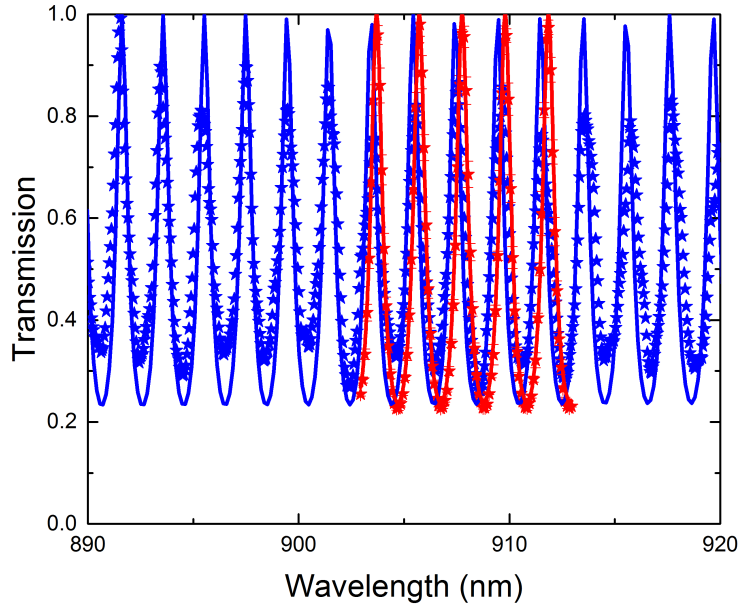


Figure 3.41: Transmission spectrum for 200 μm spacer double membrane array where the red data points represent measured transmission with monochromatic light source and red line represents the fit to this data. Similarly, blue data points present transmission measured with white light illumination and the blue line is the fit to the data.

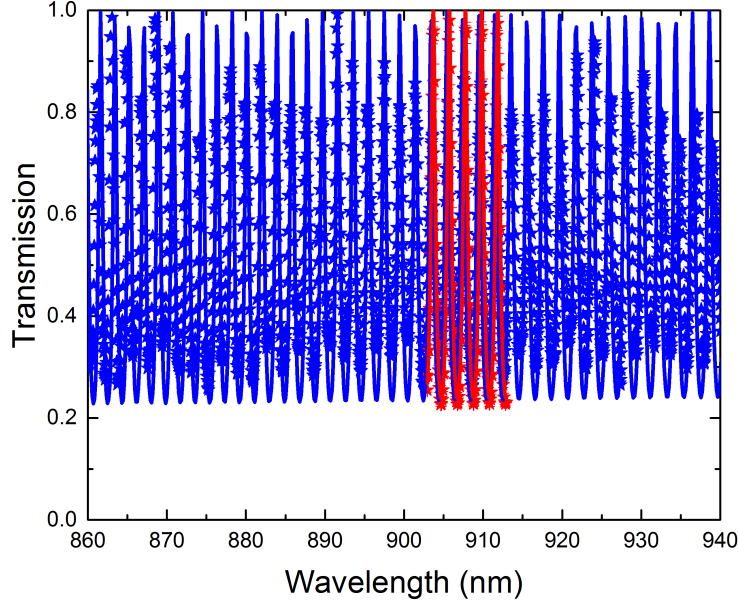


Figure 3.42: Same result as in figure 3.41 with increased wavelength range.

From 3.41 and 3.42, we see that the transmission obtained with monochromatic light source is shifted in wavelength in comparison to the transmission spectra measured using white light source. This is attributed due to the presence of some tilt in the measurement setup, which can be either due to an intrinsic tilt resulting from the wedge of a spacer or an extrinsic tilt due to the membrane holder being tilted.

For 200 μm spacer double membrane array, we get a peak transmission of $\approx 97\%$ near 900 nm. As previously discussed, from fitting the data we obtain the membrane thickness and spacer distance estimate to be $t = 100.0 \pm 0.8$ nm and $d = 204.65 \pm 0.01$ μm for the transmission spectrum obtained using white light source and $t = 97.3 \pm 0.4$ nm and $d = 202.00 \pm 0.01$ μm for the monochromatic laser source.

In conclusion, we have fabricated and optically characterized double membrane arrays with spacer thicknesses of 9 μm , 100 μm and 200 μm using transmission measurements under broadband white light and monochromatic light illuminations. With these first membrane arrays we have been able to achieve a maximum peak transmission of $\approx 99.7\%$ for the 9 μm double membrane array. In the next section 3.5, we consider the factors responsible for reducing the theoretically predicted unity transmission of double membrane arrays.

As a first attempt we also glued a triple membrane array with 200 μm thick spacer chips. Figure 3.43 shows the transmission spectrum obtained with this triple array. Although the peak transmission is far from unity we can see double transmission peaks appearing in the spectrum as expected from theory. [34][37].

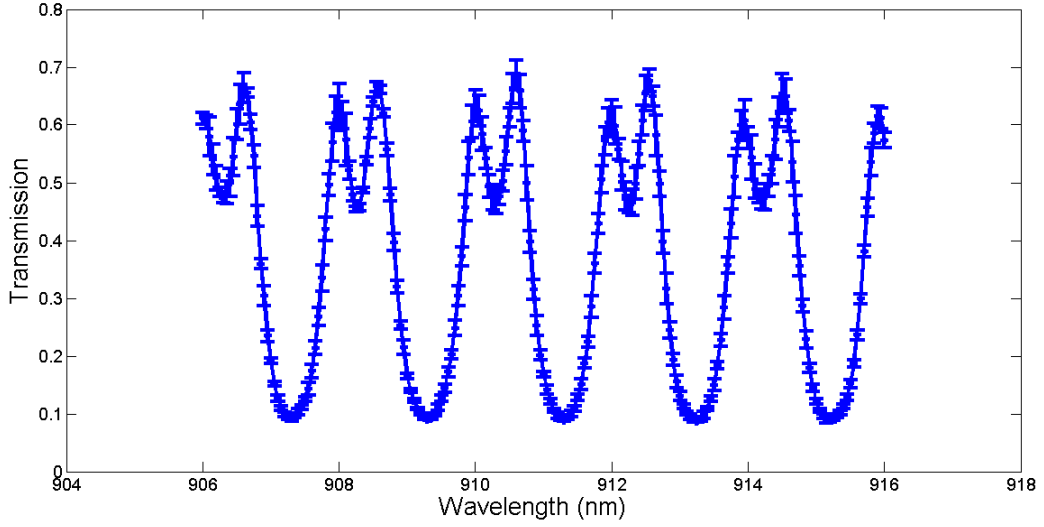


Figure 3.43: Transmission spectrum for 200 μm spacer triple array measured using monochromatic light source where the measured transmission points are shown with the associated error bars.

3.5 Transmission of wedged Fabry Perot cavity

In section 3.4, the experimentally measured transmission for the membrane arrays achieves a maximum of 99.7%. Since our ideal goal is to construct membrane arrays with peak transmission close to 100%, it is important for us to address the different factors responsible for lowering the transmission. There are two main effects which can reduce the unity transmission for a cavity formed with planar reflectors, these are the Gaussian nature of the beam and having non parallel (or wedged) mirrors. These effects are discussed below.

3.5.1 Effect of Gaussian beam size on a planar Fabry Perot cavity

Assume an incident monochromatic Gaussian beam focused at normal incidence on the first mirror with an electric field amplitude (at the first mirror) given by

$$E_{in}(x, y, z) = \exp \left[ik \frac{x^2 + y^2}{2R(z)} - i\psi(z) \right] \exp \left(-\frac{x^2 + y^2}{w(z)^2} \right) \frac{1}{w(z)\sqrt{\pi/2}} \quad (3.8)$$

with the standard Gaussian beam parameters ($z_R = \pi w_0^2/\lambda$) as shown in figure 3.44

$$w(z) = w_0 \sqrt{1 + (z/z_R)^2} \quad (3.9)$$

$$R(z) = z(1 + (z_R/z)^2) \quad (3.10)$$

$$\psi(z) = \arctan(z/z_R) \quad (3.11)$$

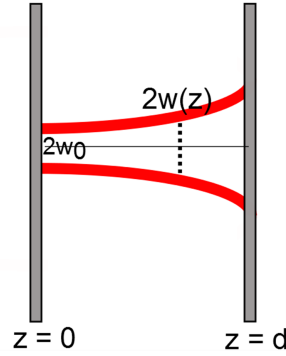


Figure 3.44: Scheme showing a planar Fabry Perot cavity with incident gaussian beam and beam defining parameters

Assuming no wedge between the first and the second mirror as shown in figure 3.44, a mirror separation d and mirrors with equal, frequency independent and real reflection coefficient r_m in amplitude, the field after the second mirror is given by an infinite sum of reflected components

$$E(x, y, d) = \sum_n t_m^2 r_m^{2n} e^{ikz_n} \exp \left[ik \frac{x^2 + y^2}{2R(z_n)} - i\psi(z_n) \right] \exp \left(-\frac{x^2 + y^2}{w(z_n)^2} \right) \frac{1}{w(z_n) \sqrt{\pi/2}} \quad (3.12)$$

where $z_n = (1 + 2n)d$. The transmission can be calculated via

$$T = \int_{-\infty}^{\infty} dx dy |E(x, y, d)|^2 = \int_0^{\infty} dr 2\pi r |E(r, d)|^2 \quad (3.13)$$

where $r = \sqrt{x^2 + y^2}$.

The unity normalization is explicit when taking the limit of a plane wave, i.e. a large Gaussian beam, for which one can neglect the variation of the waist and the phase-shift with z : $R(z) \rightarrow \infty$, $\psi(z) \rightarrow 0$ and $w(z) \rightarrow w_0$. The field amplitude is then given by

$$E(r, d) = \sum_n t_m^2 r_m^{2n} e^{ikd(2n+1)} \exp \left(-\frac{r^2}{w_0^2} \right) \frac{1}{w_0 \sqrt{\pi/2}} \quad (3.14)$$

and its integrated intensity

$$I(d) \equiv \int_0^{\infty} dr 2\pi r |E(r, d)|^2 \quad (3.15)$$

$$= \left| \sum_n t_m^2 r_m^{2n} e^{ik2nd} \right|^2 \int_0^{\infty} dr 2\pi r \exp \left(-\frac{2r^2}{w_0^2} \right) \frac{1}{w_0^2 (\pi/2)} \quad (3.16)$$

$$= \left| \frac{t_m^2}{1 - r_m^2 e^{2ikd}} \right|^2 \quad (3.17)$$

which is equal to $t_m^4/(1 - r_m^2)^2 = 1$ when the Fabry Perot is resonant ($d = m\lambda/2$).

The effect of the Gaussian beam curvature can be evaluated by plotting, e.g., the maximum transmission around a certain wavelength as a function of the waist for different mirror separations as shown in figure 3.45

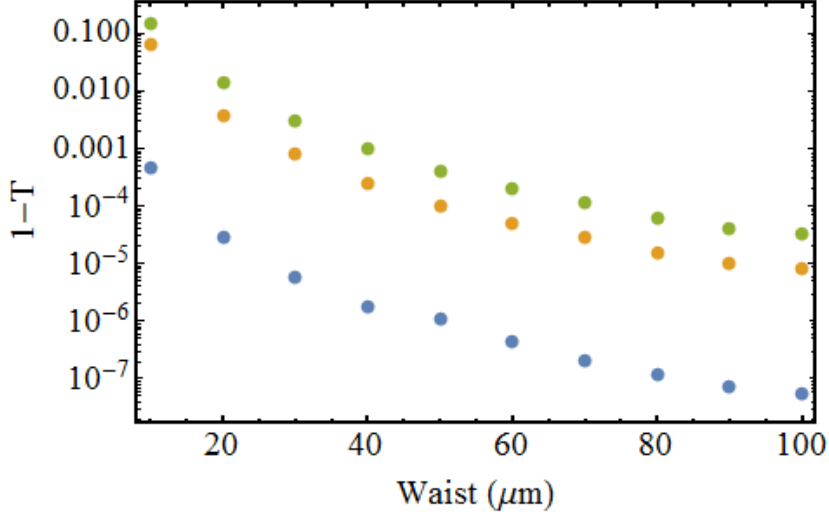


Figure 3.45: $1 - T_{max}$ as a function of w_0 for $d = 8.5$ (blue), 100 (orange) and 200 (green) μm . $r_m^2 = 0.34$ and $\lambda \sim 900$ nm.

For the experimentally measured waist of $\approx 50 \mu\text{m}$, we expect a limit on transmission given by, $1-T \approx 10^{-6}$ for the $8.5 \mu\text{m}$ spacer double membrane array, $1-T \approx 10^{-4}$ for the $100 \mu\text{m}$ and $1-T \approx 4 \times 10^{-4}$ for the $200 \mu\text{m}$ spacer double membrane array.

Since the measured transmission for our membrane arrays are much lower than the predicted values, we can assume that the transmission is not limited by the size of the gaussian beam. In the next section, we consider the effect of having non-parallel or wedged membrane chips.

3.5.2 Wedged Fabry Perot cavity with incident Gaussian beam

In this section, we evaluate the effect of having non parallel or wedged mirrors of a Fabry Perot cavity as shown in figure 3.46. In this configuration, one of the mirrors forming the Fabry Perot tilted at an angle ϵ with respect to the surface of the other mirror.

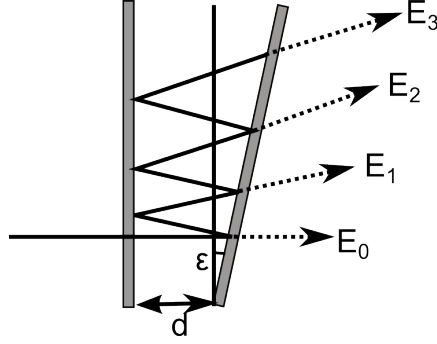


Figure 3.46: Scheme showing a wedged Fabry Perot cavity with a tilted mirror

Let us now assume that the second mirror makes an angle ϵ with the first one in the x -direction. Following reference [44], geometrical considerations for the reflected amplitudes lead to a field at the second mirror given by

$$E(x, y, d) = \sum_n t_m^2 r_m^{2n} E_n(x - x_n(d), y, d + z_n(d)) \quad (3.18)$$

where $E_n(x, y, z) = E_{in}(x \cos(2n\epsilon), y, z + x \sin(2n\epsilon))\sqrt{\cos(2n\epsilon)}$ is the field experiencing a wavefront tilt by $2n\epsilon$, $x_n(d)$ is the transverse walk-off of the n -th outgoing beam, $z_n(d)$ is the difference in distance travelled by the n -th outgoing beam with reference to the direct transmission beam ($n = 0$). This gives

$$E(x, y, d) = \sum_n t_m^2 r_m^{2n} \sqrt{\cos(2n\epsilon)} \exp \left[ik \left(z'_n + \frac{(x - x'_n)^2 + y^2}{2R(z'_n)} \right) - i\psi(z'_n) \right] \exp \left(-\frac{(x - x'_n)^2 + y^2}{w(z'_n)^2} \right) \frac{1}{w(z'_n)\sqrt{\pi/2}} \quad (3.19)$$

with

$$x_n = \frac{d}{\tan(\epsilon)} \left(\frac{1}{\cos(2n\epsilon)} - 1 \right) \quad (3.20)$$

$$z_n = d \frac{\tan(2n\epsilon)}{\tan(\epsilon)} \quad (3.21)$$

$$x'_n = x_n \cos(2n\epsilon) \quad (3.22)$$

$$z'_n = d + z_n + (x - x_n) \sin(2n\epsilon) \quad (3.23)$$

When the waist is large enough so that one can neglect the Gaussian beam curvature the transmission at lowest order in ϵ , can be approximated by

$$T \simeq t_m^4 \int dx \left| \sum_n r_m^{2n} \exp [i2nk(d + x\epsilon)] \exp \left(-\frac{(x - 2n^2 d\epsilon)^2}{w_0^2} \right) \right|^2 \frac{1}{w_0\sqrt{\pi/2}} \quad (3.24)$$

Neglecting the offset in the Gaussian is consistent with $d \ll z_R$, which gives further

$$T \simeq t_m^4 \int dx \frac{\exp\left(-\frac{2x^2}{w_0^2}\right)}{w_0 \sqrt{\pi/2}} \left| \sum_n r_m^{2n} \exp[i2nk(d+x\epsilon)] \right|^2 \quad (3.25)$$

$$= t_m^4 \int dx \frac{e^{-\frac{2x^2}{w_0^2}}}{w_0 \sqrt{\pi/2}} \left| \frac{1}{1 - r_m^2 e^{2ik(d+x\epsilon)}} \right|^2 \quad (3.26)$$

For a transmissive wavelength, $1 - r_m^2 e^{2ik(d+x\epsilon)} = 1 - r_m^2 e^{2ikx\epsilon}$, yielding

$$T_{max} \simeq \int dx \frac{e^{-\frac{2x^2}{w_0^2}}}{w_0 \sqrt{\pi/2}} \frac{1}{1 + F \sin(kx\epsilon)^2} \quad (3.27)$$

where $F = 4r_m^2/(1 - r_m^2)^2$ is the coefficient of finesse of the Fabry Perot cavity. When $kw_0\epsilon \ll 1$, the decrease in transmission is quadratic in ϵ

$$T_{max} \simeq 1 - \frac{F}{4} k^2 w_0^2 \epsilon^2 \quad (3.28)$$

Equation 3.28 suggests that to a good approximation we can estimate the transmission of a wedged Fabry Perot cavity to be dependent only on the Finesse fixed by the mirror reflectivity, spot size and the wavelength of the light. Then the measured transmission is independent of the distance between the mirrors.

As shown in figure 3.47, for the 8.5 μm spaced double membrane array where we estimated a tilt of the order of 0.1 mrad using profilometer (3.2.1) and AFM measurements (3.2.2), we get a upper bound on the transmission of $\approx 99.9\%$.

Thus we should be able to achieve a maximum of 99.9% with a tilt of the order of 0.1 mrad, however there could be other factors which might have degraded the transmission of the membrane arrays. This could be due to a larger wedge introduced in the system because of improper alignment or mishandling during the fabrication process. Further more, any dirt or particles on the surface of the membranes can also affect the parallelism of the membrane-arrays and hence their optical properties. Work to improve the parallelism of the membrane-arrays is under way.

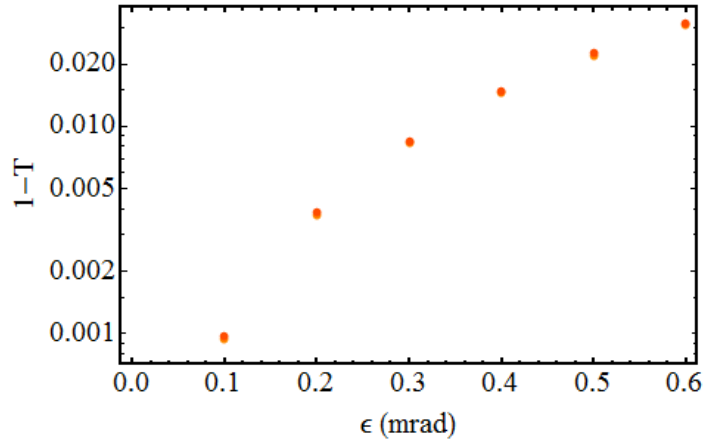


Figure 3.47: $1 - T_{max}$ as a function of ϵ for $d = 8.5 \mu\text{m}$, $w_0 = 50 \mu\text{m}$, $r_m^2 = 0.34$ and $\lambda \sim 900 \text{ nm}$. The results of the exact calculation (3.19) and the approximation (3.27) are indistinguishable (red points), the orange points show the lowest order expansion (3.28).

In conclusion in this chapter, we have discussed how we have characterized the different parameters of interest for the single Si_3N_4 membranes in section 3.2. Followed by section 3.3 where we have discussed how we have designed and developed a mechanical setup to glue the single membranes and create membrane array systems. This mechanical setup has been tried, tested and modified with improvements along each step. In the final sections of 3.4 and 3.5 we have discussed the optical characterization of membrane arrays using complementary methods and develop theory to explain the effect of having experimental imperfections in the double membrane array system.

Chapter 4

Towards cavity optomechanics with membrane arrays

The previous chapter dealt with the assembly of membrane arrays and the characterization of their free space optical properties. In this chapter, we report on the experimental progress towards characterizing their mechanical properties and towards incorporating them into a high finesse optical cavity for cavity optomechanics experiments.

In section 4.1, we describe two experimental setups, a mechanical characterization setup which is designed for vibrational mode spectroscopy of membrane arrays and a high finesse cavity setup for optomechanics experiments. In section 4.2, we tackle an until now unaddressed theoretical issue, namely the effect of the membrane thickness on the collective optomechanical coupling strength of periodic arrays in the transmissive regime and make the connection with the theoretical predictions of chapter 2, obtained in the case of infinitely thin membranes.

4.1 Experimental setup

We have designed and partly assembled two optical setups in their respective experimental vacuum chambers. One interferometric setup referred to as “Mechanical characterization setup” for measuring the vibrational noise spectrum of the membrane arrays and the “Optomechanical cavity setup” to perform the actual cavity optomechanics experiments.

The assembly of mechanical characterization and optomechanical cavity setup is shown in figure 4.1 and it can be seen that both chambers share the same vacuum pumping line. The cavity and mechanical characterization chambers are each connected to a turbo pump (Pfeiffer HiPace80) through an angle valve. To pump either chamber we open the angle valve connecting it to the turbo pump. The turbo pump pumps the chamber down to low pressures of $< 10^{-6}$ mbar. This pressure can then be maintained independently in the respective chambers using an ion pump. The reason we use ion pump to maintain the pressure during experiments is to avoid the vibrations from the turbo pump in the kHz range. The cavity chamber has a 15 liter/sec Varian ion pump and the small mechanical characterization chamber has its own 10 liter/sec Varian ion pump. We use a

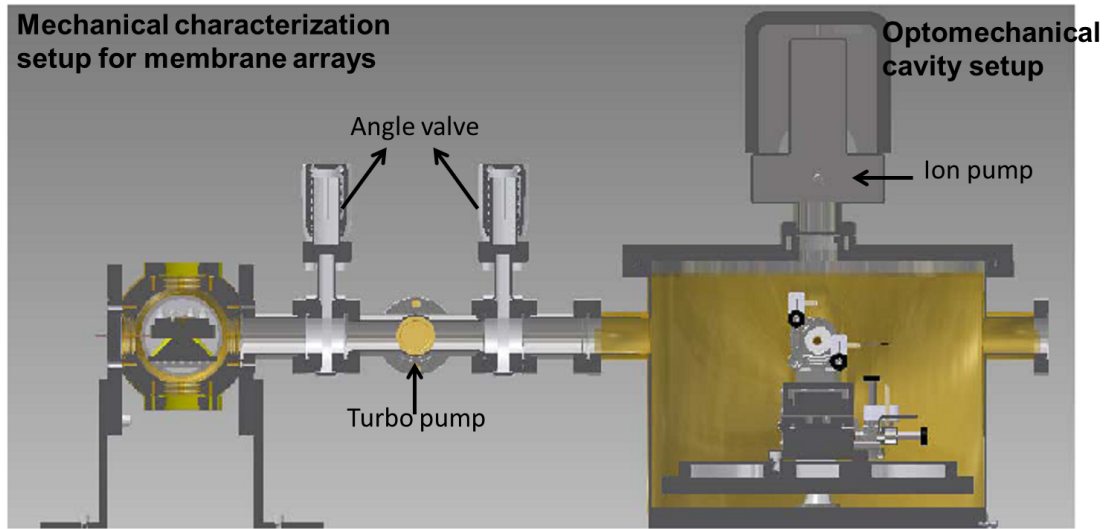


Figure 4.1: Experimental setup consisting of two vacuum chambers one for the mechanical characterization and the other for cavity optomechanical experiments. These vacuum chambers share a turbo pumping line as shown.

small chamber for mechanical characterization setup to be able to switch samples quickly. In the next sections, we discuss how we design and build the mechanical characterization setup followed by a discussion on the design of the cavity setup.

4.1.1 Mechanical characterization setup

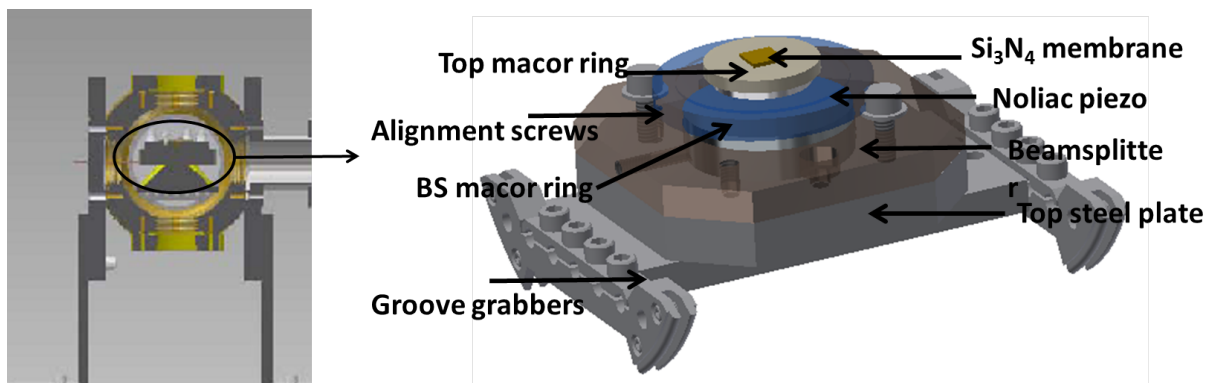


Figure 4.2: Membrane holder assembly inside mechanical characterization chamber showing membrane, top macor ring, piezo, beam splitter macor holder, beam splitter, baseplate and groove grabbers.

In figure 4.1 we see that the vacuum chamber on the left is the mechanical characterization setup. This small chamber is pumped down to $\approx 10^{-6}$ mbar of pressure with a turbo

pump (Pfeiffer HiPace80), which has a maximum rotation speed of 1500 Hz. Once the required low pressure of 10^{-6} mbar is achieved in the chamber, then the turbo pump is switched off and we use an ion pump to maintain this pressure in the chamber.

Figure 4.2, shows the construction inside the chamber. The interferometer setup consists of a low finesse Fabry Perot resonator formed by a membrane (array) and a 50/50 beam splitter. The membrane array is securely placed on a macor ring with a groove that just holds the chip on its corners. This macor ring is then put on top of the piezoelectric actuator (Noliac NAC 2124) referred to as piezo hereafter. The piezo is glued to a bigger macor ring (beam splitter macor ring) which is placed on the beamsplitter. The beamsplitter macor ring height can be adjusted using custom made screws as shown in figure 4.2. The freedom to move the membrane holder assembly allows to align the membrane parallel to the beamsplitter. The beamsplitter fits inside a stainless steel base plate which is designed to fit in the vacuum chamber. The whole construction is placed on groove grabbers attached to the side flange in vacuum chamber.

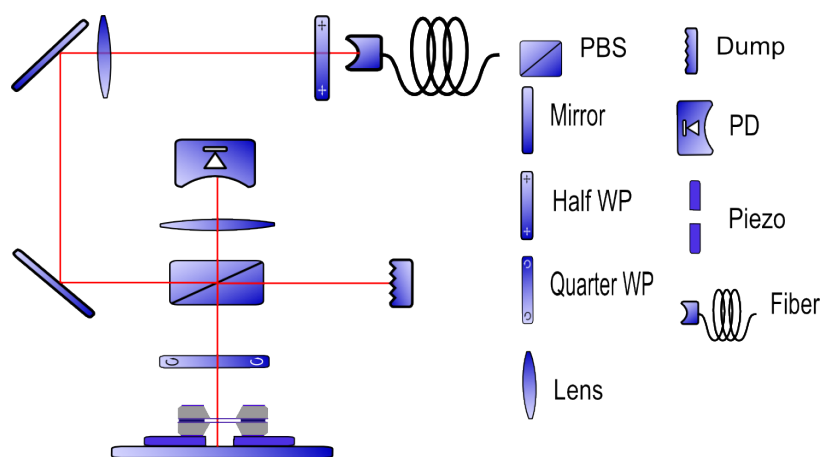


Figure 4.3: Optical layout of mechanical characterization setup showing a low finesse Fabry Perot cavity formed with the membrane array and a beamsplitter.

The mechanical characterization chamber has two view ports through which we can input and extract laser light. The optical layout for the experiment is as shown in fig.4.3. A diode laser (Sacher LION TEC 520) provides monochromatic light in the wavelength range from 890 - 940 nm. The laser beam after passing through a double-pass Acousto Optic Modulator (AOM) is coupled to a polarization maintaining fiber. The output beam from the fiber then passes through a half wave plate (HWP), is steered using mirrors, and sent vertically downwards using a polarizing beamsplitter (PBS). The beam passes through a quarter wave plate (QWP) and is then directed towards the low-finesse cavity inside the vacuum chamber. For positioning and aligning of the membrane, we use a CMOS camera (DCC 1545M) placed close to the top window. We extract either the retro-reflected or transmitted light from the cavity and direct the signal to a low-noise transimpedance photodetector (Thorlabs PDA8A).

First, the interferometer is aligned to get maximum interference contrast when scanning the Fabry Perot cavity length. Then the cavity length is set to the flange of interference fringe to get most sensitivity to vibrations.

The signal from the photodetector is then sent to a spectrum analyzer (Tektronix RSA 103 B) which can be used as a spectrum analyzer or network analyzer. Spectrum analyzer is used for measuring the thermal noise spectra of the membranes. The measurement depends on the bandwidth used for measurement in comparison to the mechanical linewidth (Γ_m) of the resonator. The mechanical spectra at higher bandwidth shows all possible mechanical modes in a given frequency range. To resolve each peak and determine its linewidth, a lower bandwidth and higher resolution measurement has to be made. A mechanical spectra gives the mechanical resonance frequencies for the various modes of vibration. The associated mechanical quality factor for each mode is then extracted from the lorentzian fit to the peaks of the mechanical spectra. We use a spectrum analyzer (Tektronix RSA 103 B) with very low resolution bandwidths ($\approx 0.1\text{Hz}$) which is required to measure resonance frequencies in the MHz regime with mechanical quality factors of $\approx 10^6$. But these measurements typically require long acquisition times during which thermal drifts tend to broaden the measured peaks.

To make an even more precise determination of the quality factor of membrane arrays we can use “Ringdown technique”. This is a standard measurement technique used to measure mechanical quality factors of single membranes with high precision [43]. In these measurements, the membrane is excited at one of its resonance mode frequencies and then the amplitude decay of the membrane vibration is recorded with network analyzer. Fitting the exponential decay curve gives us the mechanical quality factor of the membrane mode.

We have build and vacuum tested the mechanical characterization chamber and aligned the optical setup. As per high vacuum requirements, all stainless steel parts were cleaned by ultrasonication in isopropanol for ≈ 1 hour and then vacuum baked at 120°C . The macor rings and piezos were first soaked in isopropanol for 4-5 hours and then soaked in ethanol for 4-5 hours. Kapton wires used for making electrical connection to piezo’s were also cleaned via ultrasonication in isopropanol.

For all gluing purposes, we use a vacuum compatible glue (5 minutter epoxy glue). And for making electrical connections we use a vacuum compatible electrically conductive glue. In the course of vacuum testing, we realized that a vibration isolation damper from Newport (ND 50-A)(which was a part of the first design) was degassing and hence incompatible with our vacuum requirements. Following which we redesigned the setup and replaced the damper with a stainless steel base plate.

This setup has now been tested by Andreas Naesby (current post-doc in optomechanics group) and used to make measurements of the mechanical properties of the previously assembled arrays. At the time of writing these measurements were still in progress.

4.1.2 Optomechanical cavity setup

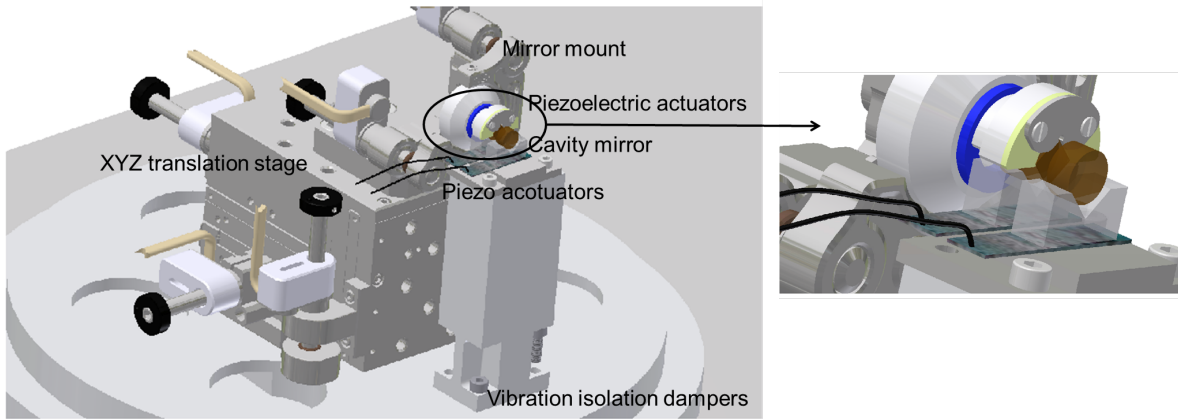


Figure 4.4: Cavity setup showing the MIM formed with membrane array and cavity mirrors. Also shown are the 5-axis stage for positioning of the membrane(s) in the cavity.

The optomechanical cavity chamber is designed to emulate the array-in-the-middle setup [43]. As shown in figure 4.4 this setup requires a membrane or membrane array to be positioned mid way between cavity mirrors of a high finesse cavity. For precise positioning and tilt adjustment of the membrane array, it is mounted on a mirror mount with piezoactuators (Newport 8302-V) and XYZ translation stage (Newport M-562-XYZ) also with piezoactuators (Newport 8302-V) controlled by picomotor (Newport 8743-CL), as shown in figure 4.4. The membrane array is attached to a piezoelectric actuator (Noliac NAC 2124) to excite the membrane mechanical modes of vibration. The whole assembly is mounted on a vibration isolation system consisting of a heavy baseplate placed on 3 vibration isolation dampers (Newport ND 50 A).

Up until now, we have designed, cleaned and produced the parts and vacuum tested the cavity chamber. In the future, we have to assemble, align and test the cavity followed by the first optomechanical experiments with membrane arrays.



Figure 4.5: Cavity setup showing the MIM formed with membrane array and cavity mirrors.

Figure 4.5 shows the Fabry Perot cavity formed by identical spherical mirrors from AT Films. The mirrors are mounted on V-blocks with the same thermal expansion coefficient as the material of mirrors to avoid thermal expansion mismatch. The V-blocks are attached to piezoelectric transducer shearing plates (Ferroperm PZ 27). The spherical mirrors are specified to have a transmission of 50 ppm at a wavelength of 900 nm (bandwidth ≈ 100 nm) and radius of curvature to be $R = 25$ mm. In the absence of absorption losses, the maximum achievable finesse \mathcal{F}

$$\mathcal{F} = \frac{2\pi}{2T} \quad (4.1)$$

would be $\mathcal{F} \approx 60000$ at 900 nm.

We assume the input laser beam to the cavity to have a Gaussian profile and in which case the waist of the beam at the center of the cavity as a function of cavity length is expressed as [45][46],

$$w_0 = \sqrt{\frac{\lambda L}{\pi}} \left(\frac{g_1 g_2 (1 - g_1 g_2)}{(g_1 + g_2 - 2g_1 g_2)^2} \right)^{\frac{1}{4}} \quad (4.2)$$

where $g_1 = g_2 = 1 - \frac{L}{R}$, L is cavity length.

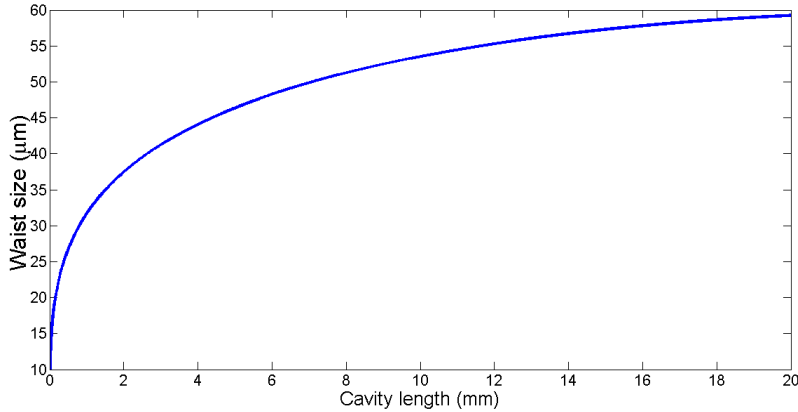


Figure 4.6: Cavity waist radius as a function of cavity length at wavelength $\lambda = 900$ nm and radius of curvature $R = 25$ mm.

For a given wavelength $\lambda = 900$ nm and radius of curvature of mirrors $R = 25$ mm, figure 4.6 shows the waist as a function of cavity length. We see that we reach to a waist of about 50 mm for a cavity length of $L \approx 7.1$ mm which we can use as a reference.

For a length of $L = 7.1$ mm, we find the cavity decay rate, κ , defined as

$$\kappa = \frac{cT}{2L} \quad (4.3)$$

to be $\frac{\kappa}{2\pi} \approx 175$ kHz.

Comparing with the typical mechanical mode frequencies ($\frac{\omega_m(1,1)}{2\pi} \approx 800$ kHz) reaching such a value would allow us to operate well in the resolved sideband regime.

4.2 Optomechanics in the thick membrane regime

In this section, we discuss our recent findings on how the membrane thickness is expected to affect optomechanical properties of a membrane array system [38]. In the theoretical discussion presented in Chapter 1, we assume the membrane to be thin with respect to the wavelength of the incident light λ , which means that $nl \ll \lambda$ where n is the refractive index and l is the thickness of the membrane. However for the arrays characterized in chapter 2 with a thickness of $l = 100$ nm and a refractive index of $n \approx 2$, the thin membrane approximation is not well met, as $nl = 200$ nm, is not much smaller than the wavelength $\lambda = 900$ nm.

We address here these issues by investigating the effect of the membrane thickness on the transmission spectrum of a periodic array of flexible membrane resonators, as well as on the collective optomechanical coupling of the membranes with the field of an optical resonator. Based on a full transfer matrix approach we first show in Sec. 4.2.1 that arbitrarily thick membranes can be modelled as effective thin membranes and compute the transmission spectrum of a two-membrane array. In Sec. 4.2.2 we investigate the optomechanical properties of such an array positioned at the center of a large optical resonator (cavity). We compute in particular the strength of the optomechanical couplings at specific “transmissive” wavelengths, where the array is effectively transparent and for which the field dispersively couples linearly to a collective motion of the individual membranes. We also make the connection with the results of Refs. [34, 37], obtained in the thin-membrane approximation, and extend them to the case when multiple field oscillations can occur inside the individual membranes.

4.2.1 Optical properties

4.2.1.1 Transfer matrix model

As in previous studies [34, 37] we restrict ourselves to one-dimensional systems and make use of the transfer matrix formalism, which is well-suited to model a periodic N -element array. In this formalism each element is described by a transfer matrix M relating the forward- and backward-propagating waves on each side of a given element [47, 48]

$$\begin{pmatrix} A \\ B \end{pmatrix} = M \begin{pmatrix} C \\ D \end{pmatrix} = \begin{bmatrix} m_{1,1} & m_{1,2} \\ m_{2,1} & m_{2,2} \end{bmatrix} \begin{pmatrix} C \\ D \end{pmatrix}, \quad (4.4)$$

with A and C (B and D) are the amplitudes of the backward-propagating (forward-propagating) waves. For example, the free-space propagation of a monochromatic field of wavelength $\lambda = 2\pi/k$ over a distance d is described by the matrix

$$M_{\text{fs}}(d) = \begin{bmatrix} e^{ikd} & 0 \\ 0 & e^{-ikd} \end{bmatrix}. \quad (4.5)$$

For an incoming field propagating to the right the transmissivity and reflectivity of the optical system modelled by M are defined by

$$t = \frac{1}{m_{2,2}}, \text{ and } r = \frac{m_{1,2}}{m_{2,2}}. \quad (4.6)$$

4.2.1.2 Single membrane transfer matrix

Each membrane is modelled as a dielectric slab with thickness l and refractive index n . To simplify the discussion we assume the refractive index to be wavelength-independent and neglect absorption in the wavelength range considered, but these effects could easily be incorporated into our model. The Fresnel coefficients at normal incidence at the left and right vacuum–dielectric interfaces yield amplitude reflection and transmission coefficients

$$\rho_l = -\rho_r = \frac{1-n}{1+n} \equiv \rho, \quad (4.7)$$

and

$$\tau_l = \frac{2}{1+n} \text{ and } \tau_r = \frac{2n}{1+n}, \quad (4.8)$$

respectively. The transfer matrix of the slab with length l can thus be written as

$$M_m = M_l M_{fs}(nl) M_r, \quad (4.9)$$

where

$$M_i = \frac{1}{\tau_i} \begin{bmatrix} 1 & \rho_i \\ \rho_i & 1 \end{bmatrix} \quad (i = l, r). \quad (4.10)$$

The reflection and transmission coefficients of the membrane are then given by [34, 39]

$$r_m = \frac{\rho(1 - e^{2iknl})}{1 - \rho^2 e^{2iknl}}, \text{ and } t_m = \frac{\tau_l \tau_r e^{iknl}}{1 - \rho^2 e^{2iknl}}. \quad (4.11)$$

The equivalent membrane polarizability $\zeta \equiv -ir_m/t_m$ is then

$$\zeta = \frac{n^2 - 1}{2n} \sin(knl). \quad (4.12)$$

Eqs. (4.9)–(4.12) hold for any membrane thickness. However, in the spirit of Refs. [34, 47], it can be convenient to model the membrane as an infinitely thin scatterer with an effective transfer matrix

$$\tilde{M}_m = \begin{bmatrix} 1 + i\zeta & i\zeta \\ -i\zeta & 1 - i\zeta \end{bmatrix}, \quad (4.13)$$

where ζ is given by Eq. (4.12), which gives reflection and transmission coefficients having the same amplitude as that of the equivalent membrane having arbitrary thickness. However, the thin-membrane model ignores the phase shift acquired by the field propagating through the membrane, which may be relevant, e.g., for propagation in a multi-membrane array and for taking into account field resonances inside individual membranes.

To take this phase shift into account one can introduce an extra padding of length ϕ/k to each side of the membrane so that its transfer matrix becomes

$$M'_m = M_{\text{fs}}(\phi/k)\tilde{M}_m M_{\text{fs}}(\phi/k), \quad (4.14)$$

with a padding phase

$$\phi = \begin{cases} \phi_0 + \pi \lfloor nl/\lambda \rfloor & \text{if } \sin(knl) > 0 \text{ and} \\ 2\pi - \phi_0 + \pi \lfloor nl/\lambda \rfloor & \text{if } \sin(knl) < 0, \end{cases} \quad (4.15)$$

where $\lfloor \cdot \rfloor$ represents the floor function and

$$\phi_0 = \frac{1}{2} \arccos \left[\frac{(n^2 - 1) + (n^2 + 1) \sin(knl)}{(n^2 + 1) + (n^2 - 1) \sin(knl)} \right]. \quad (4.16)$$

As can be seen from the example shown in Fig. 4.7, the resulting effective thin membrane conveniently models the propagation of the field outside the membrane.

4.2.1.3 Periodic membrane array transfer matrix

We consider a periodic array of N identical, arbitrarily thick membranes, each modelled by a transfer matrix M_m and separated by a distance d . The transfer matrix of the array is then computed as

$$M_N = M_m M_{\text{fs}}(d) M_m \cdots M_m, \quad (4.17)$$

where M_m appears N times. The transmittance of the array $\mathcal{T} = 1/|(M_N)_{2,2}|^2$ can be compared to that of the corresponding array of effective thin membranes $\mathcal{T}' = 1/|(M'_N)_{2,2}|^2$, where M'_N is defined by substituting M'_m for M_m in Eq. (4.17).

4.2.1.4 Two membrane arrays

In this section we focus on the case of a two membrane arrays and use as an example silicon nitride membranes as employed in our experiments.

Figure 4.8 shows the transmission spectrum of a two-membrane array with refractive index $n = 2$, thickness $l = 100$ nm and spacing $d = 9$ μm . The single-membrane transmittance spectrum is also displayed as reference. Unity transmission is achieved, as expected, when the reflectivity of the individual membrane, r_m , vanishes; this occurs when its effective thickness nl is an integer multiple of $\lambda/2$. Unity transmission can also be achieved in a two-membrane array when there is perfect constructive two-mirror interference, which occurs at the “transmissive” wavelengths discussed in previous chapters. As the figure illustrates, spectra resulting from the effective thin-membrane model (dashed curves) perfectly overlap with the results from the full model, showing the equivalence between the two models regarding free-space optical transmission.

Also shown is the curve resulting from the thin membrane model calculations for a membrane with an equivalent ζ which gives the transmission peaks at wrong positions.

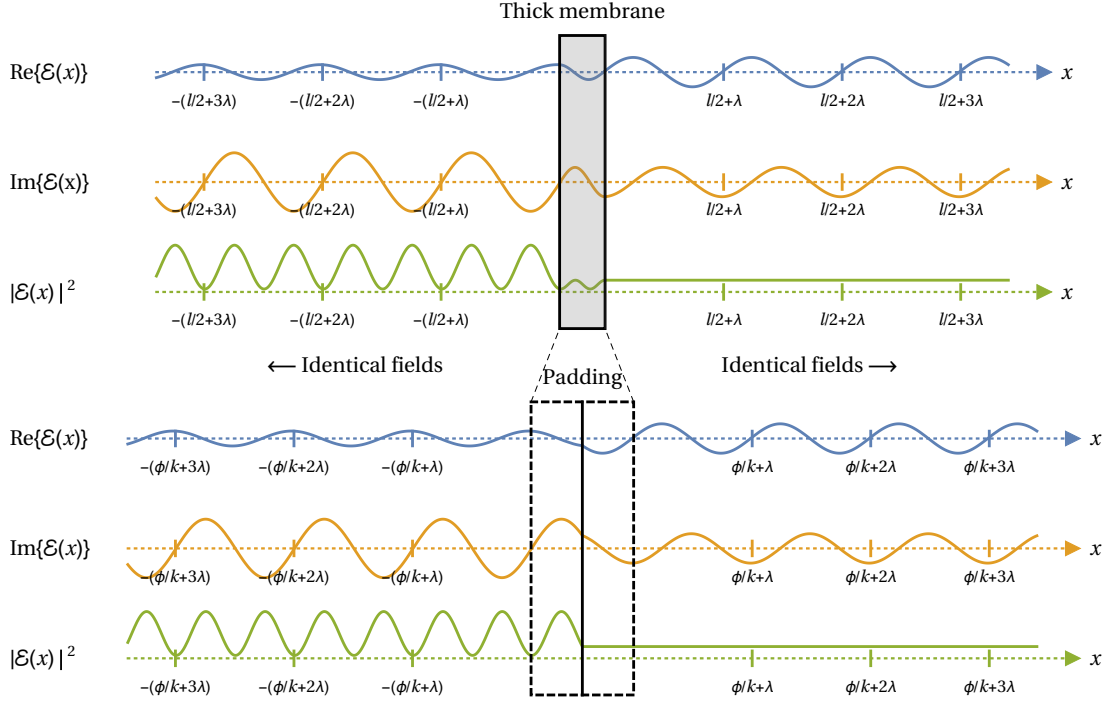


Figure 4.7: Equivalence between a thick membrane (top) and an effective thin membrane with padding (bottom). From top to bottom in each of the subfigures, the curves illustrate the real (blue), imaginary (orange), and squared modulus (green) of the electric field, in arbitrary units, as a function of position. The shaded rectangle in the top subfigure shows the dielectric slab, while the dashed rectangle in the bottom subfigure show the extent of the padded areas around the infinitely thin membrane. Note that the fields outside the shaded (top) and dashed (bottom) rectangles are identical in both amplitude and phase.

4.2.2 Cavity optomechanics

We now turn to the case of vibrating membranes positioned inside a (large) optical resonator and wish to investigate the role of the membrane thickness on the optomechanical coupling with the cavity field. Of particular interest, in connection with the results of Refs. [34, 37], is the strength of the optomechanical coupling at the aforementioned transmissive wavelengths, where the field couples dispersively and linearly to a collective motion of the individual membranes.

4.2.2.1 Optomechanical coupling

The N -membrane array, where $N = 2$ here, but our discussion applies generally, is assumed to be at the center of a symmetric linear Fabry–Pérot cavity of length L . The length of the array is supposed to be much smaller than that of the cavity and the cavity field Rayleigh range. The cavity mirrors are modelled by a transfer matrix M_c of the form (4.13) and their polarizability is denoted by ζ_c . The total transfer matrix of the system can thus be

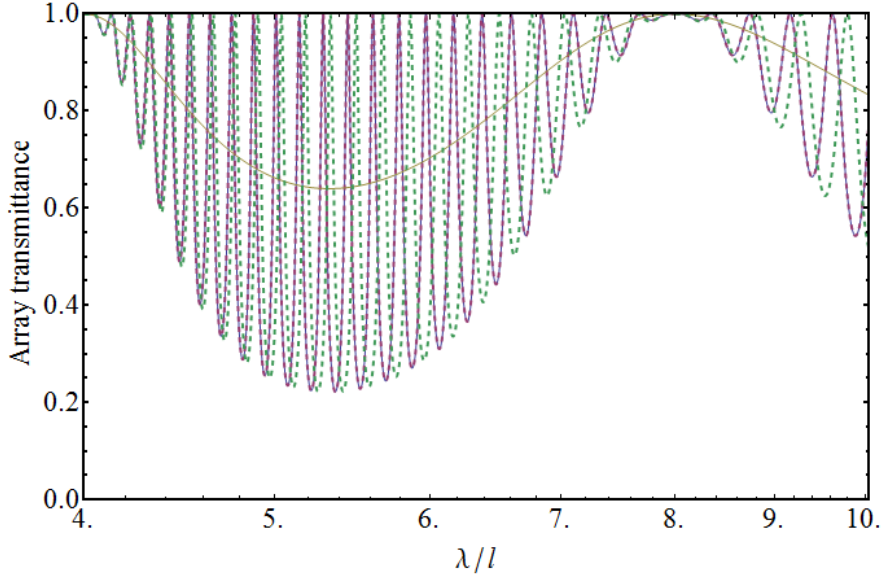


Figure 4.8: The optical transmission spectrum of a two-membrane array with $n = 2$ and $d = 90l$. The full purple curve shows the transmittance (\mathcal{T}) resulting from the full transfer matrix calculations; superimposed on this curve is a dashed purple one that shows the transmittance (\mathcal{T}') from the effective thin-membrane model. For comparison the green curve gives the optical transmission spectrum of the two-membrane array using thin mebrane model with an equivalent ζ . The brown curve shows the single-membrane transmittance ($|t_m|^2$) as a reference.

written as the product

$$M_{\text{tot}}(L) = M_c M_{\text{fs}}(L_-) M_N M_{\text{fs}}(L_+) M_c, \quad (4.18)$$

where L_{\mp} are the lengths of the sub-cavities to the left and the right of the array, respectively. Assuming the field wavelength to be equal to one of the transmissive wavelengths defined previously, it is easy to compute the cavity transmission spectrum as a function of L in order to find the cavity resonances. In order to calculate the optomechanical coupling strength we follow the same method as in Refs. [34, 37]: (i) The cavity resonance frequencies ω are calculated for all membranes at their equilibrium positions, (ii) the j^{th} membrane is then displaced by δx_j , (iii) the corresponding transfer matrix calculated and the shift in the cavity resonances is computed, finally (iv) yielding the individual optomechanical coupling g_j of the j^{th} membrane through the relation $\omega \rightarrow \omega + g_j \delta x_j$. These coupling strengths define the collective motional mode of the membranes which is coupled to the field with a collective coupling constant

$$g_{\text{coll}} = \sqrt{\sum_{j=1}^N g_j^2}. \quad (4.19)$$

As a figure of merit, g_{coll} can be compared to the maximal coupling for a single perfectly reflective membrane, $g = 2(\omega/L)x_{\text{zpm}}$, where x_{zpm} is the extent of the wave-packet of the equivalent quantum harmonic oscillator in its ground state.

4.2.3 Two-membrane array

We consider the case $N = 2$ and assume that the field wavelength corresponds to one of the transmissive wavelengths, as in, e.g., Fig. 4.8. The shifts in the cavity resonance frequencies when one of the membranes is displaced by a small amount can then be calculated analytically in the same fashion as in Ref. [37]. One finds that the displacements of the membranes give rise to two different frequency shifts, which depend on the parity of the cavity mode number. Figure 4.9 shows as an example the real part of the electric field amplitude inside the cavity with the membranes at their equilibrium positions, for the case of two odd and two even cavity modes, and in the case $\lambda > 2nl$ (no internal resonance). Cavity modes come in pairs; for each odd (even) cavity mode where the field amplitude between the membranes is increased as compared to its amplitude in the left and right subcavities, there exists an even (odd) cavity mode where the field amplitude is suppressed. The magnitude of the optomechanical coupling strength mimics the amplitude of the field between the membranes, i.e., it is larger in the case of the former set of modes and smaller in the latter case. In both cases, however, the resonance shifts are opposite for each membrane, which means that $g_1 = -g_2$ and that the field couples to a breathing mode of the two membranes.

4.2.3.1 Thin-membrane model: Optomechanical coupling strength

To derive analytical expressions for the optomechanical couplings at the transmissive wavelengths of a two-membrane array we make use of the thin-membrane model, for which we are able to carry out analytical calculations. In the next section, we will compare the results obtained by replacing the polarizability that appears in the analytical coupling strengths obtained by using the thin-membrane approximation in this section by its general expression, which is valid for arbitrary membrane thickness.

The derivation of the “transmissive” optomechanical couplings in the thin-membrane approximation proceeds along the same steps as in Sec. IIC of Ref. [37] and we only give the main steps here. Within the thin-membrane model the effective polarizability of the array can be shown to be

$$\chi = 2\zeta(\cos \nu - \zeta \sin \nu), \quad (4.20)$$

with $\nu = kd$. The array is transmissive when $\chi = 0$, i.e., when

$$\cos \nu_{\pm} = \frac{\mp \zeta}{\sqrt{1 + \zeta^2}}. \quad (4.21)$$

The cavity resonance frequency shift for displacements δx_1 and δx_2 of membranes 1 and 2, respectively, is

$$\delta\omega = c \left(\frac{\partial k}{\partial \delta x_1} \delta x_1 + \frac{\partial k}{\partial \delta x_2} \delta x_2 \right), \quad (4.22)$$

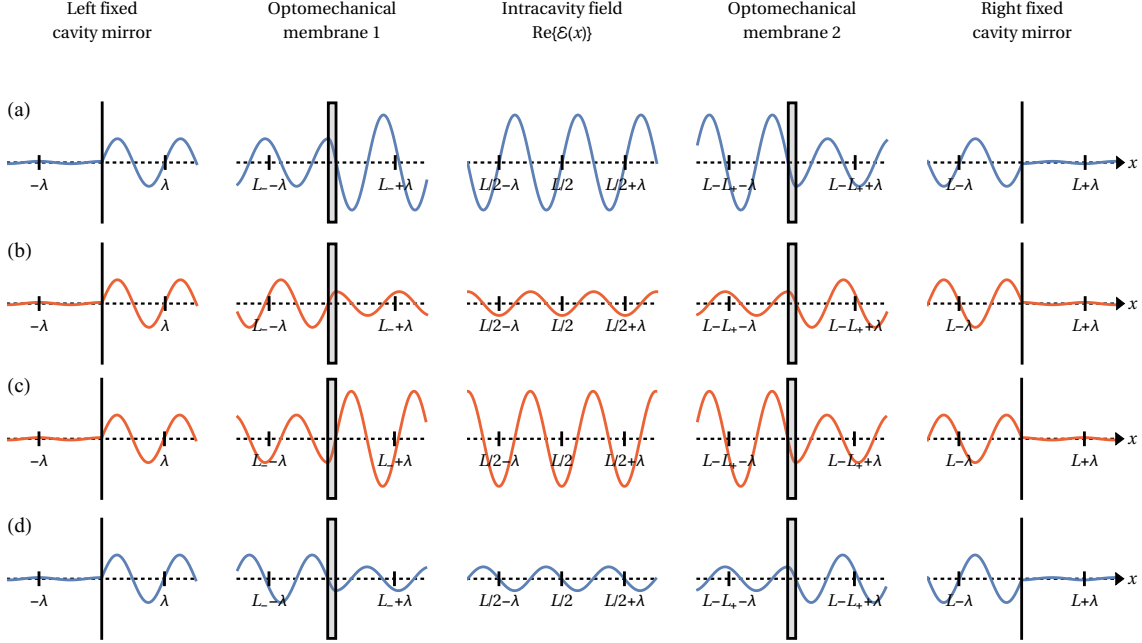


Figure 4.9: Real part of the electric field (in arbitrary units) as a function of position for odd [blue; (a) and (d)] and even [red; (b) and (c)] cavity modes, for transmissive wavelengths larger than nl . From left to right, the five plots are centered around $x = 0$, L_- , $L/2$, $L - L_+$, and L , respectively. The inner membranes have the same characteristics as those considered in Fig. 4.8, and the optical resonator has length $L \simeq 5 \times 10^4 l$ and finesse 3000. The four parts of this plot correspond to the four labelled data points in Fig. 4.10.

where c is the speed of light in vacuum and the partial derivatives are given by Eqs. (27)–(29) of Ref. [37], i.e.,

$$\frac{\partial k}{\partial \delta x_1} = -\frac{\partial k}{\partial \delta x_2} = -\frac{\text{Im}\{\beta - e^{i\nu}\alpha\}}{L + 2d\frac{\partial \chi}{\partial \nu}}, \quad (4.23)$$

with $\alpha = 2ik\zeta^2 e^{-i\nu}$ and $\beta = -2k\zeta(1 - i\zeta)e^{-i\nu}$. Using Eqs. (4.20) and (4.21), one gets that

$$\frac{\partial k}{\partial \delta x_1} = -2k \frac{\zeta(\pm\sqrt{1 + \zeta^2} + \zeta)}{L[1 \pm 4(d/L)\zeta\sqrt{1 + \zeta^2}]}. \quad (4.24)$$

Making further use of the fact that the resonance frequency shift is related to the normalized collective displacement by

$$\delta\omega = g_{\pm} \frac{\delta x_1 - \delta x_2}{\sqrt{2}}, \quad (4.25)$$

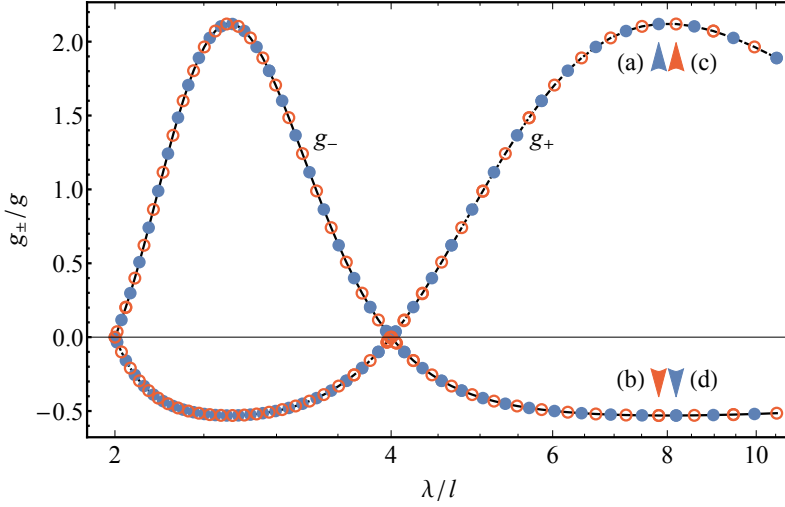


Figure 4.10: Normalized optomechanical couplings g_{\pm}/g , at transmissive wavelengths for the same two-membrane array as used in Fig. 4.8. The array is positioned at the center of an optical resonator with length $5 \times 10^4 l$ and finesse 3 000. The data points show the results of the full transfer matrix calculations (solid blue circles for odd cavity modes, open red circles for even ones), while the curves show the results of the predictions based on the thin-membrane model [Eq. (4.26)]. Four resonances, labelled (a) through to (d), correspond to the respective field patterns shown in Fig. 4.9.

one obtains the collective optomechanical couplings

$$g_{\pm} = g\sqrt{2} \frac{\zeta(\pm\sqrt{1+\zeta^2} + \zeta)}{1 \pm 4(d/L)\zeta\sqrt{1+\zeta^2}}. \quad (4.26)$$

The coupling g_+ is thus found to be identical to the one given by Eq. (38) of Ref. [37], albeit with a different sign convention for ζ . We find g_+ to be larger than g_- when the wavelength is large enough, $\lambda > 2nl$, so that there is no internal resonance for the field inside a single membrane. However, in the region containing the first internal resonance (i.e., $nl < \lambda < 2nl$), g_- becomes larger than g_+ . This can be understood by looking at the evolution of the intracavity field amplitude, as shown in Fig. 4.9 in the case $\lambda > 2nl$. For $\lambda > 2nl$ cavity modes corresponding to g_+ show a greater field build-up between the membranes than the ones corresponding to g_- . The resulting radiation pressure forces and, therefore, the optomechanical coupling strength, are therefore stronger for modes corresponding to g_+ . In contrast, for wavelengths such that $nl < \lambda < 2nl$, because of the change in the sign of ζ , the solution corresponding to cavity modes with a larger field build-up is found to be g_- . As λ/l becomes smaller still, g_+ and g_- alternate in a manner similar to the one just described.

It is interesting to consider the limiting cases for highly reflective membranes. For large $|\zeta|$ and $\lambda > 2nl$,

$$g_+ \sim g \frac{2\sqrt{2}\zeta^2}{1 + 4(d/L)\zeta^2}. \quad (4.27)$$

As noted in Ref. [34] the denominator represents the relative increase in the effective length of the large cavity with length L due to the field build-up in the small cavity, bounded by the membranes, with length d . As long as $4d\zeta^2/L \ll 1$, the effective length of the large cavity is unchanged and the optomechanical coupling strength scales as the finesse of the small cavity, which is proportional to ζ^2 . When the membranes are reflective enough to effectively narrow the large cavity linewidth, the optomechanical coupling saturates and tends to a value proportional to ω/d , determined by the small cavity bounded by the membranes.

In contrast, under the same conditions, we find

$$g_- \sim -\frac{g}{\sqrt{2}} \frac{1}{1 - 4(d/L)\zeta^2}. \quad (4.28)$$

When $4d\zeta^2/L \ll 1$, the radiation pressure force on each membrane is provided by the field in the adjacent subcavity. Although the field amplitude in the shorter subcavities is the same as it would be in the large cavity without membrane array, interference between the two coupled subcavities reduces the optomechanical coupling strength. When the membranes are reflective enough, the reduced field amplitude between the membranes leads to a reduction in the effective cavity length, which in turn results in an effective broadening of the cavity linewidth; this is the opposite situation to the one described in detail in Ref. [37].

4.2.3.2 Full transfer matrix model: Numerical results

To investigate if the predictions of the thin-membrane model hold for realistic membranes with arbitrary thickness we numerically computed these cavity optomechanical coupling strengths at the transmissive wavelengths for the two-membrane array of Fig. 4.8 using the method described above. The length of the cavity is taken to be $L = 5 \times 10^4 l$ and its finesse 3000 as an example. Figure 4.10 shows both optomechanical coupling strengths g_{\pm} , normalized by g , numerically computed at each transmissive wavelength between $2l$ and $10l$. In both cases, the effective thin-membrane model predictions are well-corroborated by the full transfer matrix calculations, which justifies the role of the polarizability as the relevant parameter for characterizing the optomechanical properties of the system. It is interesting that similar optomechanical coupling strengths can be obtained, regardless of whether the membranes are thin or, on the contrary, thick enough for the field to oscillate several times within the dielectric medium, assuming equal effective masses. From Fig. 4.10 it is also clear that, for wavelengths close to an internal resonance, the optomechanical coupling strength vanishes, as there is no field imbalance across the membranes.

In conclusion, the transmission spectra and linear collective cavity optomechanical couplings of a periodic array of flexible membranes have been derived on the basis of full transfer matrix calculations taking into account the thickness of the membranes. The results support the use of the thin-scatterer approximation, provided a suitable phase-shift padding is introduced, and stress the role of the polarizability as the relevant parameter to investigate the optomechanical properties of these arrays.

To estimate the expected optomechanical coupling strength for the previously assembled arrays, we use typical values of $r_m = 0.58$ ($\zeta = 0.71$) at 900 nm, $m \approx 16$ ng, $\omega_m = 800$ kHz, we estimate a zero point motion of $x_{zpm} = 4.9$ fm which gives us the single membrane optomechanical coupling strength $\frac{g}{2\pi} \approx 145$ Hz. Now using equation 4.26 for a two membrane array at a separation distance of $d = 9 \mu\text{m}$ we find $g_+ \approx 2$ g. Thus for a double membrane array at a given transmissive wavelength we would expect a twofold enhancement of the optomechanical coupling strength as compared to the case of a perfectly reflecting single membrane.

Through our theoretical investigations we have established that the optomechanical coupling strength is strongly dependent on the polarizability or equivalently the reflectivity of Si_3N_4 membranes. In the next chapter, we aim to design, develop and fabricate photonic structures on single Si_3N_4 membranes with the aim to achieve 100% reflectivity and hence optimise the collective coupling strengths significantly.

Chapter 5

High reflectivity Si_3N_4 membranes

From chapters 1 and 3 we know that the collective optomechanical coupling strength scales quite favorably with the reflectivity (or equivalently the polarizability) of the membrane. In this chapter, we discuss how we can create a 1D sub-wavelength grating (SWG) on a high-stress Si_3N_4 membrane and enhance their reflectivity. Sub-wavelength gratings (SWG) are a special class of gratings where the grating period (≈ 805 nm) in our case, is less than the wavelength of the incident light (890 - 900 nm). These SWG's have been used in various experiments with wide applications, for example as high reflectors in Vertical cavity surface emitting lasers (VCSEL's) [49][50] and more recently they have also been employed in optomechanical experiments [41][51][26][52]. The motivation in this work is to pattern part of the commercial high stress Si_3N_4 membrane with a SWG to increase its reflectivity, as first demonstrated by J.Lawall's group at NIST Gaithersburg [26][52]. Combined with the array assembly discussed in chapter 2 this may provide a way to significantly enhance the optomechanical coupling strength and lead us towards the single photon strong optomechanical coupling regime. We begin the chapter by introducing the Rigorous Coupled Wave Analysis (RCWA) which is a computational technique used widely to analyse SWG's, in section 5.1. We continue the discussion by describing how we use MIST software (Model Integrated Scattering Tool), in section 5.2, to perform simulations. MIST is a software that has several built-in scattering models including RCWA which we use to investigate the reflectivity of Si_3N_4 gratings. These simulations study the variation of the reflectivity of grating with various grating parameters and we use the results to determine the optimum grating parameters that give high reflectivity in our operating wavelength range. With this information, the gratings are fabricated and characterized as detailed in section 5.3. Following in section 5.5, the gratings are optically characterized by measuring their transmission using a monochromatic light source.

5.1 RCWA theory for rectangular grating

RCWA is an established computational technique used for calculating scattering properties of periodic dielectric structures. We use RCWA to solve for transmitted and reflected diffraction orders from a SWG Si_3N_4 grating.

Consider a rectangular grating geometry as shown in figure 5.1 where the grating period is a , grating width is w , grating line height is h and where the grating material has a refractive index n and is surrounded by air ($n_{air} = 1$). We assume the grating material to have real refractive index and hence neglect absorption. The grating lies in the $x - y$ plane and the grating periodicity is in the x direction where is it considered infinitely periodic.

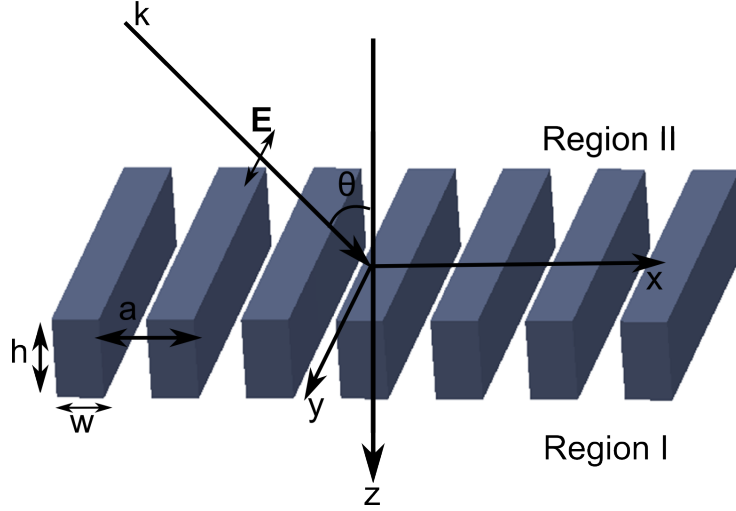


Figure 5.1: Scheme showing a rectangular grating with grating period a , width of grating is $w = f \times a$ and grating height h . Also shown is a TE polarized light propagating in the $x - z$ plane that is incident on the grating at an angle θ with the z -axis. There are three regions to consider first, the region I which is the incident medium separated from the grating by input plane, the grating region, and the region II which is the transmitted medium separated from the grating by an output plane.

For simplicity, consider a linearly polarized Transverse electric (TE) wave incident on the grating at an angle θ with the z -axis, and our aim is to investigate the diffraction from the grating, shown in figure 5.1. There are three regions, the incident medium (region I) separated from the grating medium by the input plane then the grating medium which again is separated from the transmitting medium (region II) by the output plane.

As outlined in reference [53], we expand the relative permittivity in the grating region as a Fourier series

$$\epsilon(x) = \sum_p \exp\left(-i\frac{2\pi p}{a}x\right) \epsilon_p \quad (5.1)$$

where ϵ_p is the p th Fourier component.

For a rectangular grating with air gaps expressing the width of the grating w as a fraction f of the grating period a as $w = f \times a$, then

$$\epsilon_p = (n^2 - n_{air}^2) \frac{\sin(\pi p f)}{\pi p} \quad (5.2)$$

To solve for the reflected or transmitted orders of diffraction, we have to find electromagnetic waves that satisfy Maxwell's equation in the incident (region I), grating and transmitted (region II) medium and match the boundary conditions.

For a TE polarization where the electric field is transverse to the plane of incidence, we express the electric field as,

$$E_y = \exp[ik_0 n (\sin\theta x + \cos\theta z)] \quad (5.3)$$

where $k_0 = \frac{2\pi}{\lambda_0}$ and λ_0 is the wavelength of incident light in air.

The normalized solutions for the electric field in the incident region (region I) and transmitted region (region II) is given by [53]

$$E_I = E_y + \sum_s R_s \exp[i(k_{xs}x - k_{I,zs}z)], \quad (5.4)$$

$$E_{II,y} = \sum_s T_s \exp[i(k_{xs}x - k_{II,zs}(z - h))] \quad (5.5)$$

where k_{xs} is determined from the Floquet condition

$$k_{xs} = k_0 [n_I \sin\theta - s(\lambda_0/a)] \quad (5.6)$$

and $k_{l,zs}$ is given as

$$k_{l,zs} = \begin{cases} k_0 [n_l^2 - (k_{xs}/k_0)^2]^{1/2} & \text{if } k_0 n_l > k_{xs} \\ ik_0 [(k_{xs}/k_0) - n_l^2]^{1/2} & \text{if } k_{xs} > k_0 n_l, \end{cases} \quad (5.7)$$

where $l = I$ for region I and $l = II$ for region II.

In equations 5.4 and 5.5, R_s is the normalized electric field amplitude of the reflected wave in region I and T_s is the normalized electric field amplitude of the transmitted wave in region II.

The magnetic field in region I and region II is obtained by using Maxwell's equation

$$\mathbf{H} = \left(\frac{-i}{\omega\mu} \right) \nabla \times \mathbf{E} \quad (5.8)$$

where μ is the permeability and ω is the angular frequency.

Within the grating region the solutions are modes of a periodic array of dielectric slabs where the tangential electric and magnetic fields are expressed with a Fourier expansion in terms of spatial harmonic fields as

$$E_{gy} = \sum_s S_{ys}(z) \exp(ik_{xs}x) \quad (5.9)$$

$$H_{gx} = i \left(\frac{\epsilon_0}{\mu_0} \right)^{1/2} \sum_s U_{xs}(z) \exp(ik_{xs}x) \quad (5.10)$$

where ϵ_0 is the permittivity of free space and $S_{ys}(z)$ and $U_{xs}(z)$ are the normalized amplitudes of the i th space harmonic fields such that E_{gy} and H_{gx} satisfy Maxwell's equation in the grating.

$$\frac{\partial E_{gy}}{\partial z} = -i\omega\mu_0 H_{gx} \quad (5.11)$$

$$\frac{\partial H_{gx}}{\partial z} = -i\omega\epsilon_0\epsilon(x)E_{gy} + \frac{\partial H_{gz}}{\partial x} \quad (5.12)$$

Substituting equation 5.9 and 5.10 in 5.11 and 5.12 and eliminating H_{gz} we obtain the coupled wave equation as cite??

$$\frac{\partial S_{ys}}{\partial z} = k_0 U_{xs} \quad (5.13)$$

$$\frac{\partial U_{xs}}{\partial z} = \left(\frac{k_{xs}^2}{k_0}\right) S_{yi} - k_0 \sum_r \epsilon_{s-r} S_{yr} \quad (5.14)$$

Equations 5.13 and 5.14 can be expressed in matrix form as

$$\begin{bmatrix} \partial \mathbf{S}_y / \partial(z') \\ \partial \mathbf{U}_x / \partial(z') \end{bmatrix} = \begin{bmatrix} \mathbf{0} & \mathbf{I} \\ \mathbf{A} & \mathbf{0} \end{bmatrix} \begin{bmatrix} \mathbf{S}_y \\ \mathbf{U}_x \end{bmatrix} \quad (5.15)$$

The equation 5.15 is solved for the eigenvalues and eigenvectors of matrix \mathbf{A} and the spacial harmonics of the tangential electric and magnetic fields in the grating are then given by

$$S_{ys}(z) = \sum_{m=1}^n w_{s,m} [c_m^+ \exp(-k_0 q_m z) + c_m^- \exp[k_0 q_m (z - h)]] \quad (5.16)$$

$$U_{xs}(z) = \sum_{m=1}^n v_{s,m} [-c_m^+ \exp(-k_0 q_m z) + c_m^- \exp[k_0 q_m (z - d)]] \quad (5.17)$$

where $w_{s,m}$ and q_m are the elements of the eigenvector matrix \mathbf{W} and the positive square root of the eigenvalues of matrix \mathbf{A} , respectively.

We define, $\mathbf{V} = \mathbf{W}\mathbf{Q}$ where \mathbf{Q} is a diagonal matrix and the elements of \mathbf{V} are given by $v_{s,m} = q_m w_{s,m}$.

The amplitudes of the diffracted fields R_s and T_s and the unknown constants c_m^+ and c_m^- are calculated by matching the tangential electric and magnetic fields at the input and output boundaries.

At the input boundary ($z=0$), we get

$$\begin{bmatrix} \delta_{s0} \\ -in_I \cos\theta \delta_{s0} \end{bmatrix} + \begin{bmatrix} \mathbf{I} \\ i\mathbf{Y}_I \end{bmatrix} [\mathbf{R}] = \begin{bmatrix} \mathbf{W} & \mathbf{W}\mathbf{X} \\ \mathbf{V} & -\mathbf{V}\mathbf{X} \end{bmatrix} \begin{bmatrix} \mathbf{c}^+ \\ \mathbf{c}^- \end{bmatrix} \quad (5.18)$$

and at the output boundary ($z=h$)

$$\begin{bmatrix} \mathbf{WX} & \mathbf{WX} \\ \mathbf{VX} & -\mathbf{V} \end{bmatrix} \begin{bmatrix} \mathbf{c}^+ \\ \mathbf{c}^- \end{bmatrix} = \begin{bmatrix} \mathbf{I} \\ -i\mathbf{Y}_{II} \end{bmatrix} [\mathbf{T}] \quad (5.19)$$

where δ_{s0} is the Kronecker delta function, \mathbf{I} is the identity matrix and \mathbf{X} , \mathbf{Y}_I and \mathbf{Y}_{II} are diagonal matrices with the diagonal elements $\exp(-k_0q_m h)$, $(k_{I,zi}/k_0)$ and $k_{II,zi}/k_0$ respectively.

The two equations 5.18 and 5.19 are numerically solved simultaneously to determine the amplitudes of backward reflected wave R_s and forward transmitted wave T_s .

For a more thorough and detailed analysis of RCWA theory, the reader is referred to [53], [54] and [49].

These results can be understood by considering the grating as a periodic array of waveguides along the x-direction. When a plane wave is incident on the grating then depending on the grating parameters and the wavelength, few waveguide array modes are excited. Now, because of the index contrast and sub-wavelength properties, there exists a wavelength range where only two modes have real propagation constants in the x-direction and carry energy. These two modes travel from input plane ($z = 0$) to grating output plane ($z = h$) and get reflected back. After the propagation of each mode through the grating, it acquires a different phase. Now at the exiting plane, due to the mismatch with exiting plane wave, the waveguide modes get reflected back and also couple to each other. The modes as they propagate and return to the input plane there is a similar mode coupling. If we follow the modes through one round trip, we can obtain the reflectivity solution for the grating. It is possible for the waveguide modes to transmit out to air at both the input and the exiting planes, however for SWG there exists only the 0th order diffraction plane wave that carries energy [55].

To obtain high reflection, the thickness of the SWG should be such that a destructive interference is obtained at the exit plane which cancels transmission. And to obtain a high-quality resonator one has to achieve constructive interference at both the input and exit planes. In this case there is destructive interference at the exit plane not because the fields are zero but because the spatial mode overlap with the transmitted plane wave is 0. Hence, we get a 0 transmission coefficient which prevents optical power from being transferred to the transmissive propagating wave thereby giving complete unity reflection [55].

We conclude by observing that for a SWG, $|R|^2 + |T|^2 = 1$, for the 0th order diffraction, so all the energy that is not transmitted will get reflected back. This is the property that we will use in the design of high reflective SWG Si_3N_4 gratings.

5.2 Grating simulation studies

5.2.1 Introduction to MIST and Grating model

For performing simulations we use MIST (Model Integrated Scattering Tool) which is an optical modelling toolbox developed by Thomas Germer from NIST (National Institute

of Science and Technology). This software is designed to perform integration of the Bidirectional Reflectance Distribution Function (BRDF) over solid angles specified by the user and we use MIST to study the dependence of BRD function with respect to the grating model parameters. These inbuilt models are provided by the SCATMECH library <http://pml.nist.gov/Scatmech/html/grating.htm>.

The BRDF gives the directional dependence of the scattering by a material which in our case is the grating and is defined as [56],

$$f_r(\theta_i, \theta_s, \phi_s) = \lim_{\Omega \rightarrow 0} \frac{\Phi_s}{\Phi_i \Omega \cos(\theta_s)} \quad (5.20)$$

where Φ_s is the power scattered into a solid angle Ω centered on polar angle θ_s and azimuth angle ϕ_s , and Φ_i is the power incident on the sample at an angle θ_i , as shown in figure 5.2.

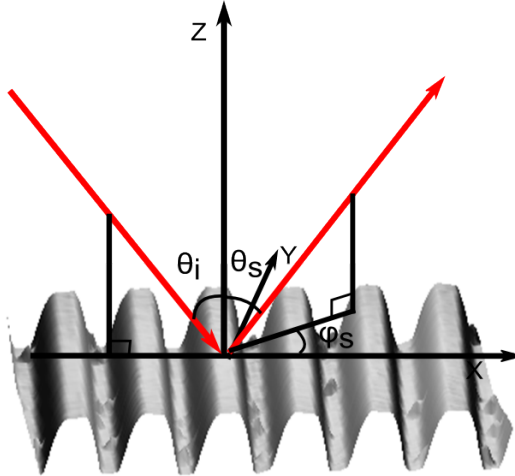


Figure 5.2: Scheme showing a grating and BRDF model defining the parameters where the incident angle is θ_i , the scattered direction of light is given by the polar angle θ_s and the azimuth angle ϕ_s .

The measured reflectance over a finite solid angle for a given optical system is defined as [56]

$$\rho(\Omega) = \int_{\Omega} f_r(\theta_i, \theta_s, \phi_s) \cos(\theta_s) \sin(\theta_s) d\theta_s d\phi_s \quad (5.21)$$

For our simulation studies, we use the RCWA model to calculate the integral in equation 5.21 for the grating geometry.

The grating geometry is defined as rectangular grating with a thin bottom layer of Si_3N_4 film as shown in figure 5.3. A rectangular grating is characterized by its period a , the mean width w_m of the grating lines and the depth of grating lines h . The thickness of

the thin film of Si_3N_4 layer is then the thickness of the membrane t_{mem} minus the grating depth h .

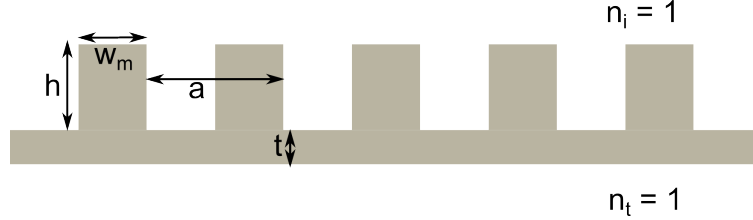


Figure 5.3: Cross sectional scheme showing a rectangular grating with the grating period a , grating mean width w_m , depth of grating lines h and thickness of the underlying Si_3N_4 layer t .

In the MIST software, the user starts by defining the BRDF and grating model parameters. Our Si_3N_4 rectangular grating with a thin film model, derives the motivation from the predefined “Single Line Grating” model in the MIST program albeit with slight modification. To incorporate these changes we use the “Generic grating model” available in the SCATMECH library, where we define our generalized grating geometry and material properties. We summarize below the different parameters that are used in the simulations, some of which we keep fixed throughout the simulation studies.

The parameters used in RCWA BRDF model are defined as :

- $\theta_i = 0^\circ$: Angle of incidence in degrees, which is fixed to be at normal incidence at the grating for all our studies
- inpol : Polarization state of incident light on the grating which is 0 for s (TE) polarized light and 90 for p (TM polarized light)
- grating rotation = 0° : Rotation angle of grating with respect to surface normal. This is fixed to be 0, which means that the incident light is along the fiducial direction of the model. For an isotropic surface, this parameter has no effect.
- diffraction order $n = 0$: Diffraction order of the grating fixed to be 0.
- Minsamples = 10 : Number of integration points for the function integral.
- differential = $(\frac{2\pi}{180})^2$: this is the differential solid angle used during the integration over a $2^\circ \times 2^\circ$ grid.
- type = 0 : BRDF function is evaluated for the reflected light when light is incident from above the grating
- alpha = $\frac{\pi}{180}$: Half angle of the diffraction cone
- order = 25 : The Fourier order considered in the calculation. The dielectric function of the grating material is expanded from -order to +order during calculations.

We use the “Generic grating” model from the SCATMECH library for gratings to define the rectangular grating as shown in figure 5.3 and define the parameters as :

- grating.period (a) : Period of the grating defined as one periodical unit measured from the edge of one groove to the nearest edge of consequent groove.
- grating.medium _{i} = (1,0) : Optical constants of the incident medium expressed as a complex number (n,k), before the grating surface as shown in figure 5.3.
- grating.medium _{t} = (1,0) : Optical constants of the transmitting medium after the grating surface as shown in figure 5.3
- grating.filename = This parameter requires to input a text file with information about the grating medium and define variables such as height of grating lines h , thickness of Si_3N_4 thin film below the grating t , grating mean width w_m as shown in figure 5.3. In this text file, the grating geometry is introduced via defining the vertices and boundaries between the different interfaces using the previously defined parameters (a, w_m, h, t).

Within this parent text file, the grating medium can be passed either as a constant value or as a function file in text format. From ellipsometric characterization of single Si_3N_4 membrane studies as discussed in chapter 2 , we know that the refractive index for the membrane is dependent on wavelength and can be modelled using Cauchy model. For the grating simulation studies we keep the index constant for simplicity, but a wavelength dependent refractive index could also be easily incorporated in the calculations.

- grating.pstring = we input the above mentioned parameters (h, t, w_m) in the sequence in which they are defined in the text file.
- grating.nlayers = 25 : Each curve or line defining a boundary in the grating design is approximated by a staircase function. This number signifies the number of levels to be used in the staircase approximation.

When performing simulations, we vary one grating parameter such as the grating period a , grating mean width w_m , or the grating height h along with the wavelength of the incident light λ , keeping all other parameters constant. In the MIST program, the result is evaluated using the differential function referred as I , which evaluates the reflectance per solid angle in the specified direction, $f_r(\theta_i, \theta_s, \phi_s)\cos(\theta_s)$. For simplicity we keep the detector to be polarization insensitive for all simulations. The final output is then given by $RI = I \times \pi \times \alpha^2$.[\[56\]](#)

5.2.2 Rectangular grating simulation results

We start by describing the simulation results for a rectangular SWG with a geometry shown in figure 5.3. The grating parameters (a, w_m, h, t) are determined using SEM as detailed in section 5.3.2 and 5.3.3 and the refractive index of Si_3N_4 membrane is measured using ellipsometry and white light transmission, presented in section 5.4. We compute the reflectivity of the $0th$ order diffracted light from the grating.

For the grating simulations, we use a constant refractive index of $n = 1.982$ and $k = 0$, independent of wavelength. This value of refractive index n for 200nm thick Si_3N_4 membrane is obtained by averaging the ellipsometrically measured values over a wavelength range of 890 - 940 nm, as detailed in section 2.2.3 in chapter 2.

From the characterization of Si_3N_4 grating on membrane as detailed in section 5.3, we estimate the grating period to be $a = 806$ nm, grating mean width $w_m = 511$ nm, grating height $h = 108$ nm and underlying Si_3N_4 layer thickness $t = 87$ nm.

Using the mean values of a, w_m, h, t as a start for our simulation studies and keeping all other parameters fixed, we investigate the effect of polarization of the incident light on the grating reflectivity.

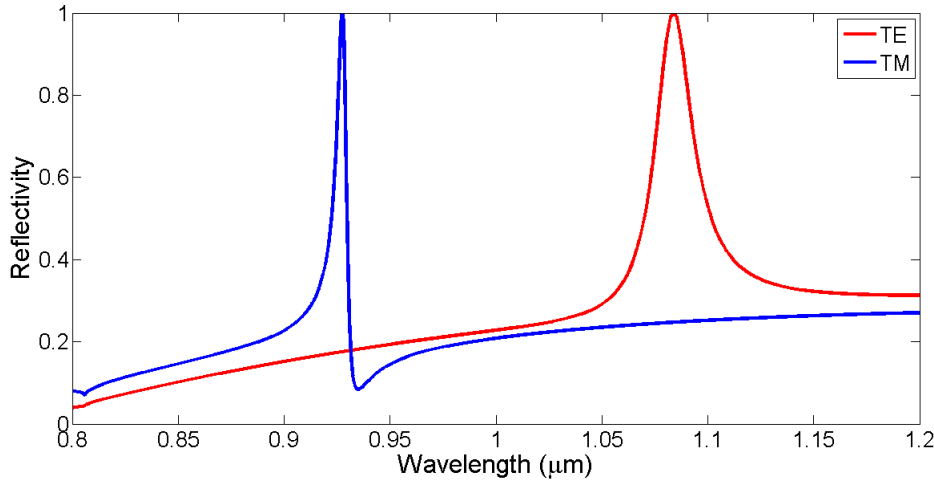


Figure 5.4: Results of simulation for a rectangular Si_3N_4 membrane grating with grating parameters $(a = 806$ nm, $w_m = 511$ nm, $h = 108$ nm, $t = 87$ nm) for TE (red) and TM (blue) polarization of the incident light.

As shown in figure 5.4, we see that for the Transverse electric (TE) polarized light incident on the grating the simulated reflectivity, shown in red, lays flat at about (20%) near the wavelength range of 890-940 nm. For this polarization we get a broad reflection peak at ≈ 1.08 μm with a FWHM ≈ 32 nm.

For the Transverse magnetic (TM) polarized incident light we see that the stimulated reflectivity shows a “Fano resonance peak” around at 927.4 nm where the grating achieves unity reflectivity. The reflectivity peak is narrow with FWHM = 7.2 nm. For the estimated grating parameters (a, w_m, h, t) we get a reflection peak only for the TM polarized incident

light in the operating wavelength range of our laser (890-940 nm). Therefore, from now on we fix the polarization state of the incident light to be TM.

Next, we investigate the effect of varying grating period a and grating mean width w_m on the reflection peak, keeping all other grating parameters fixed.

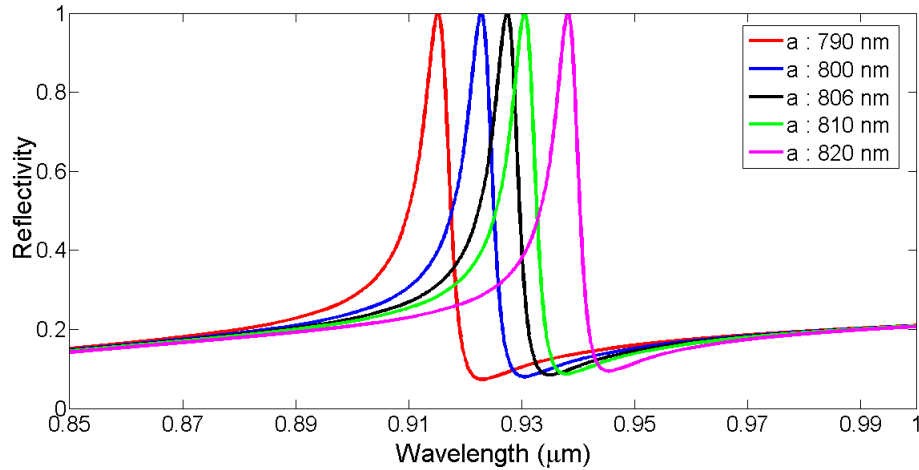


Figure 5.5: Results of simulation for TM polarized incident light on a rectangular Si_3N_4 membrane grating with varying grating period, keeping $w_m = 511$ nm, $h = 108$ nm and $t = 87$ nm fixed

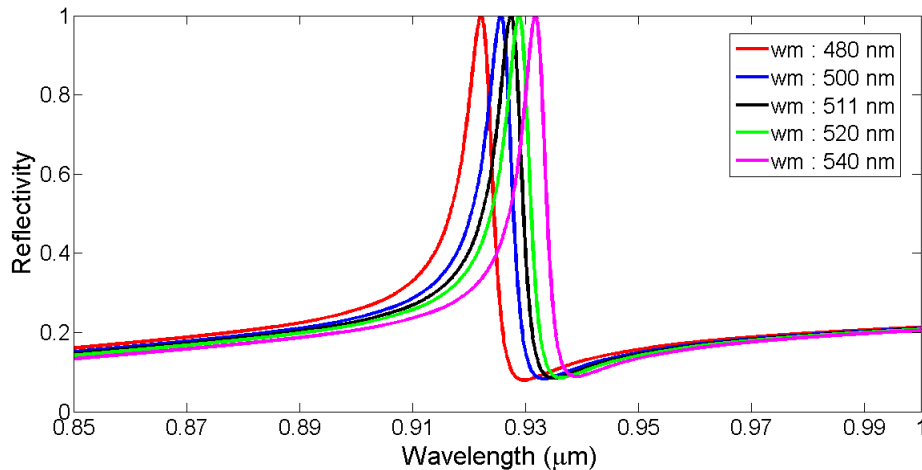


Figure 5.6: Results of simulation for TM polarized incident light on a rectangular Si_3N_4 membrane grating with varying grating mean width, keeping $a = 806$ nm, $h = 108$ nm and $t = 87$ nm fixed.

In figure 5.5, we see a “shift” of the reflectivity peak with the period a of the grating. For

the simulated rectangular Si_3N_4 grating model (fig. 5.3) with TM polarized incident light, we see that the wavelength for the peak reflection shifts towards lower wavelength values by 0.8 nm when the grating period is decreased by 1 nm, indicating a linear correlation.

Figure 5.6 shows a similar trend as observed with grating period, where the reflectivity peak shifts towards lower wavelength with a decrease in grating mean width w_m . Quantitatively, we see that the peak reflectivity wavelength lowers by 0.2 nm for every 1 nm decrease in the grating mean width.

For the grating shown in figure 5.3, it is critical to know what happens to the grating reflectivity when the grating line height h varies. The grating height h and thickness of the underlying film t are related by $h + t = t_{\text{mem}}$, where t_{mem} is the thickness of the Si_3N_4 membrane.

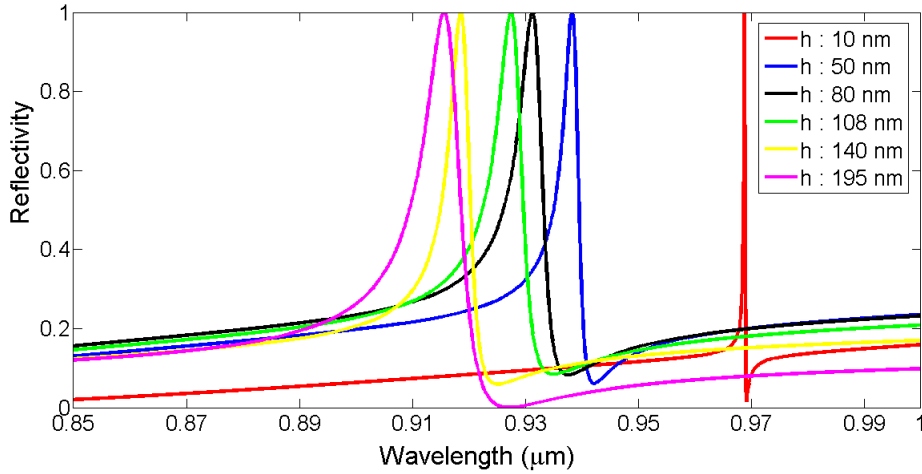


Figure 5.7: Results of simulation for TM polarized incident light on a rectangular Si_3N_4 membrane grating with varying grating line height, keeping $a = 806$ nm and $w_m = 511$ nm fixed.

In fig.5.7, we fix the grating period and grating mean width and see how the grating height affects the peak reflectivity. We observe two trends: first, a shift of the reflectivity peak towards lower wavelength as the grating height increases and second the broadening of the reflectivity peak. The reflectivity peak shifts towards lower wavelength by ≈ 0.3 nm for every 1 nm increase in grating line height. For a grating with no underlying Si_3N_4 layer, that is when $h = t_{\text{mem}}$, the reflectivity peak FWHM ≈ 9.1 nm where as for a grating with a grating line height as low as $h = 10$ nm followed by a Si_3N_4 layer of 185 nm the FWHM is only = 0.3 nm. This implies that, in order to achieve broader reflection peak within a given wavelength range, we should aim to achieve ideal gratings with no remanant Si_3N_4 film below the grating. Why this is a challenging situation to achieve will be addressed in the fabrication section 5.3.1.

From the rectangular grating studies, we conclude that for the Si_3N_4 membrane grating the reflection peak wavelength can be tuned by changing either the grating period, mean width or grating height. For the above discussed Si_3N_4 grating, the reflection peak shifts

towards lower wavelength value when either the period or mean width are decreased or the grating height is increased. Further we note that with a decrease in grating line height and, consequently, an increase in the Si_3N_4 film thickness, there is a narrowing of the reflectivity peak.

As will be discussed in section 5.3, the fabrication of rectangular gratings does not result in straight walls and sharp edges. Instead due to the etching process, the gratings end up having rounded corners and curved walls. In the next section 5.2.3 we discuss the wedged grating which has a trapezoidal shape as shown in figure 5.8.

5.2.3 Wedged grating simulation results

In this section we discuss the effect of having sloped grating walls instead of the idealized straight parallel walls of rectangular gratings. As discussed in the previous section, we use the MIST program with the RCWA model to compute the BRD function for a wedged grating. The new grating geometry is as shown in figure 5.8 which is introduced as a new file in the grating.filename parameter.

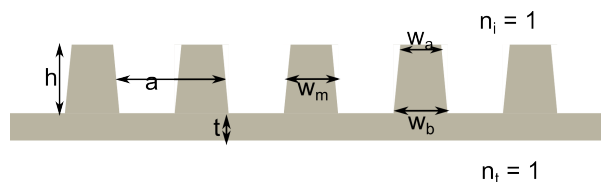


Figure 5.8: Cross sectional scheme showing a wedged grating with the grating period a , grating top width w_a , grating bottom width w_b , grating mean width w_m and depth of grating lines h .

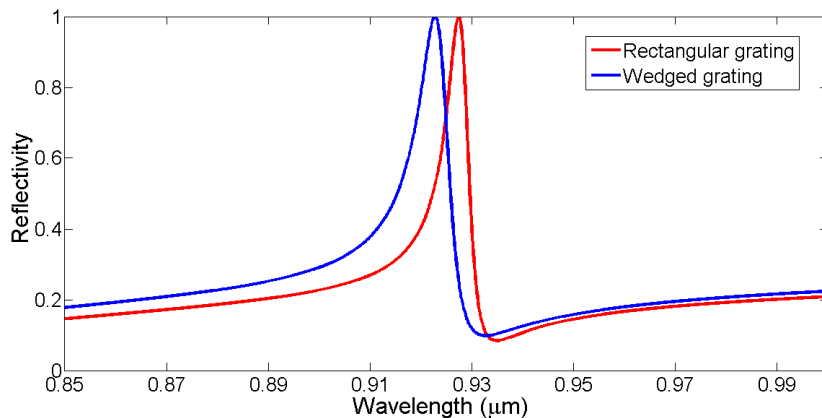


Figure 5.9: Results of simulation for TM polarized incident light on a rectangular Si_3N_4 membrane grating (red) in comparison with wedged Si_3N_4 grating (blue) keeping all parameters fixed.

As shown in figure 5.8, now we have a grating which is characterized by the grating period a , grating top width w_a , grating bottom width w_b , grating height h and thickness of the underlying Si_3N_4 film t . The grating mean width in a wedged grating is defined as $w_m = (w_a + w_b)/2$ and the offset is then defined as $w_m - w_a \equiv w_b - w_m$.

For the simulation studies, we take the mean values of the grating parameters obtained using SEM images as detailed in section 5.3. The grating parameters used for simulation are : grating period $a = 806$ nm, grating mean width $w_m = 511$ nm, offset $w_m - w_a = 117$ nm, grating height $h = 108$ nm and thickness of Si_3N_4 film to be $t = 87$ nm.

With interest to our previous discussion on idealized rectangular gratings now we study how the wedged walls of a Si_3N_4 grating affects the reflection peak. For the simulation studies, we keep the parameters fixed unless otherwise stated.

As shown in figure 5.9, we see the difference between the simulation results in the reflectivity for a rectangular and wedged grating for the same TM polarization keeping all other parameters fixed. We see that the reflection peak for the wedged Si_3N_4 grating has shifted to a lower value by 4.6 nm as compared to the rectangular Si_3N_4 grating and the peak has a broader FWHM of 10.3 nm. In comparison, the FWHM for reflection peak of rectangular grating is $\text{FWHM} = 7.1$ nm.

Simulation studies are done for the wedged Si_3N_4 grating in the same way as for the idealized rectangular grating.

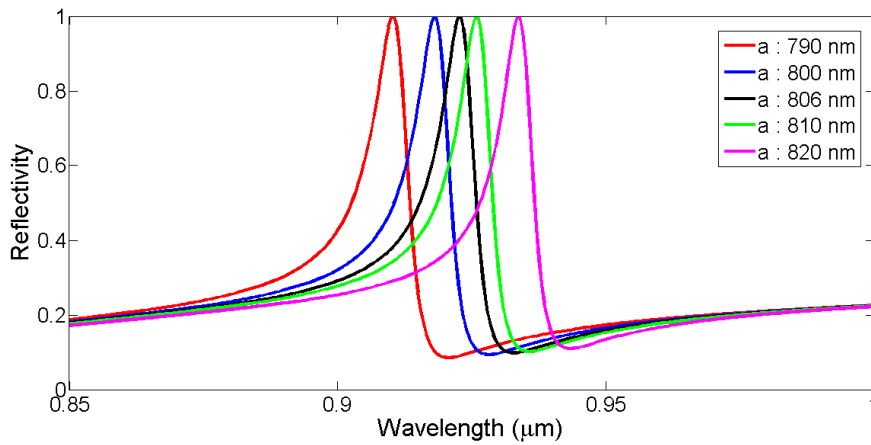


Figure 5.10: Results of simulation for TM polarized incident light on a wedged Si_3N_4 membrane grating with varying grating period keeping $w_m = 511$ nm, offset = 117 nm, $h = 108$ nm and $t = 87$ nm fixed.

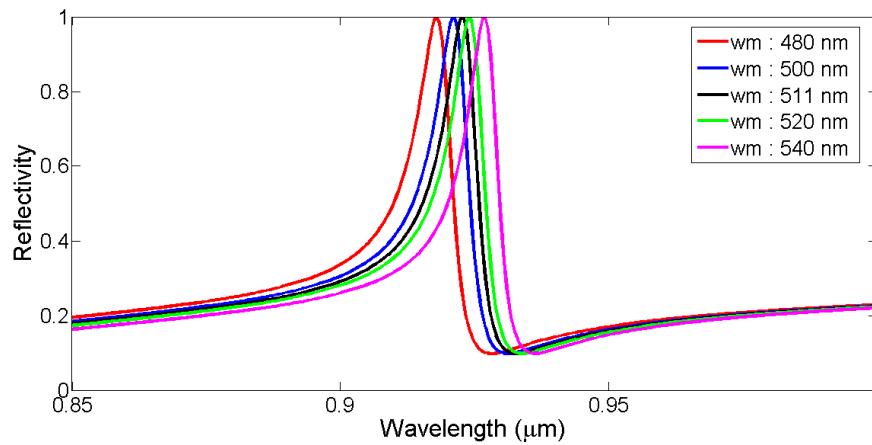


Figure 5.11: Results of simulation for TM polarized incident light on a wedged Si_3N_4 membrane grating with varying grating mean width keeping $a = 806$ nm, offset = 117 nm, $h = 108$ nm and $t = 87$ nm fixed.

Simulation results for a wedged Si_3N_4 grating are shown in figures 5.10 and 5.11 where the grating reflectivity is studied with respect to grating period and grating mean width variation, predict almost exactly the same behaviour as observed for rectangular grating in 5.5 and 5.6, respectively. From these observations we conclude that the wedged nature of our Si_3N_4 grating does not significantly affect the grating reflectivity.

One interesting parameter to play with, in case of the wedged Si_3N_4 grating is the offset. Changing the offset is equivalent to changing the slope of the wedge for the wedged grating.

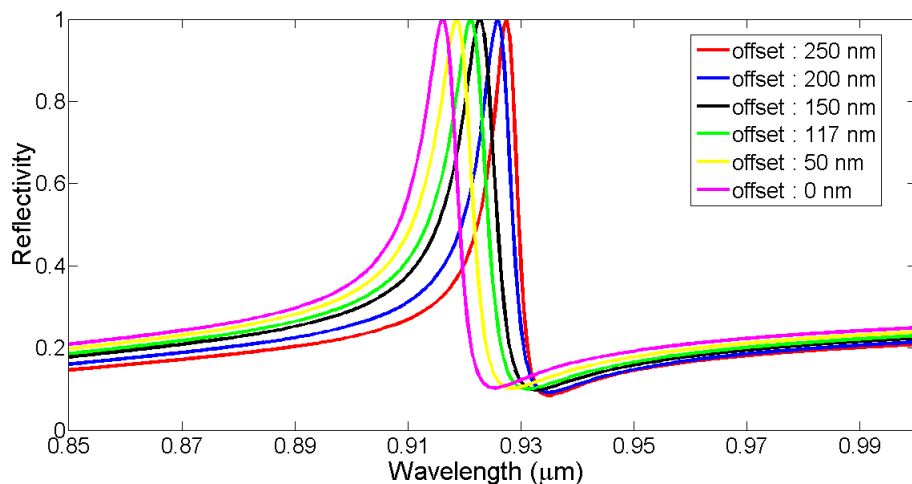


Figure 5.12: Results of simulation for TM polarized incident light on a wedged Si_3N_4 membrane grating with varying offset keeping $a = 806$ nm, $w_m = 511$ nm, $h = 108$ nm and $t = 87$ nm fixed.

From figure 5.12 we see that for increasing the offset by 1 nm, equivalent to increasing the slope results in a shift of the peak reflectivity wavelength towards higher values by 0.05 nm. Also, when the offset is 0 we retrieve the rectangular Si_3N_4 grating simulation result.

Figure 5.13 shows simulation results for variation of grating reflectivity with grating line height h . From figure 5.13, we observe similar variation of grating reflectivity as a function of grating line height as previously observed in rectangular grating simulation studies, with reference to figure 5.7.

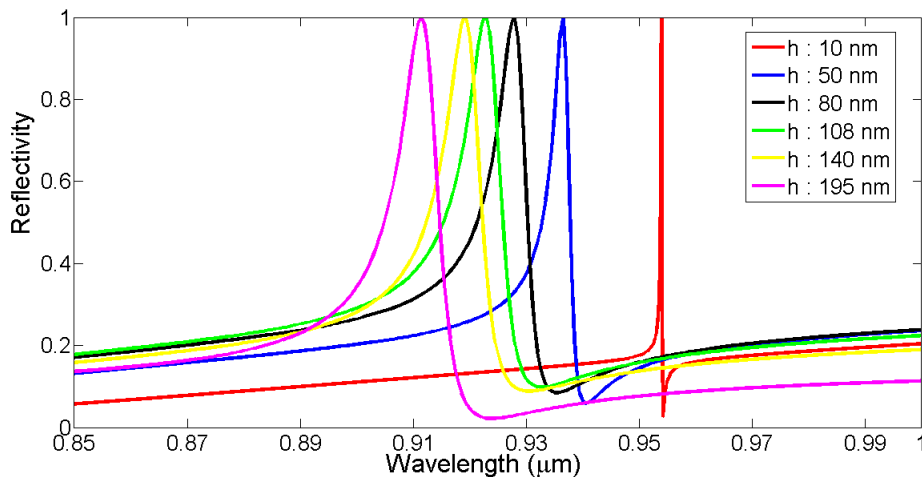


Figure 5.13: Results of simulation for TM polarized incident light on a wedged Si_3N_4 membrane grating with varying grating line height keeping $a = 806$ nm and $w_m = 511$ nm fixed.

In conclusion we have discussed the simulation results of rectangular and wedged Si_3N_4 gratings obtained using MIST software and we observe that the grating simulation studies predict similar behaviour for both types of gratings. This leads us to believe that sloped grating walls do not reduce the grating reflectivity efficiency rather it only shifts the peak reflectivity wavelength for the given TM polarization.

5.3 Fabrication and characterization of sub wavelength grating (SWG) on high stress Si_3N_4 membranes

In the previous sections we discussed how to use MIST program to perform simulations to study the efficiency of grating reflectivity as a function of wavelength when different grating parameters are varied. Next, in section 5.3.1 we discuss the fabrication process to create the sub wavelength gratings (SWG's) on high stress Si_3N_4 membranes. Followed by section 5.3.2, where we discuss the determination of grating parameters such as grating period a and grating mean width w_m using Secondary Electron Microscopy (SEM). Further to extract more exact information and characterize the grating profile, we devise a new technique in which we use Focussed Ion Beam (FIB) to cut a gold sandwiched Si_3N_4 grating layer and use SEM to provide us with the transverse grating profile, which will be discussed in section 5.3.3.

5.3.1 Fabrication of gratings on high stress Si_3N_4 membranes

To fabricate a sub wavelength grating on Si_3N_4 membranes, we draw our inspiration from the work conducted in Lawall group [52][26]. With reference to [52][26], it is described how to design, develop and fabricate SWG's on low stress Si_3N_4 membranes. We extend the work to high stress Si_3N_4 membranes with the motivation to realize highly reflective membranes with high frequencies and mechanical quality factor.

The fabrication of gratings on a Si_3N_4 membrane follows the flow chart shown in figure 5.14. We use a 200 nm thick, 500 nm square high stress Si_3N_4 membranes on a 200 μm thick, $5 \times 5 \text{mm}^2$ Si frame provided by NORCADA. The entire grating fabrication process is carried out in the cleanroom facility at iNano center, Århus University. The various steps are :

- Membrane cleaning : We start by taking a clean, dust free 200 nm thick Si_3N_4 membrane. The membrane is further cleaned in an etching machine using O_2 plasma to remove carbon contaminants from the membrane surface. For the cleaning recipe, we use O_2 plasma with an O_2 flow rate of 50 sccm for a duration of 3 mins . The activity of the cleaning process depends on the RF set power is 50 W and pressure set point is 100 mtorr.
- Gluing chip to carrier wafer : To perform spin coating on the Si_3N_4 membrane, we glue the cleaned membrane chip ($5 \times 5 \text{mm}^2$) on a cleaned Si substrate ($1 \times 1 \text{cm}^2$). To do this, we use a “Crystal bond glue”, which melts at a temperature of 65°C . We heat the glue using a hot plate and then put a small drop of this glue near the center of the carrier wafer and carefully place the membrane chip on the carrier wafer with the aim to glue one chip corner to the carrier wafer.
- Spin coating of PMMA : For spin coating we use a solution of 9% of 950 molecular weight PMMA. PMMA is the standard electron positive resist used for most Electron Beam Lithography (EBL) processes. Positive electron resists when exposed to an electron beam break the intermolecular bonds and hence the exposed region becomes

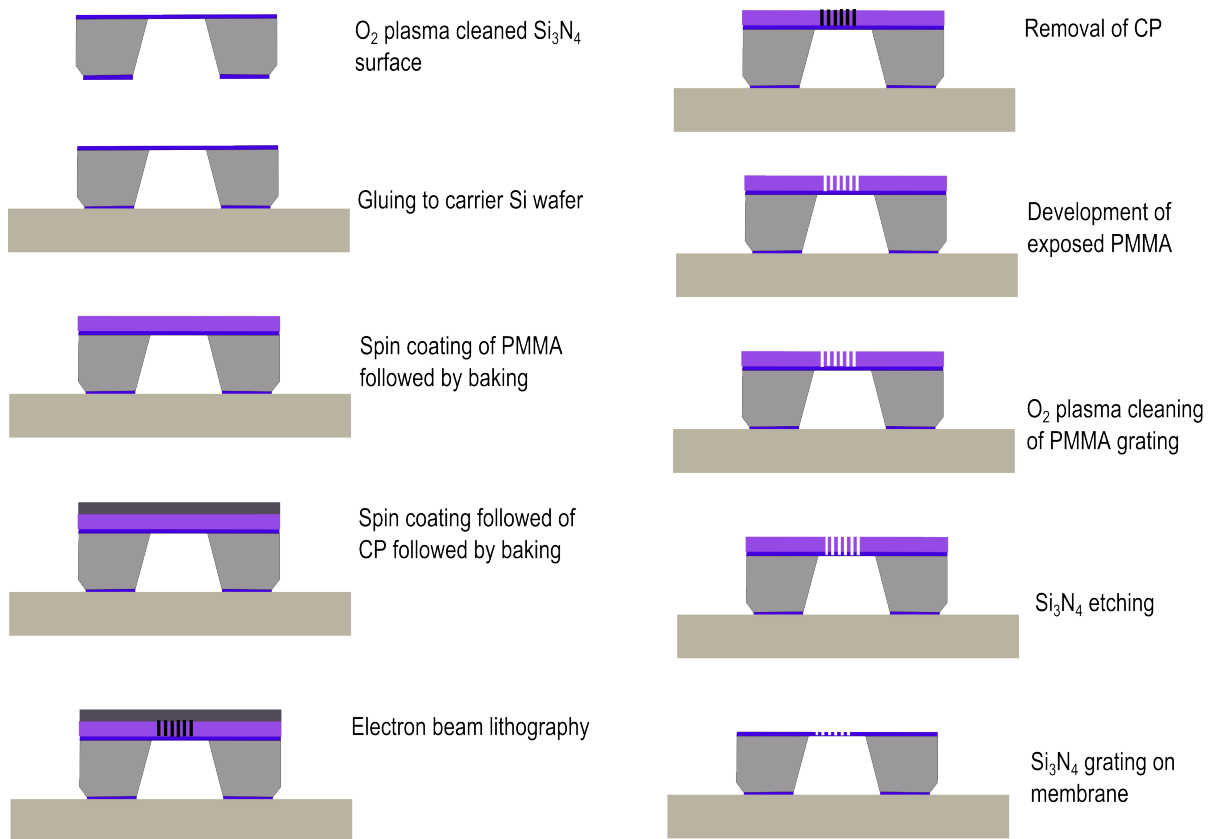


Figure 5.14: Fabrication process for Si_3N_4 grating on membrane surface

dissolvable in a developer solution thereby creating the desired pattern on the PMMA layer. To make the 9% PMMA solution we mixed 4g of 11% 950 PMMA with 1g of anisole to get approx 5g of 9% 950 PMMA solution. We use two drops of the 9% PMMA solution for spin coating. The spin coating parameters used are : speed = 4000 rpm, acceleration = 2000 rpm/s and time = 60s.

- **Baking of PMMA** : After the spin coating of PMMA, we have to perform baking. This is done by immediately placing the PMMA coated membrane chip on a preheated hot plate at a set temperature of 180°C for 2 mins.
- **Resist thickness measurement** : We can either use profilometer or ellipsometer to make a quick determination of the coated PMMA resist thickness. It is important to know the resist thickness before resist development and etching of Si_3N_4 membrane, as this helps us to avoid underdevelopment of resist and possible etching failures. For profilometer measurements we make a small scratch on the PMMA surface near one of the edges and use the step edge to determine the resist thickness. For ellipsometer measurements, we build a model with layers of PMMA, Si_3N_4 , and Si layer followed by a quick measurement in the UV-vis range, then fit the model to the measured

results and extract the resist thickness (measurement process described in detail in section 1.2.3 chapter 2). For a given concentration of PMMA solution and fixed spin coating parameters the resist thickness remains the same.

- Spin coating conductive polymer (CP) : Next, we coat the PMMA surface on the membrane chip with conductive polymer (SX-AR-PC 5000/90.2) to avoid charging effects during Electron Beam Lithography (EBL). Spin coating parameters for the conductive polymer are : speed = 2000 rpm, acceleration = 2000 rpm/s and time = 60s.
- Baking conductive polymer : Following the spin coating we perform baking of the conductive polymer. The CP and PMMA coated carrier wafer with membrane chip is immediately placed on a pre-heated hot plate at 90°C for 2 mins.
- Electron Beam Lithography (EBL) : The PMMA and CP coated wafer with membrane chip is placed on a standard EBL holder with a faraday cup. We use the FEI SEM (Magellan 30) to perform the EBL process and expose the PMMA layer to create a grating pattern. This is a standard SEM machine with inbuilt capability to perform EBL. A SEM machine consist of an electron gun which emits thermionic electrons when heated, these electrons are focussed using electrostatic and magnetic lenses to form a well defined and focussed beam of electrons which are then accelerated towards the sample surface. The secondary electrons formed as a result of interaction of the incident electrons with the sample surface is captured by an Everhart-Thornley Detector (ETD) which then provides the sample surface image. There can also be backscattered electrons from the sample surface which are then captured in the Through-Lens-Detector (TLD) which provides a higher resolution image of the sample surface. SEM characterization will be discussed in section 5.3.2.

For performing EBL, we use the incident electrons to expose the PMMA layer and break the molecular structure of the PMMA molecules thereby creating a well defined exposed region. By selective exposure on the PMMA surface we create the desired PMMA grating pattern. Before the start of EBL, we perform the usual adjustments of the SEM for example checking the stigmatism of the electron beam, focussing, measuring electron beam current, etc, as discussed in the EBL instruction manual (provided by iNano). For EBL processes, we use a beam current of 2 nA at an acceleration voltage of 30 keV. For the EBL design we use the “ELPHY Quantum software”. The design of PMMA grating has lines defined by a thickness of 460 nm and a period of 800 nm for an area size of $(50 \times 50 \mu m^2)$. The dose factor for EBL writing is an important factor which affects the thickness of PMMA grating lines formed after development. After a couple of trials, we fixed the dose factor to be 2.4, which gave us the desired result without under or over development of the PMMA resist.

- Development of the exposed resist : After EBL, the next step is to develop the exposed PMMA resist in a developer solution of 3:7 H_2O : IPA(Iso-propyl alcohol). Before this, we first remove the conductive polymer layer by immersing the wafer

carrying membrane chip in deionized water for ≈ 2 mins. Followed by N_2 blow drying. After the surface is thoroughly cleaned, we immerse the exposed PMMA resist in the developer solution for exactly 1 min. Next, the development is stopped immediately by immersing the sample in IPA for 30 secs, followed by careful N_2 blow drying. Development is one of the crucial steps in the fabrication process in which the development time, developer solution and temperature play an important role in creating fully developed resist patterns. The dose factor fixed for EBL also affects the PMMA grating features, primarily the grating mean width and grating line height of the PMMA grating.

- **Cleaning PMMA grating :** At this point, we have a PMMA grating on the PMMA layer. To have a clean and fully developed PMMA grating without irregularities, which will affect the subsequent Si_3N_4 grating, we perform a PMMA plasma cleaning. This process is aimed to clean the walls of the PMMA grating and any left over thin layer of PMMA after development on the Si_3N_4 membrane surface. We use a O_2 plasma cleaning recipe with an O_2 flow rate of 100 sccm with RF set power of 50 W for a duration of 21 sec.
- **Gluing the carrier wafer to a Si inch wafer :** After cleaning of the PMMA grating, the carrier wafer is glued to a bigger 6 inch Si carrier wafer using the crystal bond glue. This is done in preparation for Si_3N_4 membrane etching process to create a holder for the etching machine.
- **Si_3N_4 membrane etching :** This is the most important step in the fabrication process where one etches through the valleys of PMMA grating to create a Si_3N_4 grating on the membrane surface. We use the “STS Pegasus” etching machine for this process and before the etching we first clean the machine chamber by initiating a recommended 10 min O_2 plasma clean using a predefined recipe. Then followed by a test run of the Si_3N_4 etching recipe on a dummy wafer. The Si_3N_4 etching process is then performed on the Si_3N_4 membrane chip for a time period of 170 secs. This Si_3N_4 etching recipe uses C_4F_8 at a flow rate of 59 sccm and SF_6 at a flow rate 36 sccm. The set 13.56 MHz RF coil power is 800 W and 13.56 MHz platen power is 40 W and the substrate temperature is 20°C .
- **Removal of PMMA :** After Si_3N_4 membrane etching, remove the PMMA from the Si_3N_4 membrane chip by immersing it in acetone for ≈ 2 mins followed by rinsing with IPA and N_2 blow drying. The Si_3N_4 grating surface is checked under an optical microscope and if the surface is not very clean, the cleaning process is repeated.
- **Cleaning of Si_3N_4 grating :** This is final cleaning of Si_3N_4 grating. For this we use Pegasus again and use a predefined O_2 cleaning recipe which uses O_2 flow rate of 100 sccm, a set 13.56 MHz RF coil power of 800 W and 13.56 MHz platen power at 40 W, and substrate temperature of 20°C .
- **Afer the cleaning, we have the Si_3N_4 grating on the membrane.**

We make a preliminary examination of the Si_3N_4 grating surface with a high magnification optical microscope, followed by more precise determination of grating parameters such as grating period a , grating mean width w_m , grating profile and height h using Secondary electron microscopy (SEM) and other techniques as will be discussed in the next sections 5.3.2 and 5.3.3. Figure 5.15 shows a grating on the Si_3N_4 membrane surface which will be discussed in following sections.

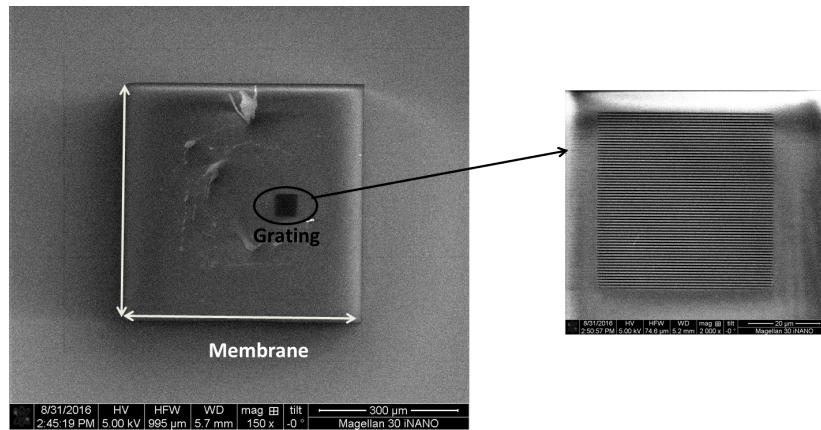


Figure 5.15: SEM image showing the grating on Si_3N_4 membrane. The SEM and optical characterization of this grating will be discussed in section 5.3.2 and 5.5

One of the major challenges faced in the the fabrication of grating on high stress Si_3N_4 membranes was to sucessfully etch the grating pattern on the Si_3N_4 membrane surface using the reactive etching process. This consisted in several iterations of development and etching routines to find the right parameters needed to create the grating pattern on Si_3N_4 membranes.

5.3.2 Characterization of grating-on-membrane parameters using SEM images

In the previous section, we have detailed how to design and fabricate gratings on Si_3N_4 membranes. In order to determine the grating parameters such as grating period a and grating mean width w_m experimentally, we make use of SEM to capture top view images of the grating. However, top view SEM images of the grating don't provide information about the grating line height h or the grating profile, for which we have developed an original method to determine these parameters which will be discussed in section 5.3.3.

First, we investigate the grating parameters (a, w) of a grating that will again be studied in section 5.3.3.

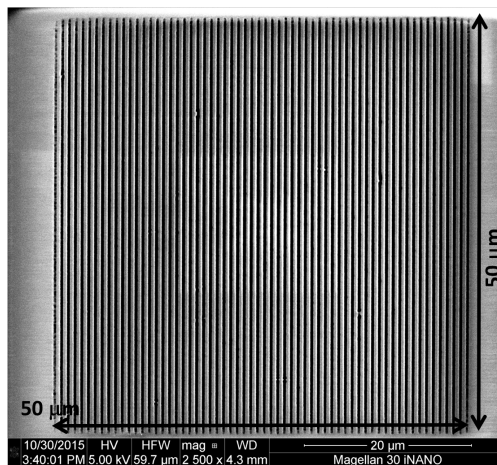


Figure 5.16: 2D SEM image showing the grating on Si_3N_4 membrane. This is a top view image taken at a magnification of $2500\times$ with a beam current of 50 pA and a voltage of 5 kV . The grating area is $50 \times 50\ \mu\text{m}^2$.

Figure 5.16 shows a 2D SEM picture of a grating on a Si_3N_4 membrane. This image is captured using ETD detector which provides the surface image of a sample using the scattered secondary electrons. The image is taken at a magnification of $2500\times$ with a beam current of 50 pA and a voltage of 5 kV . The grating area is $50 \times 50\ \mu\text{m}^2$ and we clearly see the equidistant grating lines with clean and well defined grating walls.

To extract quantitative information from the SEM images of the grating, we use an inbuilt scale in the SEM software to measure the grating period a and width w as seen from the top. One such image at a magnification of $25000\times$ is shown in figure 5.17.

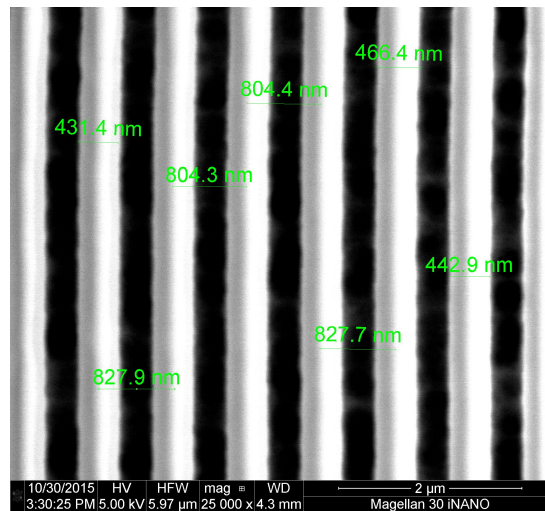


Figure 5.17: 2D SEM image showing the same grating as in figure 5.16 at a magnification of $25000\times$ with a beam current of 50 pA and a voltage of 5kV. Grating period and mean width measurements at various grating locations are shown in green.

Using the SEM measured values in image 5.17, we extract a grating period of 816.1 ± 13.5 nm and a grating width 446.9 ± 17.8 nm. To be more exact in extracting the grating parameters we use a software, “Image J” on the image shown in fig. 5.17. After calibrating the image with a scale, the grating parameters are measured visually. We estimate the grating period $a = 813.7 \pm 6.3$ nm and mean width $w = 454.4 \pm 12.1$ nm. Clearly, the estimated values of grating period and width from the two different methods of determination on the same image 5.17 are in agreement within the error bars.

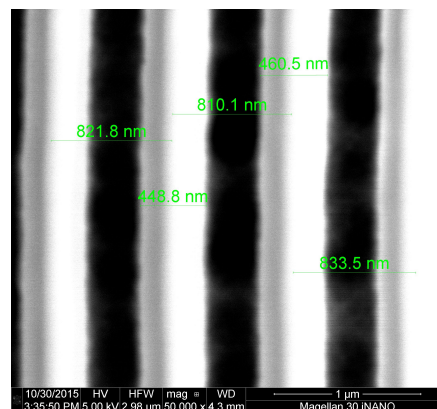


Figure 5.18: 2D SEM image showing the same grating as in figure 5.16 and 5.17 at a higher magnification of $50000\times$. The measurements of grating period a and grating mean width w_m are shown in green.

A higher magnification image of the same grating is shown in figure 5.18. Through this

image we observe that the grating edges are not that sharp or clean and there seems to be some interconnections between the grating lines. To investigate further we proceed in the next section 5.3.3 with a destructive method to analyse the same grating and estimate the grating parameters with better accuracy and to ascertain the grating profile. This image also confirms that the SEM measured period and width are in the range within the predicted measurement results of image 5.17.

5.3.3 Characterization of grating-on-membrane parameters using Focussed ion beam (FIB) cut of the grating followed by SEM

The SEM top view images of the grating can provide us with information only about the grating period a and meanwidth w_m . In order to further extract the grating profile and height of grating lines h we need to look at the grating with a cross sectional view or use an AFM. Since the gratings are fragile we cannot use AFM for such a measurement, as any contact with the grating or the membrane will break the membrane easily. And with SEM, it is not possible to have a cross sectional view of the grating even with tilt. To resolve this issue, we devised a new technique where we cut a part out of the grating using FIB and then look at the cut in the grating with a SEM.

Before the FIB cut, the Si_3N_4 grating is made more robust by sandwiching the grating between two gold layers. As shown in scheme 5.19, the front side of the Si_3N_4 grating-membrane is coated with ≈ 50 nm of Au and the back side with ≈ 200 nm of Au via thermal deposition.

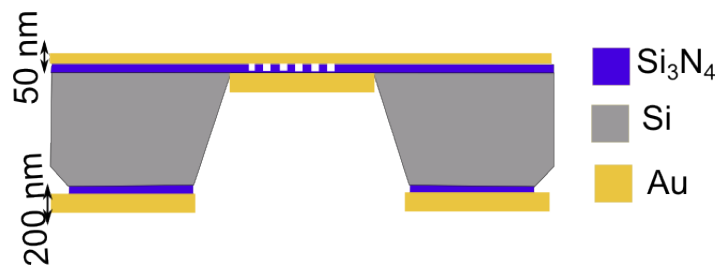


Figure 5.19: Scheme showing the Si_3N_4 grating sandwiched between two Au layers in preparation for FIB cut. Thickness of the top Au layer is ≈ 50 nm and thickness of the bottom Au layer is ≈ 200 nm.

The FIB cutting of the sandwiched Si_3N_4 grating is performed in the FEI Versa machine. The Versa machine is a dual beam system which incorporates both SEM and FIB imaging capabilities. FIB as the name suggests uses ions usually Ga^+ ions instead of electrons for imaging of samples. When we use highly energetic Ga^+ ions, the ion beam can impact the sample surface destructively and create holes in the sample. FIB process creates holes in the sample surface by removing the material via sputtering.

Figure 5.20 represents a scheme for dual beam FIB-SEM instrument, which shows a perpendicular electron beam to the sample surface where as the Ga^+ ion beam is directed

at an angle of 52° . Before the FIB cutting process the grating is further protected by depositing a thick $\approx 2 \mu\text{m}$ carbon layer over an area where the FIB cutting is performed, as shown in figure 5.21.

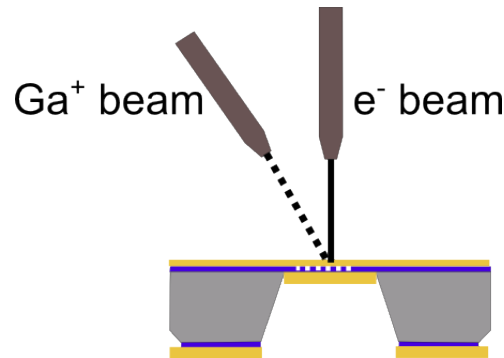


Figure 5.20: Scheme showing the dual beam FIB - SEM system. For the cutting of sandwiched Si_3N_4 grating we use the Ga^+ beam and for in-situ imaging e^- beam.

To perform FIB cutting, the sample is tilted to an angle of 52° to be normal to the Ga^+ ion beam. Parameters used for the FIB process are beam current = 30 pA, voltage = 30 kV and targeted etching distance $\approx 2.5 \mu\text{m}$. The result of the FIB cutting is shown in figure 5.21, where cuts are done at three different locations.

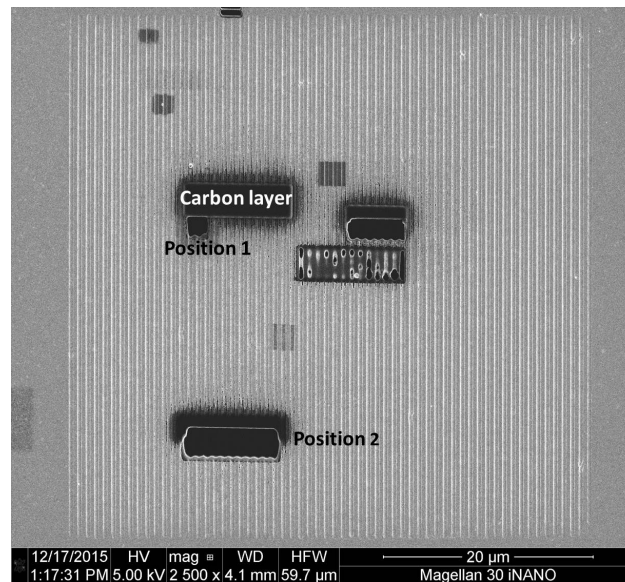


Figure 5.21: 2D SEM image showing the same grating as in figure 5.16, 5.17 and 5.18 which is now Au coated and cut at several locations using FIB. For identification the cut locations are marked as position 1 and 2. The cross sectional view of these cut locations is shown in figure 5.22 and 5.23

Figure 5.21 shows the SEM top view of the sample surface with FIB cuts at various positions. The cross sectional view of these positions is captured using SEM and shown in figure 5.22 for position 1, figure 5.23 for position 2. With these images we see that the grating profile is not rectangular. Instead the grating walls are smoothly curved and the corners are rounded. Also, we see that the grating is not going through the membrane as there is an underlying layer of Si_3N_4 . This is why we introduced and studied the grating with a thin Si_3N_4 layer and wedged walls instead of the usual rectangular grating using MIST simulation.

Analyzing these images using “ImageJ”, we find the period of the grating to be $a = 805.9 \pm 9.5$ nm, grating topwidth $w_a = 395.0 \pm 13.6$ nm, grating bottomwidth $w_b = 628.3 \pm 15.1$ nm which gives grating meanwidth $w_m = 511.7 \pm 10.2$ with an offset of 116.7 ± 17.0 . The thickness of grating lines $h = 108.5 \pm 7.8$ nm and the thickness of the underlying Si_3N_4 layer $t = 86.7 \pm 6.7$ nm.

The grating period a and mean width w_m estimated using top view SEM images is in agreement with the values obtained using cross sectional FIB cut SEM images of the same grating. However, for all simulation studies we use the mean values of grating parameters determined using the cross sectional cut of the grating, since the values estimated using top view SEM images are not considered decisive as these images are dependent on the image saturation and contrast.

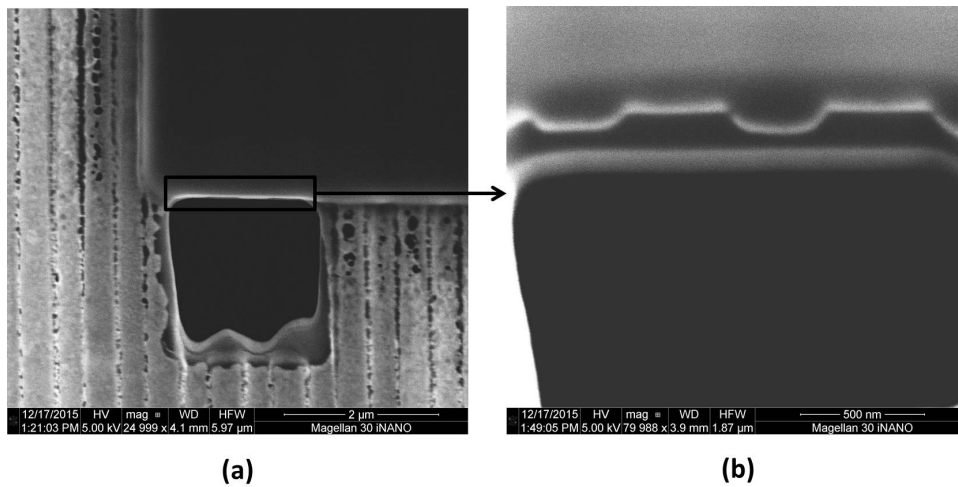


Figure 5.22: 2D SEM image showing the cut part of the position 1 of grating shown in figure 5.21 where (a) shows the image in top view without any tilt of the sample and (b) shows the cross sectional view at a tilt angle of 45° . In the cross sectional view, Si_3N_4 grating profile is clearly visible with the bright top and bottom layer of Au. The image (a) is taken at a magnification of $25000\times$ and (b) at a magnification of $80000\times$ with a beam current of 50 pA and a voltage of 5 kV.

In figure 5.22 and 5.23 along with the grating profile, we also see the bright top and bottom layer of Au. The bright top layer of Au which is about 50 nm thick aids us in

visualizing the grating profile with better clarity.

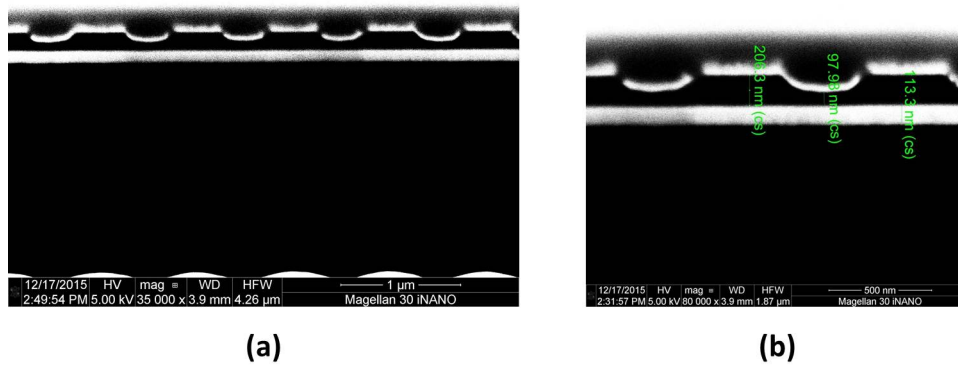


Figure 5.23: 2D SEM image showing the cross sectional view of the cut part of the position 2 of grating shown in figure 5.21 at a tilt angle of 45° where (a) shows an image obtained at magnification of $35000\times$ and (b) an image taken at magnification of $80000\times$. The grating profile is clearly visible together with the bright top and bottom layer of Au. For the images we use a beam current of 50 pA and a voltage of 5 kV.

5.4 Characterization of Si_3N_4 membranes

In the previous section we have modelled, fabricated and characterized the gratings on Si_3N_4 membranes. One of the most critical parameters to consider in the design of gratings is the refractive index n of the Si_3N_4 membranes. From the simulations, we see that for a rectangular Si_3N_4 grating with grating parameters ($a = 806$ nm, $w_m = 511$ nm, $h = 108$ nm, $t = 87$ nm) even an 1% change in refractive index n shifts the reflectivity peak by 1.4 nm, thereby affecting the grating modelling parameters (a, w_m, h, t) designed to achieve peak reflectivity in a given range. In the next sections we discuss two different methods to determine the refractive index and thickness of Si_3N_4 membranes.

5.4.1 Ellipsometric characterization of Si_3N_4 membrane

Ellipsometric characterization of single Si_3N_4 membrane gives us the refractive index n which is an important parameter for the design of Si_3N_4 gratings. The ellipsometric measurement is carried out as outlined in section of chapter 2 for two 200 nm thick Si_3N_4 membrane chips and the results of the measurements are shown in figure 5.24.

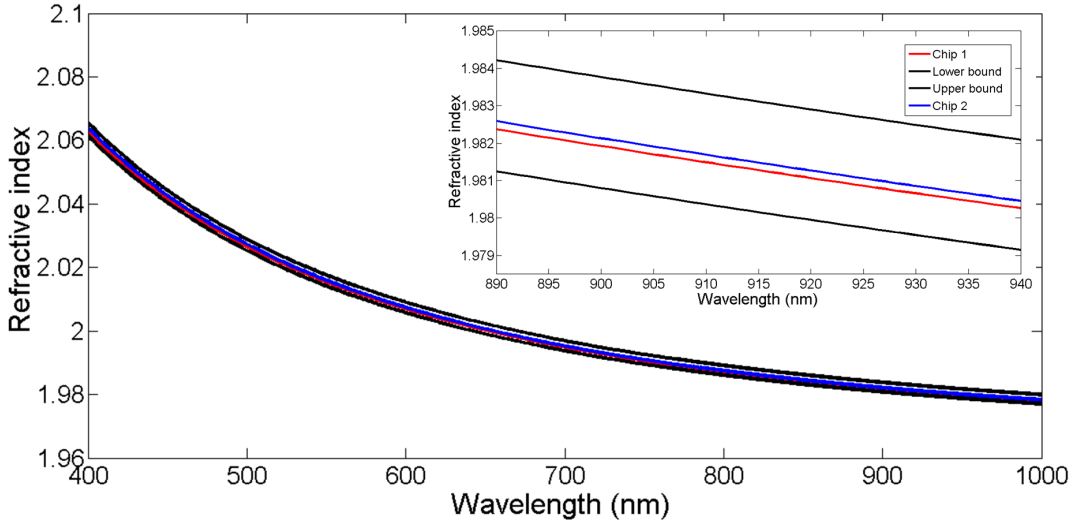


Figure 5.24: Results of ellipsometric measurements on two 200 nm thick Si_3N_4 membrane chips where the inset shows the zoom on the wavelength range of interest.

The refractive index is determined by fitting the measurement results to the Cauchy model and extracting the Cauchy coefficients, n_0 and n_1 . From the fit, for the first chip we extract the Cauchy coefficients to be $n_0 = 1.962 \pm 0.001$, $n_1 = 162.5 \pm 1.3$ and thickness of membrane $t_{mem} = 203.5 \pm 0.2$ nm and for the second chip we get $n_0 = 1.962 \pm 0.001$, $n_1 = 161.3 \pm 0.6$ and $t_{mem} = 205.0 \pm 0.1$ nm.

From figure 5.24, we see that the refractive index is wavelength dependent, however the index variation is less than 1% over the wavelength range of interest i.e 890 - 940 nm (shown in inset of figure 5.24). Hence, we approximate the refractive index as a constant value over the specified wavelength range and estimate average $n = 1.982 \pm 0.001$ for chip 1 and $n = 1.981 \pm 0.001$ for chip 2. Thus, for the 200 nm Si_3N_4 batch of membranes we estimate an average refractive index of $n = 1.981 \pm 0.001$ and the average thickness to be $t_{mem} = 204.3 \pm 1.1$ nm. For all grating simulation studies we used a approximate refractive index of $n = 1.982$.

To compare the obtained values of refractive index n and thickness of membranes t_{mem} with ellipsometry and check the accuracy of the method, we perform a white light transmission measurement of the 200 nm thick membranes under broadband illumination as described in section 5.4.2.

5.4.2 Transmission of single Si_3N_4 membrane measured under broadband illumination

In this section, we use broadband white light illumination to measure the transmission of single 200 nm thick Si_3N_4 membranes used for fabrication of gratings. From section chapter 3 we know that the transmission of thick membranes, thick when $n \times t_{mem}$ is of the same order as the wavelength of incident light λ , shows internal resonances due to

interference effects within the dielectric medium. For a 200 nm thick Si_3N_4 membrane we find the internal resonances to occur at 400 nm and 800 nm wavelength of incident light as seen in figure 5.25, where $n \times t_{mem}$ is an integral multiple of $\frac{\lambda}{2}$.

We use the same setup as discussed in section 2.4 of chapter 2, to measure transmission of double membrane arrays.

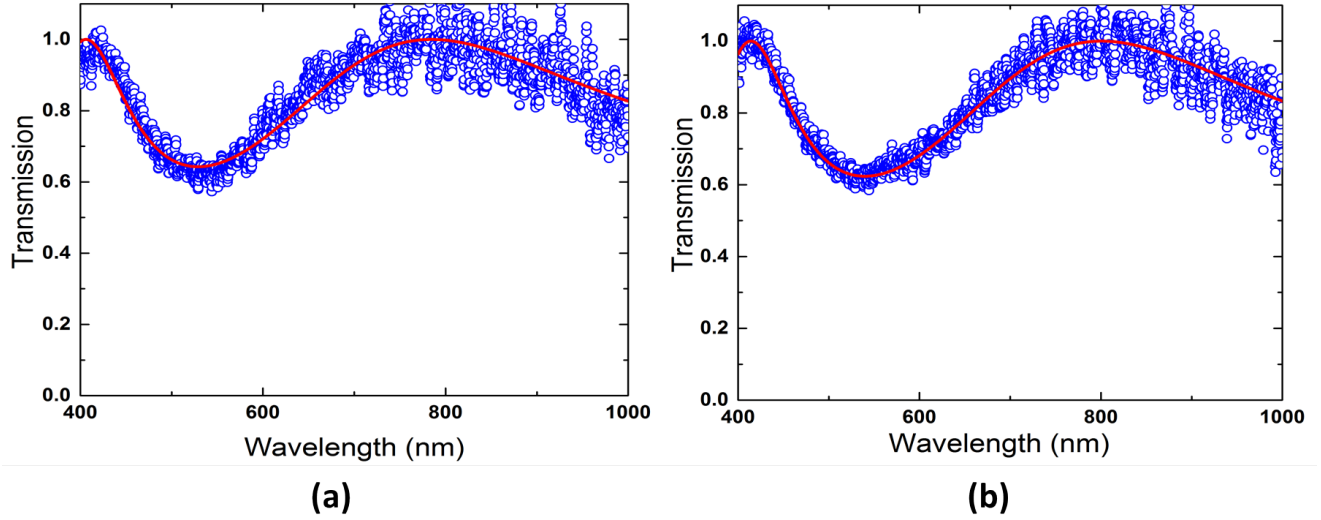


Figure 5.25: Results of white light transmission measurements on two 200 nm thick Si_3N_4 membrane chips where graph (a) shows the first membrane-chip and (b) shows the second membrane-chip. Data points are shown in blue open circles and the thick membrane transmission fit to the data points is shown in red.

The transmission spectra for the two membranes is then fitted using the transmission expression given for a thick membrane

$$T = 1 - \frac{1}{1 + \frac{4n^2}{((n^2-1)\sin((2\pi nt_{mem})/\lambda))^2}} \quad (5.22)$$

To fit the white light measurements we use an effective refractive index $n_{eff} = E[n_0 + \frac{n_1 \times 100}{\lambda^2}]$ where λ is the wavelength in nm, n_0, n_1 are the Cauchy coefficients obtained from ellipsometry, E is a parameter that is extracted from the fit which gives the relative deviation in the index as measured from ellipsometry and t is the thickness obtained from the fit. The measurement result and the fit for the measurement is shown in figure 5.25 where the fit gives the membrane thickness for the first membrane-chip to be $t_{mem} = 199.9 \pm 0.9$ nm and the constant fit parameter $E = 0.983 \pm 0.002$ which gives the effective refractive index $n_{eff}(\lambda = 900 \text{ nm}) \approx 1.952$. Similarly, figure 5.25(b) shows the measurement result and fit for the second membrane-chip and we find the thickness of the membrane $t_{mem} = 198.9 \pm 0.4$ nm and constant parameter $E = 1.005 \pm 0.002$ which gives the effective refractive index $n_{eff}(\lambda = 900 \text{ nm}) \approx 1.999$.

In comparison, for the same two membrane-chips using ellipsometry we obtain, $t_{mem} = 204.58 \pm 0.09$ nm and refractive index $n(\lambda = 900 \text{ nm}) = 1.990 \pm 0.002$ for first membrane-chip and $t_{mem} = 203.2 \pm 1.1$ nm and refractive index $n = 1.997 \pm 0.009$ for second membrane-chip. This suggests that the refractive index n and thickness t obtained using the white light transmission measurement is relatively close to the value obtained using ellipsometry for the same membrane-chips. To be more exact in our calculations we could impose a wavelength-dependent refractive index variation and extract Cauchy coefficients (n_0, n_1) from the white light transmission measurement which will provide a better estimation of refractive index. Also, we note that within the same batch there could be slight variations in the refractive index n due to inhomogeneity in the fabrication.

5.5 Optical characterization of grating on Si_3N_4 membrane

In this section we describe how we measure the transmission of Si_3N_4 grating and compare the result with the simulated model. For the transmission measurements we use the grating-membrane shown in SEM images 5.27.

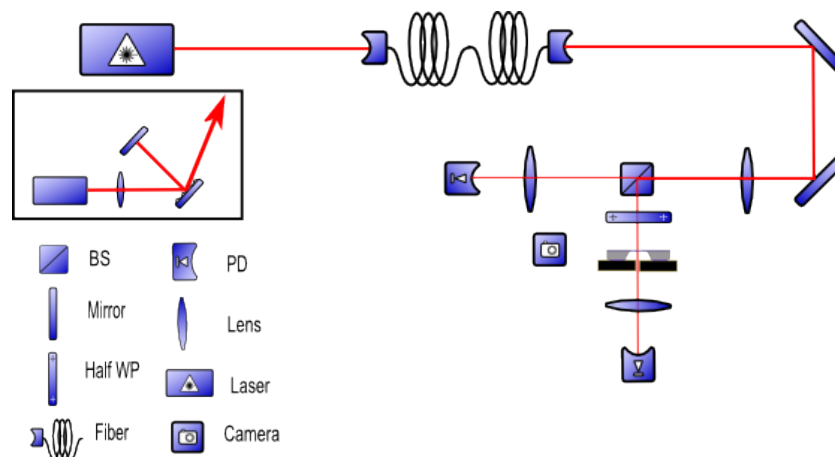


Figure 5.26: Transmission measurement scheme for Si_3N_4 grating on a membrane. This setup is similar to the monochromatic light transmission setup used for membrane arrays in chapter 2, except now a half wave plate (achromatic Thorlabs) is inserted before the grating to vary incident polarization and a CMOS camera to precisely position the grating.

Figure 5.26 shows the setup for the optical characterization of the gratings. In this setup, we only measure the transmission of gratings.

The Laser beam coming from Sacher Lion TEC 520 laser is coupled to a polarization maintaining optical fiber and sent to the grating characterization setup. The output beam from the fiber is directed to a 50/50 beam splitter and split into two beams. The first beam acts as the reference beam and is sent to a photodiode detector, detector 1 (Thorlabs 36 DET A/M). The second beam is focussed using a doublet 60 mm lens to get a spot size of $\approx 28 \mu\text{m}$ at the membrane. The beam goes through a half wave plate and through the

grating holder that has a $500\ \mu\text{m}$ hole at the center, to a photodiode detector 2 (Thorlabs 36 DET A/M). For precise positioning and alignment of the grating-membrane chip we use a CMOS camera (DCC 1545M) placed close to the grating holder such that it captures the scattered light from the membrane surface.

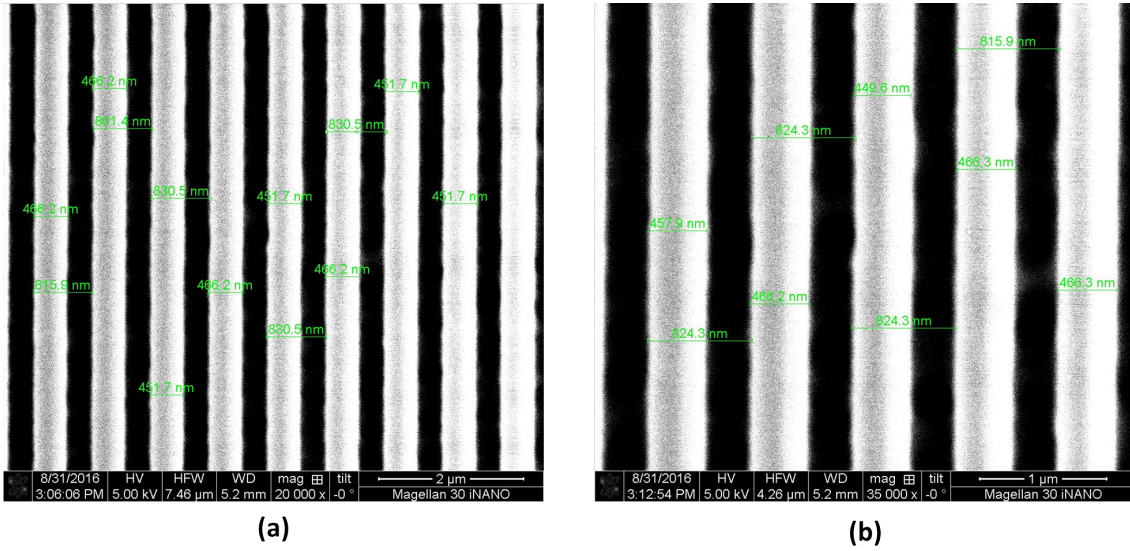


Figure 5.27: 2D SEM image showing the Si_3N_4 grating which is optically characterized in this section. (a) shows the image at a magnification of and (b) at a magnification taken using a beam current of 50 pA and voltage of 5 kV.

Figure 5.27 shows the SEM images of a Si_3N_4 grating is used for transmission measurement in this section. The images are shown in figure 5.27(a) at a magnification of $25000\times$ and 5.27(b) at a magnification of $35000\times$ taken with a beam current of 50 pA and voltage 5 kV. From the images we estimate an average grating period $a = 807.8 \pm 17.3\ \text{nm}$ and grating width $w = 462 \pm 12\ \text{nm}$ for image 5.27(a) and $a = 801.8 \pm 5.9\ \text{nm}$ and $w = 466.3 \pm 4.9\ \text{nm}$ for image 5.27(b). The grating period and width obtained using the two SEM images with different magnifications are within error bar precision.

The transmission measurements for the grating use the same procedure as described in section 2.5 of chapter 2. The difference from previous procedure being that now we have to precisely position the grating using the camera and have the laser beam go through the grating. After the grating is translated and aligned to have the laser beam incident on it, we test the polarization effects of the grating initially with a camera and the half wave plate. As shown in figure 5.29, we clearly see the reflective diffraction pattern from the grating. For monochromatic light incident at a wavelength of 902.3 nm we see different orders of reflected diffraction beam with the 0th order being the most intense.

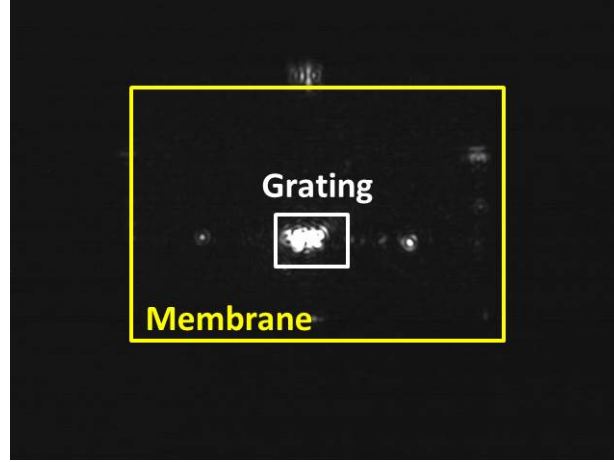


Figure 5.28: Camera image showing the grating diffraction pattern at the maximum transmission point.

The transmission through the grating is scanned for the whole wavelength range of the laser (890 - 940 nm), first for the polarization resulting in minimum transmission through the grating and then for the polarization resulting in maximum transmission. To normalize the measured intensities we also take scans without the grating at each of the orthogonal polarizations (TE or TM). For each wavelength λ_i , the power measured by each detector is recored for 0.1 ms, over the desired wavelength range. Without the grating in place the ratio of the intensities gives the normalization factor $N(\lambda_i)$ defined by

$$N(\lambda_i)_{TE/TM} = \left[\frac{I2_{\text{without}}(\lambda_i)}{I1_{\text{without}}(\lambda_i)} \right]_{TE/TM} \quad (5.23)$$

where λ_i is discrete wavelenegth for each step i , $I2_{\text{without}}(\lambda_i)$ is the mean intensity measured in detector 2 and $I1_{\text{without}}(\lambda_i)$ is mean intensity measured in detector 1, without the grating for the two orthogonal polarizations.

The measurement can then be repeated with the grating for the two orthogonal polarizations (TE and TM) where the sample transmission is given by

$$T(\lambda_i)_{TE/TM} = \left[N(\lambda_i) \frac{I2_{\text{with}}(\lambda_i)}{I1_{\text{with}}(\lambda_i)} \right]_{TE/TM} \quad (5.24)$$

where λ_i is discrete wavelenegth for each step i , $I2_{\text{with}}(\lambda_i)$ is the mean intensity measured in detector 2 and $I1_{\text{with}}(\lambda_i)$ is mean intensity measured in detector 1, with the grating for the two orthogonal polarizations.

We also take measurement scans on a region outside of the grating area that is on the membrane, to see if the transmission still remains the same as expected for a 200 nm Si_3N_4 membrane for the two orthogonal polarizations. These results are summarized in figure 5.29.

We draw several observations from the figure 5.29. First, see the Si_3N_4 membrane transmission for the two orthogonal polarizations and as expected the transmission measured is independent of polarization. Fitting the data points to theory we extract a membrane thickness of $t_{mem} = 203.1 \pm 9.4$ and a refractive index of $n = 1.98 \pm 0.12$.

More interestingly, we see a clear signature of grating effect as the grating transmission goes down to 30.4% at a incident wavelength of 934.8 nm for one of the polarization where as the other orthogonal polarization retains a constant value of $\approx 80\%$ over the entire scanned wavelength range.

These results are then compared with what would be an expected theoretical model simulated using MIST software. For the simulation we use approximate values of grating period $a = 806$ nm and grating mean width $w_m = 530$ nm obtained from SEM images for this grating (figures 5.27). Then we adjust the height h and the thickness t of the underlying Si_3N_4 layer to obtain transmission variation similar to the experimentally measured transmission for the two orthogonal polarizations. These results are compared with what would be an expected theoretical model, where we use grating parameters of $a = 806$ nm, $w_m = 530$ nm, $h = 60$ nm, $t = 135$ nm, offset = 117 nm and a refractive index $n = 1.982$ for both polarizations.

The green lines are not a fit to the data instead they are simulated transmission variation for a Si_3N_4 grating-on-membrane with assumed grating parameters ($a = 806$ nm, $w_m = 530$ nm, $h = 60$ nm, $t = 135$ nm, offset = 117 nm and a refractive index $n = 1.982$ for both TE and TM polarizations). To fit the measured data and extract grating parameters, we need more advanced tools such as Finite-Difference-Time-Domain software packages and modelling tools.

Also, we observe that the we don't achieve optimum 100% grating reflectivity as predicted by grating simulations. One of the possible reasons, could be because of the grating line height h being significantly lower than expected in the simulations. This could be a result of not sufficiently etching through the Si_3N_4 membrane layer due to either underdevelopment of PMMA grating or incomplete etching of Si_3N_4 membrane during fabrication process. Or else the decrease in expected reflection efficiency could also be due to absorption losses, since the grating might have some left over PMMA or dirt material on the surface which degrades the optical properties.

Controlling the fabrication process and parameters is the utmost important aspect for creation of gratings with repeatable results. Any inconsistencies or deviation that is observed in the grating properties arise from changes in the fabrication procedure.

In conclusion in this chapter, we have summarized how to design, fabricate, and characterize Si_3N_4 grating-on-membrane systems. We have successfully fabricated and optically characterized a Si_3N_4 grating-on-membrane. With the transmission measurements done using a monochromatic light source on this Si_3N_4 grating-on-membrane system we have seen the expected signatures for SWG characteristics. This Si_3N_4 grating-on-membrane system gives us a peak reflectivity of $\approx 70\%$ at a wavelength of 934.8 nm. In the future, we plan to optimise the fabrication grating parameters to create efficient gratings with peak reflectivity in our operating wavelength range and to design and fabricate arrays of Si_3N_4 grating-on-membrane systems for collective optomechanical systems.

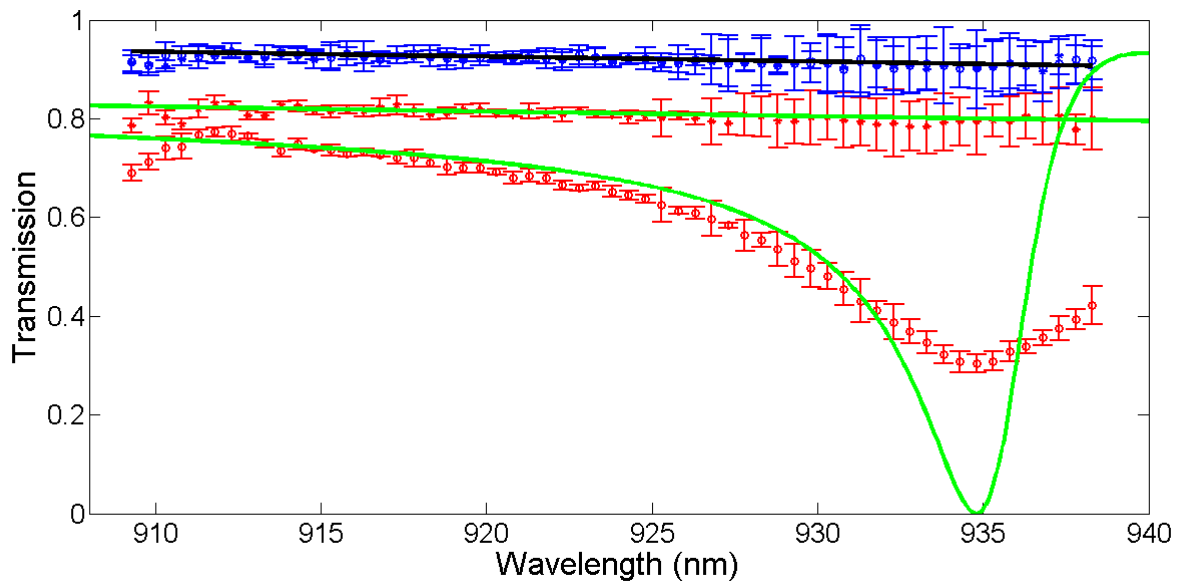


Figure 5.29: Result of transmission measurement on a Si_3N_4 grating-on-membrane using a monochromatic light source. The red data points are measurement results on the Si_3N_4 grating which ‘*’ for TE polarization and ‘o’ for TM polarization. The green line represents simulated transmission for a wedged Si_3N_4 grating with grating parameters ($a = 806$ nm, $w_m = 530$ nm, $h = 60$ nm, $t = 135$ nm, offset = 117 nm and a refractive index $n = 1.982$ for both TE and TM polarizations. The blue ‘*’ data points are transmission measurement results of the Si_3N_4 membrane for TE polarization and blue ‘o’ data points are transmission measurement results of Si_3N_4 membrane for TM polarization and the black line is the fit to the data.)

Chapter 6

Hybrid cavity mechanics with doped systems

In the previous chapter we discussed the design and fabrication of 1D photonic structures in order to enhance the membrane reflectivity. In this chapter, we take a different approach and theoretically look into the dynamics of a mechanical resonator with embedded dopants that can interact with an optical field. Such an optomechanical system which allows interaction between different mechanical, electromagnetic and atomic degrees of freedom is commonly referred to as hybrid optomechanical systems.

Hybrid cavity optomechanics is an emerging field within cavity optomechanics which involves hybrid setups. The main motivation for hybrid setups is to functionalize or interface mechanical resonators with embedded dopants that act as few-level systems and thereby increase the possibilities for interacting with electromagnetic radiation.

Hybrid optomechanical setups present an interesting interface and can be applied in metrology, sensing and telecommunication applications. Various hybrid interfaces have been studied, in which single atoms or molecules [57–62], cold atomic ensembles [32, 63–75], quantum dots [76–78], NV centers [79–83], defects [84], artificial superconducting atoms [85–87], crystals [88] can interact with movable mirrors, membranes, cantilevers, nanobeams, etc.

A prototypical hybrid optomechanical system, as considered e.g. in [58, 62, 65, 67], consists in a single optical mode coupled, on the one hand, to a single mechanical mode via radiation pressure and, on the other hand, to a single (or ensemble of) two-level system (TLS). The interaction of a TLS with the field of the optical resonator indirectly modifies the optomechanical response of the mechanics, which may allow for enhanced optomechanical cooling, coherent atom-photon-phonon interactions or the generation of multipartite nonclassical states.

We propose here an alternative hybrid optomechanics approach in which an ensemble of TLS which interacts with an optical cavity field is embedded directly into a macroscopic mechanical resonator. We show that the TLS effectively mediate interactions between the cavity field and the mechanics, which may result, for instance, in efficient cooling of the mechanics to the ground state, even in the unresolved sideband regime where standard

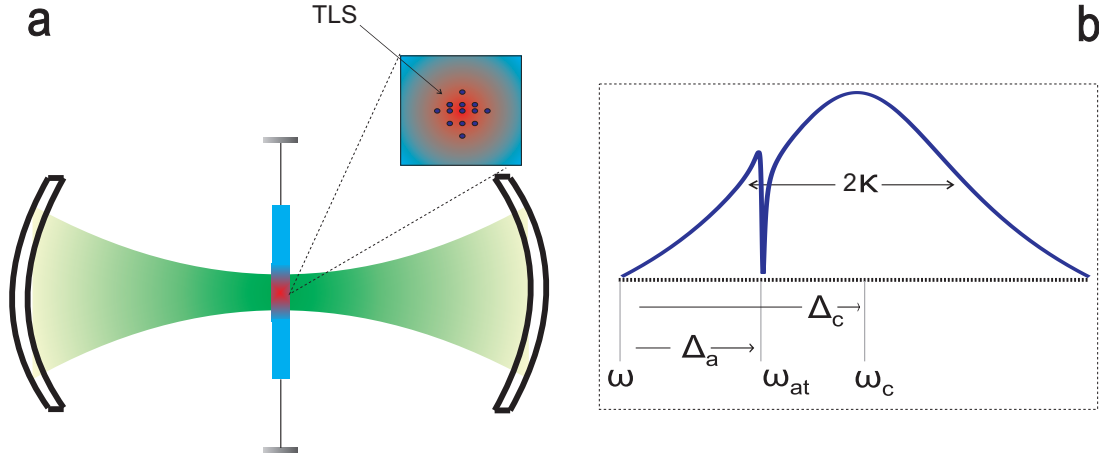


Figure 6.1: Schematics - (a) Hybrid optomechanical setup consisting of a vibrating membrane inside an optical cavity and doped with two-level quantum emitters (TLS) which interact with one cavity field mode. The doping pattern can be tailored to fit vibrational patterns of the membrane and/or the transverse intensity profile of the cavity field. (b) Cavity field susceptibility as a function of frequency, illustrating the bad cavity/good dopant regime in which the cavity linewidth κ is much larger than the dopant linewidth γ . The relevant frequencies and detunings are shown (see text for details).

radiation pressure cooling would be inefficient.

This approach may have several advantages: on the one hand, the TLS can provide narrow resonances and, thereby, a sharper dispersive optomechanical response for the mechanics. On the other hand, their integration into a massive resonator allows for operation in a highly-localized regime with respect to the optical field spatial period, and consequently, an enhanced light-matter interaction. This localization may allow e.g. for the generation or detection of large quantum superposition states [82]. Fundamentally, this strategy thus potentially paves the way towards the realization of novel types of hybrid optomechanical interactions which can be exploited to extend the degree of control of the mechanics. Practically, it is naturally implementable for a wide range of resonators, such as nanomembranes, microspheres or cantilevers, and particularly relevant for resonators whose direct coupling to light via radiation pressure is weak.

The chapter is outlined as follows: Sec. 6.1 presents the model, the effective interaction Hamiltonian and the calculation of the steady state covariance matrix following a standard linearized treatment. In Sec. 6.2 an analytical derivation of the effective mechanical susceptibility and noise terms affecting the mechanics is provided, followed by a discussion of various regimes of interest and numerical results.

6.1 Model

6.1.1 Effective Hamiltonian

We consider the situation depicted in Fig. 6.1, in which a flexible membrane with thickness smaller than the relevant optical wavelengths is positioned inside an optical cavity [10]. Owing to its intrinsic elastic properties and the boundary conditions imposed by the clamping geometry, the membrane exhibits a set of normal modes, denoted by the index s , with effective frequencies ω_s , effective masses m_s and displacement fields $u_s(\mathbf{r})$. We consider its motion along the (cavity) x -axis and denote the transverse position in the (y, z) -plane by the vector \mathbf{r} . After quantization, a general displacement operator in the direction of interest x can be expanded in terms of normal modes $\hat{x}(\mathbf{r}) = \sum_s x_{\text{zpm}}^s u_s(\mathbf{r})(\hat{b}_s + \hat{b}_s^\dagger)$, where \hat{b}_s is the phonon annihilation operator for mode s , while its effective mass is given by $m_s = \rho \int d^2r |u_s(\mathbf{r})|^2$ (assuming constant surface density ρ). The zero-point amplitude is defined as $x_{\text{zpm}}^s = \sqrt{\hbar/(m_s \omega_s)}$.

We consider a poorly reflecting membrane whose dispersive optomechanical coupling with the cavity field is weak [this point is discussed further in Sec. 6.1.6]. We assume however that it is patterned with an ensemble of two-level emitters. Their density is low enough such the bare mechanical properties of the membranes are essentially unchanged, but the emitters interact with the cavity field with dynamics described by the standard Tavis-Cummings interaction. In principle, they can interact with multiple cavity field modes, but we restrict ourselves to the situation where that the cavity field is driven close to resonance with the TLS and with one of the mechanical modes only. We denote by \hat{a} the cavity field annihilation operator and ω_c its frequency, and describe the TLS by continuous Pauli operators $\hat{\sigma}_+(\mathbf{r})$ and $\hat{\sigma}_-(\mathbf{r})$, which are distributed according to a surface distribution function $s(\mathbf{r})$. The Tavis-Cummings interaction between the emitters and the field can then be written as ($\hbar = 1$)

$$H = g_0 \int d\mathbf{r} f(\mathbf{r}) h(\hat{x}(\mathbf{r})) s(\mathbf{r}) \left(\hat{\sigma}_+(\mathbf{r}) \hat{a} + \hat{\sigma}_-(\mathbf{r}) \hat{a}^\dagger \right) \quad (6.1)$$

where g_0 is the vacuum Rabi frequency, f , h are the cavity field transverse and longitudinal modefunctions and $\hat{x}(\mathbf{r}_j) = x_{\text{zpm}} u(\mathbf{r}_j)(\hat{b} + \hat{b}^\dagger)$ the displacement operator of the mechanical mode considered. The continuous Pauli operators are defined such that $[\hat{\sigma}_-(\mathbf{r}), \hat{\sigma}_+(\mathbf{r}')] = \hat{\sigma}_z \delta(\mathbf{r} - \mathbf{r}')$. Although it is not required, we assume for simplicity a weak driving of the two-level emitters, most of which remain in the ground state ($\hat{\sigma}_z \simeq 1$). The surface distribution function $s(\mathbf{r})$ is then normalized such that $\int d\mathbf{r} s^2(\mathbf{r}) = N_a$, where N_a is the total number of TLS.

We then linearize the membrane displacement around its equilibrium position x_0 : $h(\hat{x}(\mathbf{r})) \simeq h(x_0) + h'(x_0) \hat{x}(\mathbf{r})$ (assume that $h'(x_0)$ is non-zero, although the case of a higher-order, e.g. quadratic, coupling in the motion could also be envisaged) and assume the membrane to be located close to the center of a standing wave cavity field, $h(x) = \sin(kx)$, with k the field wavenumber. For typical membranes vibrating at MHz frequencies with \sim ng effective mass it is of the order of fm and one can reasonably assume localization deep into the Lamb-Dicke limit even at room temperature. Introducing the Lamb-Dicke parameter

$\eta_0 = kx_0$ and $\hat{q} = (\hat{b} + \hat{b}^\dagger)/\sqrt{2}$, the interaction Hamiltonian can thus be decomposed as the sum of zeroth- and first-order contributions in \hat{q}

$$H = g_0 \sin(kx_0) \int d\mathbf{r} f(\mathbf{r}) s(\mathbf{r}) \left(\hat{\sigma}_+(\mathbf{r}) \hat{a} + \hat{\sigma}_-(\mathbf{r}) \hat{a}^\dagger \right) + g_0 \cos(kx_0) \eta_0 \hat{q} \sqrt{2} \int d\mathbf{r} f(\mathbf{r}) s(\mathbf{r}) u(\mathbf{r}) \left(\hat{\sigma}_+(\mathbf{r}) \hat{a} + \hat{\sigma}_-(\mathbf{r}) \hat{a}^\dagger \right) \quad (6.2)$$

We now introduce a collective bosonic mode for the TLS effectively coupled to the membrane motional mode as

$$\hat{c} = \frac{1}{\sqrt{N}} \int d\mathbf{r} f(\mathbf{r}) s(\mathbf{r}) u(\mathbf{r}) \hat{\sigma}_-(\mathbf{r}) \quad (6.3)$$

where the effective number of emitters involved in the optomechanical interaction

$$N = \int d\mathbf{r} f^2(\mathbf{r}) s^2(\mathbf{r}) u^2(\mathbf{r}) \quad (6.4)$$

is defined such that $[\hat{c}, \hat{c}^\dagger] = 1$. With $g^{(1)} = g_0 \sqrt{2N} \eta_{LD} \cos(kx_0)$, the first-order part of the Hamiltonian (6.2) becomes

$$H^{(1)} = g^{(1)} \hat{q} \left(\hat{c} \hat{a}^\dagger + \hat{c}^\dagger \hat{a} \right) \quad (6.5)$$

The zeroth-order part of Hamiltonian (6.2) involves the collective mode $\int d\mathbf{r} f(\mathbf{r}) s(\mathbf{r}) \hat{\sigma}_-(\mathbf{r})$, which is *a priori* different from the previously defined collective mode. This mode can be conveniently written as a weighted sum of mode \hat{c} , and another orthogonal mode, \hat{c}_0 , by the relation

$$\int d\mathbf{r} f(\mathbf{r}) s(\mathbf{r}) \hat{\sigma}_-(\mathbf{r}) = \sqrt{N} (\alpha \hat{c} + \beta \hat{c}_0) \quad (6.6)$$

where

$$\alpha = \frac{\int d\mathbf{r} f^2(\mathbf{r}) s^2(\mathbf{r}) u(\mathbf{r})}{\int d\mathbf{r} f^2(\mathbf{r}) s^2(\mathbf{r}) u^2(\mathbf{r})}, \quad (6.7)$$

$$\beta = \sqrt{\frac{1}{N} \int d\mathbf{r} f^2(\mathbf{r}) s^2(\mathbf{r}) [1 - \alpha u(\mathbf{r})]^2} \quad (6.8)$$

ensure that $[\hat{c}_0, \hat{c}_0^\dagger] = 1$ and $[\hat{c}, \hat{c}_0^\dagger] = 0$. With this decomposition the total interaction Hamiltonian can be expressed as

$$H = \beta g^{(0)} \left(\hat{c}_0 \hat{a}^\dagger + \hat{c}_0^\dagger \hat{a} \right) + \left(\alpha g^{(0)} + g^{(1)} \hat{q} \right) \left(\hat{c} \hat{a}^\dagger + \hat{c}^\dagger \hat{a} \right) \quad (6.9)$$

with $g^{(0)} = g_0 \sqrt{N} \sin(kx_0)$. To simplify the discussion we will assume in the following $\alpha \sim 1, \beta \sim 0$, so that the interaction Hamiltonian only involves the collective mode coupled to the membrane motion. (This can be ensured by having an optical mode waist, or equivalently a dopant area, smaller than the mechanical mode size. Note that the inclusion of the contribution of the static Hamiltonian involving the collective mode which is not coupled to the mechanics essentially amounts to modifying the cavity susceptibility and noise, and it can be checked that it does not qualitatively changes the results discussed in the conceptually simpler case $\beta = 0$.)

$$H = \left(g^{(0)} + g^{(1)} \hat{q} \right) \left(\hat{c} \hat{a}^\dagger + \hat{c}^\dagger \hat{a} \right) \quad (6.10)$$

6.1.2 Equations of motion

The cavity mode at frequency ω_c is driven optically via the side mirror with a laser of amplitude η and frequency ω . The free evolution (in a frame rotating at ω) is governed by

$$H_0 = \frac{1}{2}\omega_m(\hat{p}^2 + \hat{q}^2) + \Delta_c\hat{a}^\dagger\hat{a} + \Delta_a\hat{c}^\dagger\hat{c}, \quad (6.11)$$

where $\hat{p} = i(\hat{b}^\dagger - \hat{b})/\sqrt{2}$ and $\Delta_c = \omega_c - \omega$, $\Delta_a = \omega_{at} - \omega$ are the cavity and atomic detunings and ω_m the mechanical frequency (Fig. 6.1) and the conventions $[\hat{a}, \hat{a}^\dagger]$ and $[\hat{q}, \hat{p}] = i$ are used. The driving Hamiltonian is

$$H_L = i\eta(\hat{a}^\dagger - \hat{a}) \quad (6.12)$$

For a complete description of the dynamics the dissipation channels have to be accounted for. These consist of (i) losses owing to the mechanical coupling to thermal environment at a rate γ_m , (ii) cavity losses of photons at a rate κ and (iii) TLS decay at a rate γ . The corresponding Liouvillians are $\mathcal{L}_{\hat{O}}[\rho] = \Gamma_{\hat{O}}\mathcal{D}_{\hat{O}}[\rho] = \Gamma_{\hat{O}}[\hat{O}\rho\hat{O}^\dagger - \hat{O}^\dagger\hat{O}\rho - \rho\hat{O}^\dagger\hat{O}]$ with \hat{O} and $\Gamma_{\hat{O}}$ standing for the collapse operators \hat{a} , \hat{b} , \hat{c} and their associated loss rates κ , γ_m and γ , respectively.

Adding dissipation to the full Hamiltonian evolution given by Eqs. (6.10,6.11,6.12) yields the following Heisenberg-Langevin equations of motion

$$\dot{\hat{a}} = -(\kappa + i\Delta_c)\hat{a} - i(g^{(0)} + g^{(1)}\hat{q})\hat{c} + \eta + \hat{a}_{in} \quad (6.13)$$

$$\dot{\hat{c}} = -(\gamma + i\Delta_a)\hat{c} - i(g^{(0)} + g^{(1)}\hat{q})\hat{a} + \hat{c}_{in} \quad (6.14)$$

$$\dot{\hat{p}} = -\gamma_m\hat{p} - \omega_m\hat{q} - g^{(1)}(\hat{a}^\dagger\hat{c} + \hat{c}^\dagger\hat{a}) + \hat{\xi} \quad (6.15)$$

$$\dot{\hat{q}} = \omega_m\hat{p} \quad (6.16)$$

where the field, atomic and mechanical input noise terms, \hat{a}_{in} , \hat{c}_{in} and $\hat{\xi}$, are zero mean-valued and have correlation functions $\langle \hat{a}_{in}(t)\hat{a}_{in}^\dagger(t') \rangle = 2\kappa\delta(t-t')$, $\langle \hat{c}_{in}(t)\hat{c}_{in}^\dagger(t') \rangle = 2\gamma\delta(t-t')$ and $\langle \hat{\xi}(t)\hat{\xi}(t') \rangle = \gamma_m(1+2n_m)\delta(t-t')$, respectively. For the thermal noise term, the standard Ohmic bath approximation has been made and n_m represents the initial thermal occupation number of the mechanical mode considered.

6.1.3 Steady state and linearized equations

Denoting by $\bar{O} = \langle O \rangle$ the steady state value of \hat{O} , and using $\bar{c}_{in} = 0$, $\bar{a}_{in} = 0$ and $\bar{\xi} = 0$, one obtains the steady state mean values by solving the following set of equations

$$0 = -(\kappa + i\Delta_c)\bar{a} - i(g^{(0)} + g^{(1)}\bar{q})\bar{c} + \eta \quad (6.17)$$

$$0 = -(\gamma + i\Delta_a)\bar{c} - i(g^{(0)} + g^{(1)}\bar{q})\bar{a} \quad (6.18)$$

$$0 = -\omega_m\bar{q} - g^{(1)}(\bar{a}^*\bar{c} + \bar{c}^*\bar{a}) \quad (6.19)$$

which gives

$$\bar{c} = -\frac{i(g^{(0)} + g^{(1)}\bar{q})}{\gamma + i\Delta_a}\bar{a} \equiv -\frac{ig}{\gamma + i\Delta_a}\bar{a} \quad (6.20)$$

where, in order to make the connection with the standard cavity QED settings, we included the mean position shift in an effective atom-light coupling $g = g^{(0)} + g^{(1)}\bar{q}$. Typically, $g^{(1)}$ is small enough so that $g \simeq g^{(0)}$ can be assimilated to the standard collective coupling rate for a superemitter localized at position q_0 . For not too high intracavity photon numbers, one can also reasonably assume that the optical spring-induced modification of the mechanical frequency is such that $\omega_m > 2g^{(1)}|\bar{a}|^2\Delta_a/(\gamma^2 + \Delta_a^2)$. The mean position shift is then given by

$$\bar{q} = \frac{2g^{(1)}|\bar{a}|^2\frac{g^{(0)}\Delta_a}{\gamma^2 + \Delta_a^2}}{\omega_m - \frac{2\Delta_a G^2}{\gamma^2 + \Delta_a^2}}, \quad (6.21)$$

where we defined $G = g^{(1)}\bar{a}$ in analogy with the enhanced optomechanical coupling in the standard dispersive optomechanics in the linearized regime (see Sec. 6.1.5). \bar{a} is solution of

$$\left[\kappa + i\Delta_c + \frac{g^2}{\gamma + i\Delta_a} \right] \bar{a} = \eta. \quad (6.22)$$

Without loss of generality we take \bar{a} to be real and positive. Let us note that, at high optomechanical coupling strengths, the previous equation may give rise to multistable solutions for the intracavity field photon number, since g depends on \bar{a} through \bar{q} . We assume in the following that we operate outside of this instability regime.

Assuming these static stability conditions met, we proceed with the usual linearization around steady state by decomposing each observable as the sum of its steady state mean values and its fluctuations $\hat{o} = \bar{o} + o$. Neglecting second order terms for the fluctuations, we obtain

$$\dot{a} = -(\kappa + i\Delta_c)a + G\frac{g}{\gamma + i\Delta_a}q + a_{in} \quad (6.23)$$

$$\dot{c} = -(\gamma + i\Delta_a)c - iga - iGq + c_{in} \quad (6.24)$$

$$\dot{p} = -\gamma_m p - \omega_m q - G\left[c + \frac{ig}{\gamma - i\Delta_a}a + \text{h.c.} \right] + \xi \quad (6.25)$$

$$\dot{q} = \omega_m p \quad (6.26)$$

The dynamic stability of the system can thus be determined by examining the eigenvalues of the evolution matrix

$$[A] = \begin{pmatrix} -\gamma & \Delta_a & 0 & g & 0 & 0 \\ -\Delta_a & -\gamma & -g & 0 & -\sqrt{2}g & 0 \\ 0 & g & -\kappa & \Delta_c & -\frac{gG\gamma\sqrt{2}}{\gamma^2 + \Delta_a^2} & 0 \\ -g & 0 & -\Delta_c & -\kappa & \frac{gG\Delta_a\sqrt{2}}{\gamma^2 + \Delta_a^2} & 0 \\ 0 & 0 & 0 & 0 & 0 & \omega_m \\ -G\sqrt{2} & 0 & -\frac{igG}{\gamma - i\Delta_a} & \frac{igG}{\gamma + i\Delta_a} & -\omega_m & -\gamma_m \end{pmatrix} \quad (6.27)$$

expressed in the basis of the quadratures (X, Y, x, y, q, p) , where $X = (c + c^\dagger)/\sqrt{2}$, $Y = i(c^\dagger - c)/\sqrt{2}$, $x = (a + a^\dagger)/\sqrt{2}$, $y = i(a^\dagger - a)/\sqrt{2}$. When the real part of each eigenvalue is

strictly negative the system is stable and the steady state covariance matrix of the system, $[V]$, can be calculated by solving the Lyapunov equation

$$[A][V] + [V][A]^\dagger = -[D] \quad (6.28)$$

where $[D] = \text{diag}[\gamma, \gamma, \kappa, \kappa, 0, \gamma_m(1 + 2n_m)]$ is the diffusion matrix.

6.1.4 Effective mechanical susceptibility, noise spectrum and final occupation number for the mechanics

In order to get some more insight into the dynamics of the system we analytically derive the effective mechanical susceptibility and the effective noise terms for the mechanics. To do so, we Fourier transform eqs. (6.23-6.26) and, after some algebra, obtain the expression of the Fourier transform of the position fluctuations $q(\omega)$

$$\begin{aligned} \chi_m^{\text{eff}}(\omega)^{-1} q(\omega) \\ = \Lambda(\omega) c_{in} + \Lambda^*(-\omega) c_{in}^\dagger + \Upsilon(\omega) a_{in} + \Upsilon^*(-\omega) a_{in}^\dagger + \xi \end{aligned} \quad (6.29)$$

where $\chi_m^{\text{eff}}(\omega)^{-1}$ is the effective mechanical susceptibility

$$\chi_m^{\text{eff}}(\omega)^{-1} = \chi_m(\omega)^{-1} + \Theta(\omega) + \Xi(\omega) \quad (6.30)$$

with

$$\chi_m(\omega)^{-1} = (\omega_m^2 - \omega^2 - i\gamma_m\omega)/\omega_m \quad (6.31)$$

$$\Theta(\omega) = -\frac{2G^2\Delta_a}{(\gamma - i\omega)^2 + \Delta_a^2} \quad (6.32)$$

$$\Xi(\omega) = -G^2[\chi_c(\omega)A(\omega) + \chi_c^*(-\omega)A^*(-\omega)] \quad (6.33)$$

$$\chi_c(\omega)^{-1} = \kappa + i\Delta_c - i\omega + \frac{g^2}{\gamma + i\Delta_a - i\omega} \quad (6.34)$$

$$A(\omega) = \frac{ig^2}{\gamma^2 + \Delta_a^2} \frac{(2\gamma + 2i\Delta_a - i\omega)(2i\Delta_a - i\omega)}{(\gamma + i\Delta_a - i\omega)^2} \quad (6.35)$$

and

$$\Lambda(\omega) = \frac{G}{\gamma + i\Delta_a - i\omega} \left[1 + \frac{g^2}{\gamma - i\Delta_a} \chi_c(\omega) B(\omega) \right] \quad (6.36)$$

$$\Upsilon(\omega) = G \frac{ig}{\gamma - i\Delta_a} \chi_c(\omega) B(\omega) \quad (6.37)$$

$$B(\omega) = \frac{2i\Delta_a - i\omega}{\gamma + i\Delta_a - i\omega} \quad (6.38)$$

Eq. (6.29) shows that the mechanical oscillator fluctuations are given by the product of the effective susceptibility and the sum of fluctuations arising from three uncorrelated noise terms coming from the atoms, the incoming field and the coupling with the thermal

reservoir, respectively. One can compute the steady state noise spectrum of the position observable by

$$S_q(\omega) = |\chi_m^{\text{eff}}(\omega)|^2 \left[2\gamma |\Lambda(\omega)|^2 + 2\kappa |\Upsilon(\omega)|^2 + \gamma_m(1 + 2n_m) \right] \quad (6.39)$$

As a figure of merit for cooling we will consider the final occupation number in the mechanics obtained by integration of the noise spectrum of the position observable

$$n_f = \Delta q^2 - \frac{1}{2} = \int \frac{d\omega}{2\pi} S_q(\omega) - \frac{1}{2} \quad (6.40)$$

Note that, strictly speaking, this occupation number should be defined as $(\Delta q^2 + \Delta p^2 - 1)/2$ [89], but, for the situations we will consider, the difference is negligible.

6.1.5 Standard dispersive radiation pressure optomechanics

Before exploring the dynamics of the doped system in various parameter regimes it is interesting to briefly recall the results for the standard radiation pressure optomechanics in the dispersive regime. Starting from the Hamiltonian $H_{OM} = G_0 \hat{a}^\dagger \hat{a} \hat{q}$ and assuming a weak single-photon optomechanical coupling G_0 , the same linearization approach would yield an effective mechanical susceptibility [89–91]

$$\chi_m^{\text{OM}}(\omega)^{-1} = \chi_m(\omega)^{-1} - \frac{2G_{\text{OM}}^2 \Delta_c}{(\kappa - i\omega)^2 + \Delta_c^2} \quad (6.41)$$

with $G_{\text{OM}} = G_0 \bar{a}$. For a high mechanical quality factor, the mechanics noise spectrum is still approximately that of a harmonic oscillator, but with an effective mechanical damping modified by the radiation pressure

$$\gamma_m \rightarrow \gamma_m + \Im \left[\frac{2G_{\text{OM}}^2 \Delta_c}{(\kappa - i\omega_m)^2 + \Delta_c^2} \right] \quad (6.42)$$

In the good cavity limit, $\kappa \ll \omega_m$, driving the mechanics on the red sideband ($\Delta_c = \omega_m$) gives cooling of the mechanics with a rate $\Gamma = G_{\text{OM}}^2/\kappa$, while being resonant with the blue sideband can give rise to self-oscillations when $G_{\text{OM}}^2 \gtrsim 2\kappa\gamma_m$. In the bad cavity limit, $\kappa \gg \omega_m$, cooling is optimum for $\Delta_c \sim \kappa/\sqrt{3}$, while self-oscillations also occur as soon as $G_{\text{OM}}^2 \gtrsim 2\kappa\gamma_m$ for $\Delta_c \sim -\kappa$. Ground state cooling is possible in the good cavity limit where, for $\Delta_c = \omega_m$ and neglecting second order terms in $(\kappa/\omega_m)^2$, the final occupation number is given by

$$n_f = \frac{\gamma_m}{\gamma_m + \Gamma} n_m \quad (6.43)$$

6.1.6 Doped versus radiation pressure optomechanics

In principle, both the dopant-mediated coupling and the radiation pressure forces can affect the mechanics of the semi-transparent membrane. It is thus interesting to compare

their magnitude in the linearized regime considered here. For a membrane with amplitude reflectivity coefficient r , the single-photon optomechanical coupling in the standard dispersive optomechanics scenario discussed in the previous section is given by $G_0 = r(\omega/L)x_{\text{zpm}}$, where L is the cavity length. Including the term arising from the Hamiltonian H_{OM} in the dynamical equation for the intracavity field fluctuations (6.23) would modify it to

$$\dot{a} = -(\kappa + i\Delta_c)a + \left[G \frac{g}{\gamma + i\Delta_a} - iG_{OM} \right] q + a_{in} \quad (6.44)$$

where $G = g^{(1)}\bar{a}$ and $G_{OM} = G_0\bar{a}$. Anticipating on the results in the next section, we set $\Delta_a = 0$ and compare the ratio of the modulus of the two terms in the square brackets: $(Gg/\gamma)/G_{OM}$, which essentially gives the ratio of the magnitude of the two optomechanical forces. Recalling that $g^{(1)} \sim g\eta_{LD}\beta = g(\omega/c)x_{\text{zpm}}\beta$ and assuming $\beta \sim 1$, this ratio becomes

$$\frac{gG/\gamma}{G_{OM}} \sim \frac{g^2L}{rc\gamma} = \frac{\alpha}{r} \quad (6.45)$$

where $\alpha = g^2L/(c\gamma) = \frac{3}{4\pi} \frac{\lambda^2}{S} N$ is the single-pass optical depth of the dopant ensemble (S being the beam cross section). This simple order of magnitude estimate shows that the doped optomechanical force can dominate over the dispersive radiation pressure force for poorly reflecting membranes and optically dense dopant.

In the following we will compare the effect of these forces acting separately on the mechanics, the extension to the situation where both forces simultaneously play a role being straightforward.

6.2 Results

6.2.1 Effective resolved sideband cooling with good dopant

Of particular interest is a dopant having a narrow resonance as compared to the cavity linewidth and the mechanical frequency, as it can allow for effective resolved sideband cooling of the mechanics.

For a bad cavity, i.e. for a cavity field decay rate κ much larger than the other relevant frequencies and rates, the field susceptibility $\chi_c(\omega)$ is small, which means that one can neglect $\Xi(\omega)$ in Eq. (6.30), and the effective mechanical susceptibility is dominated by the atomic response $\Theta(\omega)$. The expression of $\Theta(\omega)$ [Eq. (6.32)] is formally identical to the field response in the standard theory for dispersive radiation pressure optomechanics, with the atoms replacing the field [i.e. replacing Δ_c by Δ_a and κ by γ in Eq. (6.41)]. Indeed, for $\gamma, g \ll \omega_m \ll \kappa$ and neglecting $\Xi(\omega)$, driving the mechanics on the red sideband $\Delta_a = \omega_m$ gives rise to optomechanical cooling with a rate $\Gamma = G^2/\gamma$ and a cooling limit given by Eq. (6.43) in the effectively resolved sideband regime induced by the atoms. This is illustrated in Fig. 6.2a, which shows the final occupation number as a function of the atomic detuning for a 'good' dopant ($\gamma/\omega_m = 0.01$, blue dots) in a 'bad' cavity ($\kappa/\omega_m = 10$). For comparison, the red curve shows the result in the corresponding standard

radiation pressure scenario (for the same cavity and comparable optomechanical coupling $G_{\text{OM}} = G$), which displays very inefficient cooling, as $\Gamma \sim \gamma_m/10$ in this case.

Let us now consider a cavity in the intermediate regime $\omega_m \sim \kappa \gg g$, for which one can no longer neglect the contribution from the field susceptibility in $\Xi(\omega)$. If one assumes that the cavity is also detuned to the red sideband ($\Delta_c = \omega_m$), one can neglect blue sideband contributions in the effective susceptibility as well as in the effective noise terms. Introducing the cooperativity parameter $C = g^2/\kappa\gamma$, one has $\chi_c(\omega_m) \sim 1/(\kappa + g^2/\gamma) = 1/\kappa(1 + C)$ and the optomechanical damping becomes

$$\Gamma = \frac{G^2}{\gamma(1 + C)}. \quad (6.46)$$

The effective atomic and field noise terms reduce to $[G/(1+C)]c_{in}$ and $[-igG/\kappa\gamma(1+C)]a_{in}$, respectively. It follows that the final occupation number is formally given by Eq. (6.43) with Γ defined by Eq. (6.46). The increase in the effective cavity linewidth due to the coupling with the dopant thus effectively reduces the cooling rate.

The blue circles in Fig. 6.2b show the final occupation number as a function of the atomic detuning for a 'good' dopant in this intermediate cavity regime ($\omega_m = \kappa$). As expected, the dip occurring around $\Delta_a = \omega_m$ corresponds to an effective resolved sideband cooling of the mechanics, which is slightly less efficient than in Fig. 6.2a, although still noticeably better than the corresponding radiation pressure scenario (red dots). However, one also observes a second cooling 'dip', occurring for $\Delta_a = 0$, which we discuss in the next section.

6.2.2 Enhanced optomechanical interactions with resonant dopant

As observed in the previous section another interesting regime for enhancing the optomechanical interaction is to have the driving laser frequency resonant ($\Delta_a = 0$) with a doping medium which is in the resolved sideband regime ($\gamma \ll \omega_m$). In this case, the purely atomic contribution $\Theta(\omega)$ vanishes and only the fluctuations of the cavity field (dressed by the dopant) contribute to the effective mechanical susceptibility. With $A(\omega_m) \simeq i(g/\gamma)^2$, the effective mechanical damping is given by

$$\gamma_m + \Im \left[\frac{2G^2 \left(\frac{g}{\gamma}\right)^2 \Delta_c}{\left(\kappa - i\omega_m + \frac{g^2}{\gamma - i\omega_m}\right)^2 + \Delta_c^2} \right] \quad (6.47)$$

This result is again reminiscent of the standard dispersive optomechanics result [Eq. (6.42)]. However, a first noticeable difference is that the optomechanical coupling rate G is now multiplied by the ratio g/γ , which can be substantially larger than unity for a strongly coupled dopant. The other noteworthy difference is that the cavity susceptibility is dressed by the dopant, as evidenced by the term $g^2/(\gamma - i\omega_m)$ in the denominator of Eq. (6.47). Still assuming that $\gamma \ll \omega_m$, this implies that the sign and amplitude of the second term in Eq. (6.47) essentially depend on the quantity $\omega_m - g^2/\omega_m$. Two regimes can then be

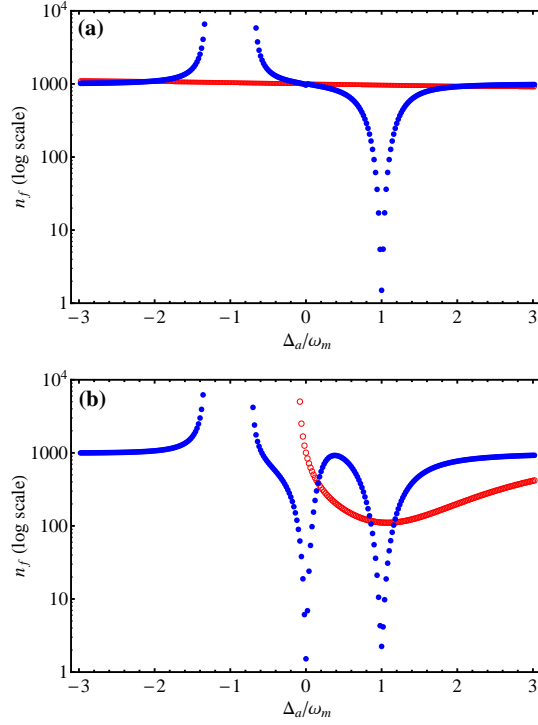


Figure 6.2: Final occupation number n_f as a function of atomic detuning Δ_a (blue dots): in (a) the bad ($\kappa/\omega_m = 10$, $g/\omega_m = 10^{-2}$) and (b) intermediate ($\kappa/\omega_m = 1$, $g/\omega_m = 0.1$) cavity regimes. Parameters: $\gamma/\omega_m = 10^{-2}$, $\Delta_c/\omega_m = 1$, $\gamma_m/\omega_m = 10^{-5}$, $G/\omega_m = 10^{-2}$, and $n_m = 10^3$. The corresponding standard radiation pressure OM result (in which case the x -axis represents Δ_c/ω_m) is shown by the red circles for comparison. Only points corresponding to stable working points are shown.

distinguished: (i) $g \ll \omega_m$: a 'weak' coupling regime with the dopant, for which optimal cooling is obtained with a cavity field tuned to the red sideband $\Delta_c \sim \omega_m$, and (ii) $g \gg \omega_m$: a 'strong' coupling regime with the dopant, for which cooling can be achieved with a blue detuned cavity field.

More precisely, if one imposes

$$\Delta_c = \Delta_0 \equiv \omega_m - \frac{g^2}{\omega_m}, \quad (6.48)$$

one has that

$$\Xi(\omega_m) \simeq -G^2 \left(\frac{g}{\gamma} \right)^2 \frac{2\Delta_0}{\kappa^2 - 2i\kappa\Delta_0} \quad (6.49)$$

In the good cavity limit ($\kappa \ll |\Delta_0|$), the effective cooling rate is given by

$$\Gamma = \frac{G^2}{\kappa} \left(\frac{g}{\gamma} \right)^2 \quad (6.50)$$

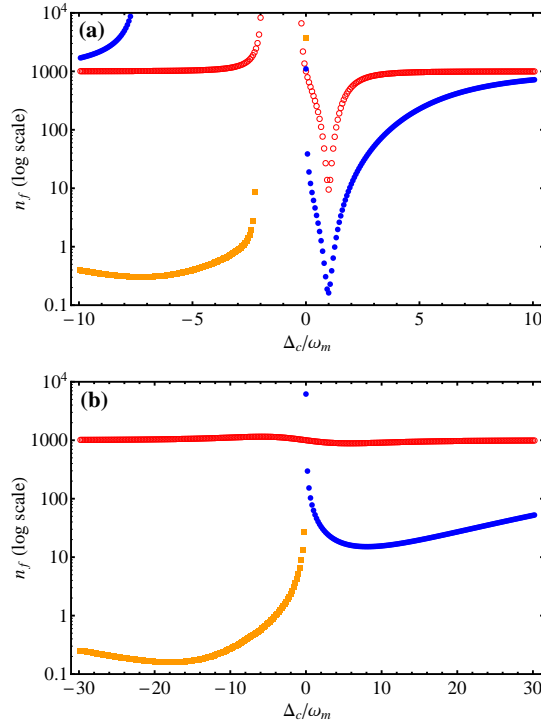


Figure 6.3: Final occupation number n_f as a function of cavity detuning Δ_c for a resonant dopant ($\Delta_a = 0$). (a) *Good cavity limit* ($\kappa/\omega_m = 0.1$) – Red circles: Standard OM. Blue dots: doped OM with a ‘weakly’ coupled dopant $g/\omega_m = 0.1$. Yellow squares: doped OM with a ‘strongly’ coupled dopant $g/\omega_m = 3$. (b) *Bad cavity limit* ($\kappa/\omega_m = 10$) – Red circles: Standard OM. Blue dots: doped OM with a ‘weakly’ coupled dopant $g/\omega_m = 0.72$. Yellow squares: doped OM with a ‘strongly’ coupled dopant $g/\omega_m = 4$. Other parameters: $\gamma_m/\omega_m = 10^{-5}$, $G/\omega_m = 10^{-2}$, $\gamma/\omega_m = 10^{-2}$ and $n_m = 10^3$. Only points corresponding to stable working points are shown.

As aforementioned, it is enhanced with respect to the standard rate by the factor $(g/\gamma)^2$. Moreover, one has $B(\omega) \simeq 1$, $\Lambda(\omega_m) \simeq \frac{iG(1+g^2/\kappa\gamma)}{\omega_m}$ and $\Upsilon(\omega_m) \simeq \frac{igG}{\gamma\kappa}$, which yields a final occupation number given by Eq. (6.43), plus an extra atomic noise contribution equal to $\frac{(1+C)^2}{C} \left(\frac{\gamma}{\omega_m}\right)^2$. This shows that ground state cooling is in principle possible, but, since C increases with g , a too strong coupling with the dopant may increase the amount of added atomic noise. There is therefore a tradeoff between enhanced cooling rate and added extra atomic noise.

This result is illustrated in Fig. 6.3a, in which the final occupation number as a function of the cavity detuning is shown in both regimes, $g/\omega_m = 0.1$ (blue dots) and $g/\omega_m = 3$ (yellow squares). The bare optomechanical coupling rate and parameters were chosen so that standard OM cooling (red circles) with an equivalent G does not allow for reaching the motional ground state. Clearly, an improvement of about two orders of magnitude is

possible for a weakly coupled doped system around $\Delta_c \sim \omega_m$. As a result of the enhanced optomechanical coupling, optomechanical instabilities for blue cavity detunings also occur comparatively sooner than in the standard OM situation. In the strong coupling regime (yellow squares), as expected from the previous discussion, instabilities are observed for red detunings, while efficient cooling to the ground state is achieved for a wide range of blue detunings around $\Delta_c \sim \Delta_0 \simeq -8\omega_m$.

In the bad (dressed) cavity limit ($\kappa \gg |\Delta_0|$) and for a cavity detuned by $\Delta_c \sim \kappa$, the cooling rate is given by

$$\Gamma = \frac{G^2}{\kappa} \left(\frac{g}{\gamma} \right)^2 \frac{\omega_m}{\kappa}. \quad (6.51)$$

Similarly to the standard OM result, the cooling rate is decreased by a factor $\sim \omega_m/\kappa$ as compared to the good cavity limit, and the lowest achievable final occupation number of Eq. (6.43) has to be divided by the same factor. However, let us note that, in the strongly coupled dopant regime $g > \omega_m$, κ should be compared to g^2/ω_m in the dressed susceptibility. This means that one can operate in the unresolved sideband regime for the bare system ($\omega_m < \kappa$), but effectively be in the resolved sideband regime for a strongly coupled doped system satisfying $g^2 > \omega_m\kappa$, and thereby still achieve ground state cooling.

This is illustrated in Fig. 6.3b, in which the bad cavity regime for the bare system is explored ($\kappa/\omega_m = 10$). While standard OM cooling (red circles) is very inefficient, the enhanced optomechanical coupling with a weakly coupled dopant allows for better cooling at red cavity detunings $\Delta_c \sim \kappa/\sqrt{3}$, albeit not to the ground state (blue dots). With a strongly coupled dopant with $g/\omega_m = 4$ – such that effective sideband resolution is achieved for the dressed system ($\Delta_0 \sim -1.5\kappa$) – ground state cooling is possible for blue detunings around $\Delta_c \sim \Delta_0$ (yellow squares).

6.2.3 Polariton optomechanics

A natural picture for interpreting these results can be provided by introducing the atom-field mixtures – *polaritons* – which diagonalize the Hamiltonian $H_0 + H_{int}$. If one assumes for simplicity that the atomic and cavity detunings are kept equal ($\Delta_a = \Delta_c = \Delta$), the polaritons are symmetric combinations of the atomic and field modes

$$\hat{u} = \frac{\hat{a} + \hat{c}}{\sqrt{2}}, \quad \hat{v} = \frac{\hat{a} - \hat{c}}{\sqrt{2}}, \quad (6.52)$$

which give the Hamiltonian

$$H = \frac{1}{2}\omega_m(\hat{p}^2 + \hat{q}^2) + [\Delta + g(q_0, \hat{q})]\hat{u}^\dagger\hat{u} + [\Delta - g(q_0, \hat{q})]\hat{v}^\dagger\hat{v} \quad (6.53)$$

In the strong coupling regime, when the polaritons are well-resolved ($g \gg \kappa, \gamma$), optomechanical cooling is then obtained when one drives the polaritons' red sideband, i.e. when $\Delta = \Delta_\pm \equiv \pm g + \omega_m$. A detailed analysis shows that the effective cooling rate is given by $\Gamma = G^2/\bar{\kappa}$, where $\bar{\kappa} = (\kappa + \gamma)/2$ is the effective polariton decay rate. The case $g/\omega_m = 6$ is illustrated in Fig. 6.4a, which clearly shows optomechanically induced cooling and heating

around $\pm g + \omega_m$ and $\pm g - \omega_m$, respectively. A similar behavior is observed in Fig. 6.4c for the weak coupling regime $g/\omega_m = 0.2$. However, remarkably, heating and cooling are also observed around $\Delta = 0$. This may seem surprising as both $\Xi(\omega_m)$ and $\Theta(\omega_m)$ vanish exactly on resonance $\Delta = 0$. Nevertheless, for small detunings, the asymmetrical coupling to both polaritons yields a non-zero effective mechanical damping (or antidamping). Indeed, assuming still $\gamma \ll \omega_m$ and expanding $\Xi(\omega_m)$ in Eq. (6.33) at first order in Δ gives an optomechanical damping/antidamping rate

$$\Gamma \simeq \left(\frac{Gg}{\gamma} \right)^2 \frac{4\kappa\Delta_0\Delta}{(\kappa^2 - \Delta_0^2 + \Delta^2)^2 + 4\kappa^2\Delta_0^2} \quad (6.54)$$

In the strong ($g \gg \omega_m$) and weak ($g \ll \omega_m$) coupling regimes, $|\Delta_0| \gg 1$ and the damping/antidamping is relatively small $\Gamma \propto (Gg/\gamma)^2 4\kappa\Delta/\Delta_0^3$, as shown in Figs. 6.4a and c. However, in the intermediate coupling regime ($g \sim \omega_m$), Δ_0 becomes small and, for $\Delta \simeq \Delta_0$, one retrieves the enhanced cooling rate of Eq. (6.50). This is illustrated in Fig. 6.4b, where $g/\omega_m = 0.8$ and ground state cooling is nearly achieved. The physical interpretation of this somewhat intriguing result is that, when $g \sim \omega_m$ and $\Delta \sim 0$, the lower polariton's red sideband is close to resonance with the upper polariton's blue sideband. The interference between the scattering amplitudes into the two sidebands gives rise to a strong dispersive optomechanical interaction, causing the observed enhanced optomechanical cooling/heating. Note that this effect does not originate from interference in the effective noise terms, but in the scattering amplitudes in the mechanical sidebands (imaginary part of the effective mechanical susceptibility). This is corroborated by the inset Fig. 6.4b, showing a variation of Γ with the detuning which perfectly correlates with the variation of the final occupation number in the mechanics.

6.3 Conclusion

We have investigated a hybrid approach to optomechanics in which the addressing of a mechanical resonator's motion is achieved indirectly via the coupling of light with an embedded dopant comprised of an ensemble of TLS. We have shown that enhanced effective optomechanical interactions in the linearized regime can be achieved with both weakly- or strongly-coupled dopant. As an example we have shown that such interactions can be used to facilitate ground state cooling of mechanical modes of resonators for which direct coupling with light via radiation pressure is otherwise weak.

From a fundamental point of view, it is worth noting that the coupling studied in the present work, in contrast with similar schemes [62], is not provided by an effective two-body interaction where atom-mechanics coupling is obtained after tracing over the mediating field, but rather by an intrinsic tripartite interaction where mechanical operators are directly coupled to dressed light-matter states [Eq. 6.10]. For strong coupling between dopant and light, for instance, interesting dynamics between the mechanics and light-matter polaritons can be engineered.

From a more practical point of view, this approach can be beneficial for the design of mechanical resonators with e.g. low reflectivity – such as membranes [10], levitated

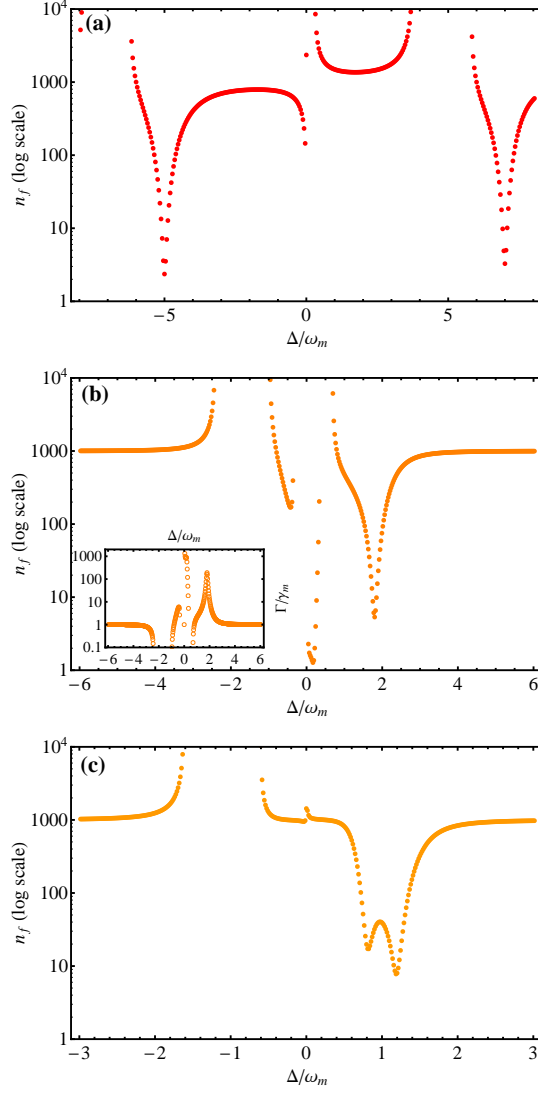


Figure 6.4: Final occupation number n_f as a function of polariton detuning Δ , for various coupling strengths: (a) $g/\omega_m = 6$, (b) $g/\omega_m = 0.8$ and (c) $g/\omega_m = 0.2$. Parameters: $\kappa/\omega_m = 0.1$, $\gamma/\omega_m = 10^{-2}$, $\gamma_m/\omega_m = 10^{-5}$, $n_m = 10^3$, $G/\omega_m = 10^{-2}$. The inset in (b) shows the variation of the optomechanical damping rate Γ , normalized to γ_m .

submicron particles [92, 93], molecule-embedded polymer layers [94], etc. The optimization of their mechanical properties can then to some extent be disentangled from the optical ones, since, by choosing the dopant, optical properties can be independently tailored. Moreover, the flexibility in matching doping patterns with vibrational and optical mode profiles may present a great advantage for multimode addressing of the system.

Chapter 7

Conclusion

In this thesis, we have established several aspects of starting a new experimental activity on nanomembrane optomechanics. We have discussed a wide range of topics from assembling and developing periodic membrane arrays in chapter 3, to designing and building low-pressure environments for the future optomechanics experiments in chapter 4, developing high reflectivity membranes by nanostructuring techniques in chapter 5 and also theoretically investigating cavity optomechanics with extended or doped membrane resonators.

In chapter 3 we report the first known assembly of Si_3N_4 membranes, developed with the aim to investigate collective optomechanics in the transmissive regime. We developed techniques for the assembly and characterization of double membrane arrays which can be easily extended to create arrays of more than two elements.

So far different double membrane arrays, with separation distances ranging from $8.5\ \mu\text{m}$ to $200\ \mu\text{m}$ have been assembled and glued. These double membrane arrays show near to unity transmission ($> 97\%$), with the $8.5\ \mu\text{m}$ spacer array giving the best results ($\approx 99.7\%$).

In the near future, we aim to extend the gluing process to assemble arrays with more than two membranes and improve on parallelism control during assembly in order to achieve closer-to-unity transmission in N-membrane arrays.

In chapter 4 we discuss the assembly and vacuum testing of our two experimental chambers. Mechanical characterization chamber being of immediate interest to us, we have concentrated our efforts in building, vacuum testing, and setting up optics for measurement scheme. At the time of writing measurements to determine the mechanical properties of the assembled arrays were under way.

From our theoretical investigations in chapter 2 and as suggested in references [34][37], we know that the collective optomechanical coupling strength scales quadratically with the membrane polarizability (ζ). This prompted us in designing and developing high reflectivity membranes by fabricating 1D photonic structures such as a grating on a Si_3N_4 membrane. Chapter 5 discusses our venture into the field of fabrication and characterization of gratings on high stress Si_4N_4 membranes. Fabrication of grating on Si_3N_4 membranes took us

several trials since the etching of Si_3N_4 through the membrane seemed to be a daunting task due to the fragility of the membrane structure. After several trials of adjusting various fabrication parameters, we were able to successfully fabricate gratings on Si_3N_4 membranes.

These gratings were characterized using SEM images and an original method of using FIB cut SEM images, which although destructive in nature, provided us with useful parameters such as grating line height and grating profile. We also report on the observation of grating signature as expected from our simulations, where our grating reflectivity increases to $\approx 70\%$ in comparison to an unpatterned membrane reflectivity $\approx 10\%$ around 934 nm. In the future we aim to fabricate gratings with a higher reflectivity over a broad wavelength range, so they can be used as high reflective mirrors in collective optomechanical experiments.

Finally, we also look theoretically into how having a thick membrane instead of the approximated thin membrane case, affects the optical and optomechanical properties of an array of membranes [38].

As a theoretical interest, in chapter 6, we look into hybrid systems for optomechanics, which for us is a doped membrane with two level atoms. In this work we report on the enhanced effective interactions between the mechanics and the cavity field which could lead to interesting physics such as the ground state cooling of mechanical resonator even in the unresolved sideband regime where radiation pressure cooling would be insufficient. This chapter is based on our published work [33].

In the near future we aim to fully characterize the double membrane arrays and experimentally investigate collective optomechanical effects as predicted by theory (chapter 2). However, the aim of the project itself is quite wide and open to many experiments. For instance, an interesting outlook would be in realizing hybrid setup involving membrane and ions and to be able to tune the interaction between these systems. The system will be a many mode system where the collective motion of the membranes will be coupled to the collective motion of ions through the cavity optical field.

Bibliography

- [1] Markus Aspelmeyer, Tobias J. Kippenberg, and Florian Marquardt. “Cavity optomechanics”. In: Rev. Mod. Phys. 86 (4 2014), pages 1391–1452. DOI: [10.1103/RevModPhys.86.1391](https://doi.org/10.1103/RevModPhys.86.1391).
- [2] V. B. Braginsky. “Measurement of weak forces in physics experiments”. In: University of Chicago press (1977).
- [3] C. M. Caves. “Quantum mechanical noise in an interferometer”. In: Phys. Rev. D 23 (1981), pages 1693–1708.
- [4] T. J. Kippenberg and K.J. Vahala. “Cavity optomechanics”. In: Optics Express 15 (2007), page 17172.
- [5] P. Meystre. “A short walk through quantum optomechanics”. In: Annalen der Physik arXiv:1210.3619v1 (2012).
- [6] A. Dorsel et al. “Optical bistability and mirror confinement induced by radiation pressure”. In: Phy. Rev. Letters 51 (1983), pages 1550–1583.
- [7] B. S. Sheard et al. “Observation and characterization of an optical spring”. In: Phy. Rev. A 69 (2004).
- [8] O. Arcizet et al. “Radiation pressure cooling and optomechanical instability of a micromirror”. In: Nature 444 (2006), pages 71–74.
- [9] A. Schliesser et al. “Radiation pressure cooling of a micromechanical oscillator using dynamical back action”. In: Phy. Rev.Letters 97 (2006), page 243905.
- [10] J. D. Thompson et al. “Strong dispersive coupling of a high-finesse cavity to a micromechanical membrane”. In: Nature 452.7183 (Mar. 2008), pages 72–75. ISSN: 0028-0836.
- [11] J. Chan et al. “Laser cooling of a nanomechanical oscillator into its quantum ground state”. In: Nature (London) 478 (2011), page 89.
- [12] J. D. Teufel et al. “Sideband cooling of micromechanical motion to the quantum ground state”. In: Nature (London) 475 (2011), page 359.
- [13] E. Verhagen et al. “Quantum-coherent coupling of a mechanical oscillator to an optical cavity mode”. In: Nature (London) 482 (2012), page 63.
- [14] T. P. Purdy et al. “Strong optomechanical squeezing of light”. In: Phys. Rev. X 3 (2013), page 031012.

- [15] S. Mancini et al. “Entangling macroscopic oscillators exploiting radiation pressure”. In: Phys. Rev. Letters 88 (2002), pages 120,401.
- [16] W. Marshall et al. “Towards quantum superpositions of a mirror”. In: Phys. Rev. Letters 91 (2003).
- [17] T. Bagci et al. “Optical detection of radio waves through a nanomechanical transducer”. In: Nat. Lett. 507 (2014), pages 81–85.
- [18] R. W. Andrews et al. “Bidirectional and efficient conversion between microwave and optical light”. In: Nat. Phys. 10 (2014), pages 321–326.
- [19] M. Eichenfeld et al. “Actuation of micro-optomechanical systems via cavity enhanced optical dipole forces”. In: Nature Photonics 1 (2007), page 416.
- [20] M. Bagheri et al. “Dynamic manipulation of nanomechanical resonators in the high-amplitude regime and non-volatile mechanical memory operation”. In: Nature Nanotechnology 6 (2011), pages 726–732.
- [21] B. M. Zwickl et al. “High quality mechanical and optical properties of commercial silicon nitride membranes”. In: Applied Physics Letters 92 (2008), page 103125.
- [22] Utku Kemiktarak et al. “Mode Competition and Anomalous Cooling in a Multimode Phonon Laser”. In: Phys. Rev. Lett. 113 (3 2014), page 030802. DOI: [10.1103/PhysRevLett.113.030802](https://doi.org/10.1103/PhysRevLett.113.030802).
- [23] S. Camerer et al. “Realization of an optomechanical interface between ultracold atoms and a membrane”. In: Phys. Rev. Lett. 107 (2011), page 223001.
- [24] D. J. Wilson et al. “Cavity Optomechanics with stoichiometric SiN films”. In: Phys. Rev. Lett. 103 (2009), page 207204.
- [25] M. Karuza et al. “Optomechanical sideband cooling of a thin membrane within a cavity”. In: New J. Phys. 14.9 (2012), page 095015. ISSN: 1367-2630.
- [26] U. Kemiktarak, M. Metcalfe, and J. Lawall. “Mechanically compliant grating reflectors for optomechanics”. In: Applied Physics Letters 100 (2012), page 061124.
- [27] T. P. Purdy, R. W. Peterson, and C. A. Regal. “Observation of radiation pressure shot noise on a macroscopic object”. In: Science 339 (2013), pages 801–804.
- [28] Christoph Reinhardt et al. “Ultralow-Noise SiN Trampoline Resonators for Sensing and Optomechanics”. In: Phys. Rev. X 6 (2 2016), page 021001. DOI: [10.1103/PhysRevX.6.021001](https://doi.org/10.1103/PhysRevX.6.021001).
- [29] R. A. Norte, J. P. Moura, and S. Gröblacher. “Mechanical Resonators for Quantum Optomechanics Experiments at Room Temperature”. In: Phys. Rev. Lett. 116 (14 2016), page 147202. DOI: [10.1103/PhysRevLett.116.147202](https://doi.org/10.1103/PhysRevLett.116.147202).
- [30] A. Yilmaz et al. In: arXiv:1608.02799 (2016).
- [31] T. P. Purdy et al. “Optomechanical raman-ratio thermometry”. In: arXi :1406.7247v1 (2014).
- [32] C. Genes et al. “Atom-membrane cooling and entanglement using cavity electromagnetically induced transparency”. In: Phys. Rev. A (2011), page 013801.

- [33] Aurélien Dantan et al. “Hybrid cavity mechanics with doped systems”. In: Phys. Rev. A 90 (2014), page 033820.
- [34] A Xuereb, C Genes, and A Dantan. “Strong coupling and long range collective interactions in optomechanical arrays”. In: Phys. Rev. Lett. 109 (2012), page 223601.
- [35] André Xuereb et al. “Reconfigurable Long-Range Phonon Dynamics in Optomechanical Arrays”. In: Phys. Rev. Lett. 112 (13 2014), page 133604. DOI: [10.1103/PhysRevLett.112.133604](https://doi.org/10.1103/PhysRevLett.112.133604).
- [36] Mian Zhang et al. “Synchronization of Micromechanical Oscillators Using Light”. In: Phys. Rev. Lett. 109 (23 2012), page 233906. DOI: [10.1103/PhysRevLett.109.233906](https://doi.org/10.1103/PhysRevLett.109.233906).
- [37] A Xuereb, C Genes, and A Dantan. “Collectively enhanced optomechanical coupling in periodic arrays of scatterers”. In: Phys. Rev. A 88 (2013), page 053803.
- [38] Bhagya Nair, André Xuereb, and Aurélien Dantan. “Cavity optomechanics with arrays of thick dielectric membranes”. In: Phys. Rev. A 94 (2016), page 053812.
- [39] A.M. Jayich et al. “Dispersive optomechanics: a membrane inside a cavity”. In: New J. Phys. 10 (2008), page 095008.
- [40] M. Pinard, Y. Hadjar, and A. Heidmann. “Effective mass in quantum effects of radiation pressure”. In: Eur.Phys.J 7 (1999), pages 107–116.
- [41] C. Stambaugh et al. “From membrane-in-the-middle to mirror-in-the-middle with a high-reflectivity sub-wavelength grating”. In: Ann.Physics (Berlin) 1-2 (2015), pages 81–88.
- [42] S. Chakram et al. “Dissipation in ultra high quality factor SiN membrane resonators”. In: Phys. Rev. Lett. 112 (2014), page 127201.
- [43] D.J. Wilson. “Cavity Optomechanics with high stress Silicon nitride films”. California Institute of Technology, 2012.
- [44] J.Y. Lee, J.W. Hahn, and H.W. Lee. “Spatiospectral transmission of a plane mirror Fabry Perot interferometer with nonuniform finite size diffraction beam illuminations”. In: J.Opt.Soc.Am.A 19 (2002), page 973.
- [45] Simon Groblacher. “Quantum opto-mechanics with micromirrors”. University of Vienna, Austria, 2012.
- [46] B.E.A. Saleh and M.C. Teich. Fundamentals of Photonics. 2007.
- [47] I. H. Deutsch et al. “Photonic band gaps in optical lattices”. In: Phys. Rev. A 52 (2 1995), pages 1394–1410. DOI: [10.1103/PhysRevA.52.1394](https://doi.org/10.1103/PhysRevA.52.1394).
- [48] André Xuereb et al. “Scattering theory of cooling and heating in optomechanical systems”. In: Phys. Rev. A 79 (5 2009), page 053810. DOI: [10.1103/PhysRevA.79.053810](https://doi.org/10.1103/PhysRevA.79.053810).
- [49] C.J Chang-Hasnain. “High-contrast gratings as a new platform for integrated optoelectronics”. In: IOP publishing Semiconductor Science and Technology 26 (2010), page 014043.

- [50] M.C.Y. Huang, Y. Zhou, and C.J. Chang-Hasnain. “A surface-emitting laser incorporating a high-index-contrast subwavelength grating”. In: Nature Photonics 1 (2007), page 119.
- [51] C.H.B. Bui et al. “High-reflectivity, high-Q micromechanical membranes via guided resonances for enhanced optomechanical coupling”. In: Applied Physics Letters 100 (2012), page 021110.
- [52] Utku Kemiktarak et al. “Cavity optomechanics with sub-wavelength grating mirrors”. In: New J. Phys. 14.12 (2012), page 125010. ISSN: 1367-2630.
- [53] JM.G. Moharam, E.B. Grann, and D.A. Pommet. “Formulation for stable and efficient implementation of the rigorous coupled-wave analysis of bianry gratings”. In: J.Opt.Soc.Am.A 12 (1995), page 1068.
- [54] V. Karagodsky, F.G. Sedgwick, and C.J. Chang-Hasnain. “Theoretical analysis of subwavelength high contrast grating reflectors”. In: Optics Express 18 (2010), page 16973.
- [55] C. Chang-Hasnain and W. Yang. “High-contrast gratings for integrated optoelectronics”. In: Adv. in Physics and Optics 4 (2012), pages 379–440.
- [56] Thomas Germer. “Model Integrated Scattering Tool (MIST)”. In: NIST ().
- [57] L. Tian and P. Zoller. “Coupled Ion-Nanomechanical Systems”. In: Phys. Rev. Letts 93 (2004), page 266403.
- [58] I. Favero and K. Karrai. “Cavity cooling of a nanomechanical resonator by light scattering”. In: New. J. Phys 10 (2008), page 095006.
- [59] S. Singh et al. “Coupling Nanomechanical Cantilevers to Dipolar Molecules”. In: Phys. Rev. Letts 101 (2008), page 263603.
- [60] K. Hammerer et al. “Strong Coupling of a Mechanical Oscillator and a Single Atom”. In: Phys. Rev. Letts 103 (2009), page 063005.
- [61] V. Puller, B. Lounis, and F. Pistolesi. “Single Molecule Detection of Nanomechanical Motion”. In: Phys. Rev. Letts 110 (2013), page 125501.
- [62] J. Restrepo, C. Ciuti, and I. Favero. “Single-Polariton Optomechanics”. In: Phys. Rev. Letts 112 (2014), page 013601.
- [63] D. Meiser and P. Meystre. “Superstrong coupling regime of cavity quantum electrodynamics”. In: Phys. Rev. A 73 (2006), page 033417.
- [64] P. Treutlein et al. “Bose-Einstein Condensate Coupled to a Nanomechanical Resonator on an Atom Chip”. In: Phys. Rev. Letts 99 (2007), page 140403.
- [65] C. Genes, D. Vitali, and P. Tombesi. “Ground-state cooling of a micromechanical oscillator: Comparing cold damping and cavity-assisted cooling schemes”. In: Phys. Rev. A 77 (2008), page 050307.
- [66] H. Ian et al. “Cavity optomechanical coupling assisted by an atomic gas”. In: Phys. Rev. A 78 (2008), page 013824.

- [67] C. Genes and D. Ritsch H.and Vitali. “Micro-mechanical oscillator ground state cooling via intracavity optical atomic excitations”. In: Phys. Rev. A 80 (2009), page 061803.
- [68] K. Hammerer et al. “Establishing Einstein-Poldosky-Rosen Channels between Nanomechanics and Atomic Ensembles”. In: Phys. Rev. Letts 102 (2009), page 020501.
- [69] A. B. Bhattacharjee. “Cavity quantum optomechanics of ultracold atoms in an optical lattice: Normal-mode splitting”. In: Phys. Rev. A 80 (2009), page 043607.
- [70] K. Hammerer et al. “Optical lattices with micromechanical mirrors”. In: Phys. Rev. Letts 104 (2010), page 143002.
- [71] D. Hunger et al. “Resonant coupling of a Bose-Einstein condensate to a micromechanical oscillator”. In: Phys. Rev. Letts 104 (2010), page 143002.
- [72] M. Paternostro, G. De. Chiara, and G. M. Palma. “Cold-Atom-Induced Control of an Optomechanical Device”. In: Phys. Rev. Letts 104 (2010), page 243602.
- [73] S. Camerer et al. “Realization of an Optomechanical Interface Between Ultracold Atoms and a Membrane”. In: Phys. Rev. Letts 107 (2011), page 223001.
- [74] B. Vogell et al. “Cavity-enhanced long-distance coupling of an atomic ensemble to a micromechanical membrane”. In: Phys. Rev. A 87 (2013), page 023816.
- [75] A. öckel et al. “Sympathetic cooling of a membrane oscillator in a hybrid mechanical-atomic system”. In: Nature Nanotechnology 10 (2015), pages 55–59.
- [76] I. Wilson-Rae, P. Zoller, and A. Imamoglu. “Laser Cooling of a Nanomechanical Resonator Mode to its Quantum Ground State”. In: Phys. Rev. Letts 92 (2004), page 075507.
- [77] N. Lambert et al. “Electron-Spin Manipulation and Resonator Readout in a Double-Quantum-Dot Nanoelectromechanical System”. In: Phys. Rev. Letts 100 (2008), page 136802.
- [78] I. Yeo et al. “Strain-mediated coupling in a quantum dot-mechanical oscillator hybrid system”. In: Nat. Nanotech 9 (2014), page 106.
- [79] P. Rabl et al. “Strong magnetic coupling between an electronic spin qubit and a mechanical resonator”. In: Phys. Rev. Letts 79 (2009), 041302(R).
- [80] O. Arcizet et al. “A single nitrogen-vacancy defect coupled to a nanomechanical oscillator”. In: Nat. Phys 7 (2012), page 879.
- [81] S. Kolkowitz et al. “Coherent sensing of a mechanical resonator with a single-spin qubit”. In: Science 335 (2012), page 1603.
- [82] Z. Yin et al. “Large quantum superpositions of a levitated nanodiamond through spin-optomechanical coupling”. In: Phys. Rev. A 88 (2013), page 033614.
- [83] M. Scala et al. “Matter-Wave Interferometry of a Levitated Thermal Nano-Oscillator Induced and Probed by a Spin”. In: Phys. Rev. Letts 111 (2013), page 180403.

- [84] T. Ramos et al. “Nonlinear Quantum Optomechanics via Individual Intrinsic Two-Level Defects”. In: Phys. Rev. Letts 110 (2013), page 193602.
- [85] A. D. O’Connell et al. “Quantum ground state and single-phonon control of a mechanical resonator”. In: Nature 464 (2010), page 697.
- [86] J. M. Pirkkalainen et al. In: Nature 494 (2013), page 211.
- [87] T. A. Palomaki et al. “Coherent state transfer between itinerant microwave fields and a mechanical oscillator”. In: Nature 495 (2013), page 210.
- [88] K. Molmer, Yann Le Coq, and S. Seidelin. “Dispersive coupling between light and a rare-earth-ion-doped mechanical resonator”. In: Phys. Rev. A 94 (2016), page 053804.
- [89] C. Genes et al. “Ground-state cooling of a micromechanical oscillator: Comparing cold damping and cavity-assisted cooling schemes”. In: Phys. Rev. A 77 (2008), page 033804.
- [90] I. Wilson-Rae et al. “Theory of Ground State Cooling of a Mechanical Oscillator Using Dynamical Backaction”. In: Phys. Rev. Letters 99 (2007), page 093901.
- [91] A. Dantan et al. “Self-cooling of a movable mirror to the ground state using radiation pressure”. In: Phys. Rev. A 77 (2008), 011804(R).
- [92] J. Giesler et al. “Subkelvin Parametric Feedback Cooling of a Laser-Trapped Nanoparticle”. In: Phys. Rev. Letts 109 (2012), page 103603.
- [93] J. Millen et al. “Nanoscale temperature measurements using non-equilibrium Brownian dynamics of a levitated nanosphere”. In: Nat. Nanotech 9 (2014), page 425.
- [94] T. Schwartz et al. “Reversible Switching of Ultrastrong Light-Molecule Coupling”. In: Phys. Rev. Letts 106 (2011), page 196405.